CHALMERS
UNIVERSITY OF TECHNOLOGY

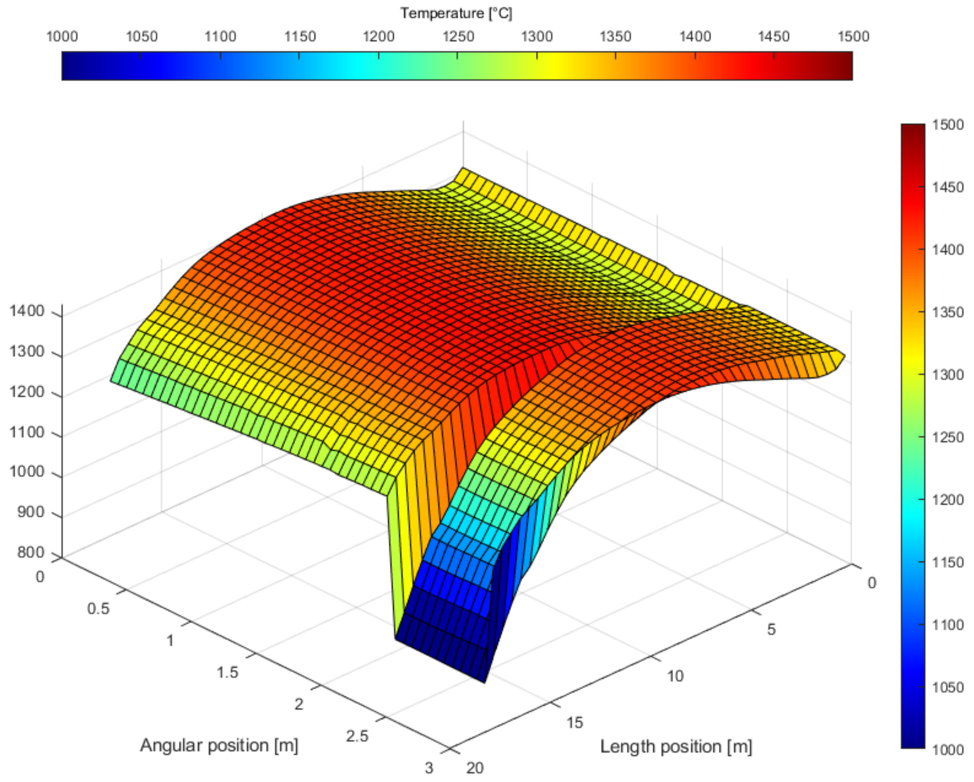

Demonstration Scale of a Rotary Kiln for Cement Production Using a Thermal Plasma

A Scaling and Heat Transfer Study

Master's thesis in Master Programme Sustainable Energy Systems

ALICE FAKT
MINEA NILSSON

DEPARTMENT OF SPACE, EARTH AND ENVIRONMENT
CHALMERS UNIVERSITY OF TECHNOLOGY
Gothenburg, Sweden 2023
www.chalmers.se

Master's thesis 2023

Demonstration Scale of a Rotary Kiln for Cement Production Using a Thermal Plasma

A Scaling and Heat Transfer Study

ALICE FAKT
MINEA NILSSON

Department of Space, Earth and Environment
Division of Energy Technology
Chalmers University of Technology
Gothenburg, Sweden 2023

Demonstration Scale of a Rotary Kiln for Cement Production Using a Thermal Plasma
A Scaling and Heat Transfer Study
ALICE FAKT
MINEA NILSSON

Supervisors: Adrian Gunnarsson, Elias Ehlmé and Klas Andersson, Department of Space, Earth and Environment
Examiner: Klas Andersson, Department of Space, Earth and Environment

Master's Thesis 2023
Department of Space, Earth and Environment
Division of Energy Technology
Chalmers University of Technology
SE-412 96 Gothenburg
Telephone +46 31 772 1000

Typeset in LaTeX
Printed by Chalmers Reproservice
Gothenburg, Sweden 2023

Demonstration Scale of a Rotary Kiln for Cement Production Using a Thermal Plasma
A Scaling and Heat Transfer Study
ALICE FAKT
MINEA NILSSON
Department of Energy Technology
Chalmers University of Technology

Abstract

The cement industry plays a significant role in global greenhouse gas emissions, prompting governments worldwide to establish targets for mitigating the impacts of global warming and the greenhouse effect. This master thesis therefore focuses on reducing the greenhouse gas emissions from the cement process, in collaboration with Swedish cement manufacturer Heidelberg Materials Sweden. The proposed approach involves replacing the conventional fossil fuel flame in the rotary kiln with an electrical thermal plasma. However, direct implementation to full scale processes are seldom done due to feasibility uncertainties and large costs, consequently, this thesis is done on a demonstration scale of a rotary kiln. The study was conducted with modelling tool simulations, using a model previously developed in Matlab at the division of Energy Technology at Chalmers University of Technology.

The aim of the thesis is to investigate the heat transfer in a demonstration scale rotary kiln operated with a thermal plasma, with carbon dioxide utilised as both the working gas in the plasma and the secondary gas. Moreover, the design and operational parameters that a rotary kiln would have in order to fulfil the temperature requirements for cement production are also examined. The expected outcome is a proposed design of a demonstration scale kiln, used for Heidelberg Materials Sweden's process.

The results from the simulations imply that it is viable to design a demonstration scale rotary kiln operated with a thermal plasma. It is concluded that the heat transfer is equally as good as for the fossil fuel driven kiln, and the temperature requirements are achieved. Two different designs are found to be good options, one where the plasma is tilted towards the bed material, then the bed material reaches the desired temperature, whereas the flue gas is still high. The other design is to tilt the plasma towards the bed as well as increase the mass flow of bed material, and add particle content to the plasma as to increase radiation. Then the bed material achieves the desired temperature, as well as a lower flue gas temperature similar to the existing rotary kiln at Heidelberg Materials. To further investigate the impact of a thermal plasma in rotary kilns, experimental research is encouraged, for example to examine the temperature profile of larger plasmas and how the actual heat transfer affected is when implementing it in a rotary kiln.

Keywords: Cement production, rotary kiln, thermal plasma, heat transfer mechanisms, Matlab model.

Acknowledgements

We would like to thank everyone who made this thesis possible, to our friends for cheering us on, and to all colleagues at the division of Energy Technology at Chalmers University of Technology. A special thank you to our examiner and supervisor Klas Andersson, and to our supervisors Adrian Gunnarsson and Elias Ehlmé at Chalmers University of Technology who have provided us with a lot of insightful feedback and inspiration. We are grateful for the opportunity to contribute to an industry that is moving towards a more sustainable future.

Alice Fakt and Minea Nilsson, Gothenburg, May 2023

Contents

List of Figures **xi**

List of Tables **xiii**

1 Introduction **1**
- 1.1 Background . . . 1
- 1.2 Aim . . . 3
- 1.3 Limitations . . . 3
- 1.4 Problem formulation . . . 4

2 Theory **5**
- 2.1 Cement production . . . 5
  - 2.1.1 Heidelberg Materials Sweden's process . . . 5
- 2.2 Rotary kilns . . . 8
  - 2.2.1 Heat transfer in rotary kilns . . . 9
  - 2.2.2 Rotary kiln heat transfer modelling tool . . . 9
- 2.3 Plasma torches . . . 12
  - 2.3.1 Carbon dioxide environments in cement processes . . . 14
  - 2.3.2 Difference between plasma gas and coal flame . . . 14
- 2.4 Scaling of thermal processes . . . 15

3 Method **17**
- 3.1 Initial scaling of process data . . . 17
  - 3.1.1 Scaling of secondary gas flow . . . 18
  - 3.1.2 Scaling of maximum plasma temperature . . . 18
  - 3.1.3 Scaling of initial dimensions of the rotary kiln . . . 19
  - 3.1.4 Checking of flow properties . . . 19
- 3.2 Overall heat balance . . . 20
- 3.3 Plasma gas temperature profiles . . . 21
  - 3.3.1 Initial temperature profile . . . 21
  - 3.3.2 Polynomial function . . . 23
- 3.4 Updating the heat transfer model . . . 24
  - 3.4.1 Implementation of the plasma temperature in the model . . . 25
  - 3.4.2 Closing the energy balance . . . 26
- 3.5 Simulations . . . 26
  - 3.5.1 Coal case . . . 26
  - 3.5.2 Reference case . . . 27

3.5.3 Simulation cases 27

4 Results & Discussion 29
4.1 Initial scaling of process data 29
4.2 Plasma temperature profiles 29
4.2.1 Polynomial function 30
4.3 Coal case 31
4.4 Reference case 33
4.5 Different parameters in cases 36
4.5.1 Kiln length 36
4.5.2 Kiln radius 37
4.5.3 Production rate 39
4.5.4 Particle content in suspension 41
4.5.5 Plasma length 43
4.5.6 Tilted plasma 45
4.6 Selected dimensions 48
4.7 Sensitivity analysis 51

5 Conclusion 53

6 Further research 55

Bibliography 57

A Appendix 1 I
A.1 Length I
A.2 Radius V
A.3 Bed mass flow XI
A.4 Particle content XV
A.5 Flame angle XVII
A.6 Flame length XXIII

B Appendix 2 XXIX

List of Figures

2.1 Schematic of the cement production process at Heidelberg Materials Sweden. Black arrows represent the product flow, red arrows represent the where heat is added, and blue arrows represent the gas flow 6
2.2 Schematic of a rotary kiln, courtesy of Adrian Gunnarsson [1] 8
2.3 Cross-section of a rotary kiln, describing the different heat transfer mechanisms and also the mixing and motion of the bed, courtesy of Adrian Gunnarsson [1] 12
2.4 Schematic of a non transferred arc plasma burner, courtesy of Adrian Gunnarsson 13

3.1 Schematic of the calciner, rotary kiln, and cooler in the present cement process at Heidelberg Materials Sweden 17

4.1 Axial temperature map of a vertical cross-section of the coal flame and gas within the present rotary kiln at Heidelberg Materials Sweden 31
4.2 A three dimensional temperature map of the kiln walls and bed material within the present rotary kiln at Heidelberg Materials Sweden. . 32
4.3 Axial temperature map of the plasma and gas within the reference case rotary kiln 34
4.4 A three dimensional temperature map of the kiln walls and bed within the reference case rotary kiln 35
4.5 Temperature of the bed material for different kiln lengths 37
4.6 Flue gas temperatures for different kiln lengths 37
4.7 Temperature of the bed material for different kiln radii 38
4.8 Temperature of the flue gas for different kiln radii 39
4.9 Temperature of the bed material for different bed mass flows 40
4.10 Temperature of the flue gas for different bed mass flows 40
4.11 Temperature of the bed material for different amounts of particle content. 41
4.12 Temperature of the flue gas for different amounts of particle content . 42
4.13 Heat transfer to the bed for different projected surface area of particles, convection presented on the top, conduction in the middle, and radiation on the bottom 43
4.14 Temperature of the bed material for different plasma lengths 44
4.15 Temperature of the flue gas for different plasma lengths 44

4.16 Axial temperature map of the gas and the plasma within the kiln, with a plasma length of 0.8 m 45
4.17 Axial temperature map of the gas and the plasma within the kiln, where the plasma is tilted by 5° 45
4.18 Three dimensional temperature map of the kiln walls and bed for a plasma angle of 5° 46
4.19 Temperature of the bed material for different plasma angles 47
4.20 Temperature of the flue gas for different plasma angles 47
4.21 Heat transferred to bed via convection, for different plasma angles . . 48
4.22 Three dimensional temperature map of the kiln walls and bed for a optimised kiln 50
4.23 Axial temperature map of the gas and the plasma within the optimised kiln 50
4.24 Axial temperature maps of the gas and plasma within the kiln. At the top: plasma gas with the radius increased by 20%, on the bottom: plasma gas with the radius decreased by 20% 52

List of Tables

3.1 Parameters used in the coal case 27
3.2 Parameters used in the reference case 27
3.3 Parameters used in different simulation cases 28

4.1 Results from initial scaling 29
4.2 Heat balance results for the coal case 33
4.3 Simulation results for the coal case 33
4.4 Simulation results for the reference case 34
4.5 Heat balance results for the reference case 35
4.6 Parameters used in the optimised demonstration scale rotary kiln . . 49
4.7 Simulation results for the optimised kiln 49
4.8 Heat balance results for the optimised kiln 51
4.9 Comparison of heat to clinker for Kiln 8 and the optimised kiln . . . 51

1

Introduction

Combustion of fossil fuels generates greenhouse gases such as carbon dioxide and methane. These gases absorb and re-emit the heat from leaving the Earth's surface, and causes a rise in the Earth's temperature, which in turn causes severe fires, droughts, rising sea levels, and declining biodiversity. Since the 1800s, the global average temperature on Earth has increased by around 1.1°C, and in order to keep global warming below 1.5°C, fossil fuel production and usage must decline with at least 6% between 2020 and 2030 [2]. To reach this target, large industries must decrease their use of fossil fuels, causing process changes which will look different for different industries. In this work, the focus is on the cement industry and production. The cement industry is one of the major contributors of greenhouse gas emissions, alongside with the steel industry and the production of oil and gas [3]. For the cement process, one possible option to substitute fossil fuels and reduce CO_2 emissions is to electrify the calcination and clinkerisation processes using a thermal plasma. The calcination reaction is the most energy demanding part of the cement process, which partly takes place in the rotary kiln. The cement production company Heidelberg Materials Sweden has set a goal to have net zero emissions by 2030, and as a part of reducing their CO_2 emissions they are investigating the possibility to replace the fossil fuel burners in the rotary kiln with a thermal plasma [4]. Due to large investment costs and uncertainties in the feasibility, as well as on the impact of the heat transfer and process conditions, direct implementations on full scale processes are seldom done. Instead, initial studies are done on smaller scales of the process before implementing on full scale processes. Thus, the focus of this thesis is to design a demonstration scale of the cement rotary kiln, with a thermal plasma as the main heat source.

1.1 Background

The production of cement is today responsible for about 8% of the world's greenhouse gas emissions [4], and the company Heidelberg Materials Sweden is the second largest emitter of greenhouse gases in Sweden, with emissions corresponding to 1.9 Mton carbon dioxide equivalents in the year 2020 [5]. Furthermore, the utilisation of cement is expected to increase in the near future due to its significant part in the developing of societies, which is of great importance as the worlds population is continuously growing, and the need for good infrastructure, buildings and construction is prominent [6]. Therefore, there is a great need to reduce these emissions related to cement production in order to handle the global warming and work towards a sustainable future. The most energy demanding reaction that occurs in cement production is the calcination reaction. This is when the limestone ($CaCO_3$) in the raw material is heated and decomposed, so that carbon dioxide (CO_2) is formed and leaves the solid material, described by the following reaction:

$$CaCO_3 \rightarrow CaO + CO_2 \tag{1.1}$$

Hence, this release of carbon dioxide cannot be prevented while producing cement using limestone as a raw material, since it is inherent in the chemical reaction when producing lime (CaO), and when relating this emission to the whole cement process it corresponds to roughly 60% of the total emissions. The remaining part of the carbon dioxide emissions from the process, 40%, comes from combustion, to supply the heat required by the process of the calcination and the following sintering steps, where the fuel is mainly fossil [4].

Heidelberg Materials Sweden has the ambition to have net zero emissions by 2030, and are therefore working towards and investigating various climate friendly ways to produce cement and clinker [5]. Their production site in Slite, Gotland, is the site which stands for the majority of their CO_2 emissions and is therefore the site that is in focus when investigating different ways to operate the process [4]. Since 60% of the emissions cannot be prevented, the focus in this thesis is on the 40% originating from combustion. This thesis is therefore a contribution to the investigation work of combustion alternatives in the cement process. The thesis will be focusing on the possibility to use a thermal plasma, using carbon dioxide as the working gas, instead of fossil fuel, at a demonstration scale of the rotary kiln in the original process. The main reactions in the rotary kiln are the sintering reactions, thus reaching the temperatures ensuring sintering will be the main focus of this thesis.

The demonstration scale of the rotary kiln is aimed to produce approximately 10 ton/h, as opposed to the 230 ton/h production at the present full scale process. Similar studies have previously been made, but focusing on the feasibility of electrifying the cement process using a plasma, and it was concluded to be a suitable option ([7], [8]). The master thesis by Burman and Engvall employed a heat transfer model for the full-scale cement process and evaluated the viability to use a thermal plasma, as well as investigated the feasibility of implementing carbon capture and storage in the process [7]. The master thesis by Petersson continued the study by further developing the heat transfer model used by Burman and Engvall, and additionally studied the effect on the bed material when implementing a thermal plasma in the full-scale cement production, and introducing radiating particles to the high temperature gas zones [8]. This master thesis will continue the study of implementing a thermal plasma in the cement process, focusing on a demonstration scale and evaluating the equipment size as well as operational parameters required for such a rotary kiln and process. Similarly, conceptual testing of calcination with plasma has been tested by Heidelberg Materials Sweden in a small-scale rotary kiln with a length of one meter, called Kiln 9, and it has proven to be successful.

A plasma is often referred to as the fourth state of aggregation, which can be described as an ionised gas. This ionisation occurs when a gas moves through an electric arc and it is used as a heat source in industries such as metallurgy and material processing [9]. The investigation of this thesis will also include using the CO_2 formed in the calcination process as the working gas in the plasma, hence recycling and utilising the otherwise emitted gas. However, it is important to note that carbon capture and storage (CCS) is also required in order for Heidelberg Materials Sweden to achieve their net zero emission target completely. An advantage of using CO_2 in the process is that the performance of CCS will be better since fewer separation steps are required, which are related to high energy penalties when gas streams consist of different species. Furthermore, a disadvantage of using a plasma is that the heat transfer from radiation is decreased compared to a conventional fossil fuel flame as there will be no radiating particles present. CO_2 for the plasma has the advantage since it radiates heat, allowing for heat to be more effectively transferred from the plasma. It should be noted that process changes that affects the radiation in the rotary kiln will have great impact on the overall heat transfer, since the radiative heat transfer stands for about 80% of the total heat transfer to the bed material within the kiln [10].

1.2 Aim

The aim of this project is to examine the possibilities to operate a rotary kiln used for cement production with a CO_2 thermal plasma, at a size of a demonstration scale. The size of the demonstration scale kiln will be designed to aim for a production rate around 5-25 t/h, using an 8 MW thermal plasma. Design parameters such as equipment sizing and temperature ranges are to be investigated. Additionally, ways to enhance the heat transfer from the plasma is to be examined by tilting the plasma and by adding radiating particles.

The expected outcome is a design of a demonstration scale rotary kiln used for Heidelberg Materials Sweden's process, with suggested equipment dimensions and heat transfer parameters. This is achieved and presented with a modelling tool which has previously been developed in Matlab. The tool will provide data about how the heat transfer is affected by using a plasma torch in the rotary kiln. The results from the tool will additionally provide details about the operating parameters of the rotary kiln.

1.3 Limitations

Carbon capture and storage technology (CCS) will have to be implemented in order for Heidelberg Materials to reach net zero emissions. However, any feasibility evaluation of CCS will be beyond the scope of this master thesis project. Other ways to reduce the climate impact associated with the production of cement, such as replacing the raw material limestone for alternative materials like blast furnace slag from steel production, is also beyond the scope of this thesis. The main process step to be considered is the rotary kiln, other process steps within the cement production line will not be considered. No economic evaluation will be carried out within this project.

Furthermore, the project will not be focusing on different options of heat transfer technologies other than a thermal plasma, as this technology has already been chosen by Heidelberg Materials Sweden as the main technology path. Electricity production and power supply will also be beyond the scope of the project.

1.4 Problem formulation

The question which is to be examined in this thesis is first and foremost if it is theoretically possible to operate a demonstration scale of a rotary kiln with a CO_2 thermal plasma instead of fossil fuel, reaching the bed temperature required for the clinkerisation of the bed material to take place. It will also be examined what the possible dimensions of such a rotary kiln are in order to achieve similar heat transfer conditions as in the rotary kiln at Heidelberg Materials Sweden, including size of the heat demand, and dimensions such as length and diameter, as well as operational parameters such as secondary gas flow and bed material flow. Further, it will be examined which temperature intervals the plasma gas will be in, and how the temperature interval inside the kiln will vary in comparison to a fossil fuel flame. Finally, the heat transfer when operating the kiln with CO_2-plasma will be compared to the heat transfer of the fossil fuel kiln currently operated at Heidelberg Materials Sweden.

2

Theory

In this chapter, relevant theory will be presented in order to help the reader interpret the method and results in following chapters. First, a description of the cement production at Heidelberg Materials Sweden will be presented in section 2.1. Next, a description of rotary kilns in general, and a description of heat transfer and the modelling of rotary kilns, is presented in section 2.2. Then, plasma and plasma torches will be described, followed by a comparison of a plasma gas and a coal flame in section 2.3, lastly scaling of combustion processes will be described briefly in 2.4.

2.1 Cement production

Cement is a binding material that is frequently used in the construction of buildings as well as in engineering constructions [11]. The global cement production was 4270 million tons in 2021 [12]. The cement product is a powder and its function is that when mixed with water it will harden into a solid mass which therefore binds structures together. Two common applications of cement are as mortar, used as binding material for brick walls and other related structures, or as concrete, used in various construction applications. Mortar and concrete are formed when mixing cement with other components, such as sand and crushed stones of various particle size [11]. The raw materials for producing cement are lime- and marlstone (which are rich in calcium, $CaCO_3$), sand and clay (which both consists of silicon, iron and alumina in different forms, SiO_2, Fe_2O_3 and Al_2O_3). These compounds are all present in nature and therefore the material is mined from quarries rich in these compounds [13]. The general process for cement production is to grind and mix the raw materials to a fine powder, provide heat so that volatiles leave the powder forming clinker, and finally grinding the clinker into the final cement powder [11]. Heidelberg Materials Sweden is a Swedish manufacturer of cement and has factories in both Skövde (mainland) and Slite (island of Gotland) [4], a more detailed description of their production process in Slite will be described in the following section.

2.1.1 Heidelberg Materials Sweden's process

The key parts of the process for cement production at the Slite site is described by the schematic below in Figure 2.1.

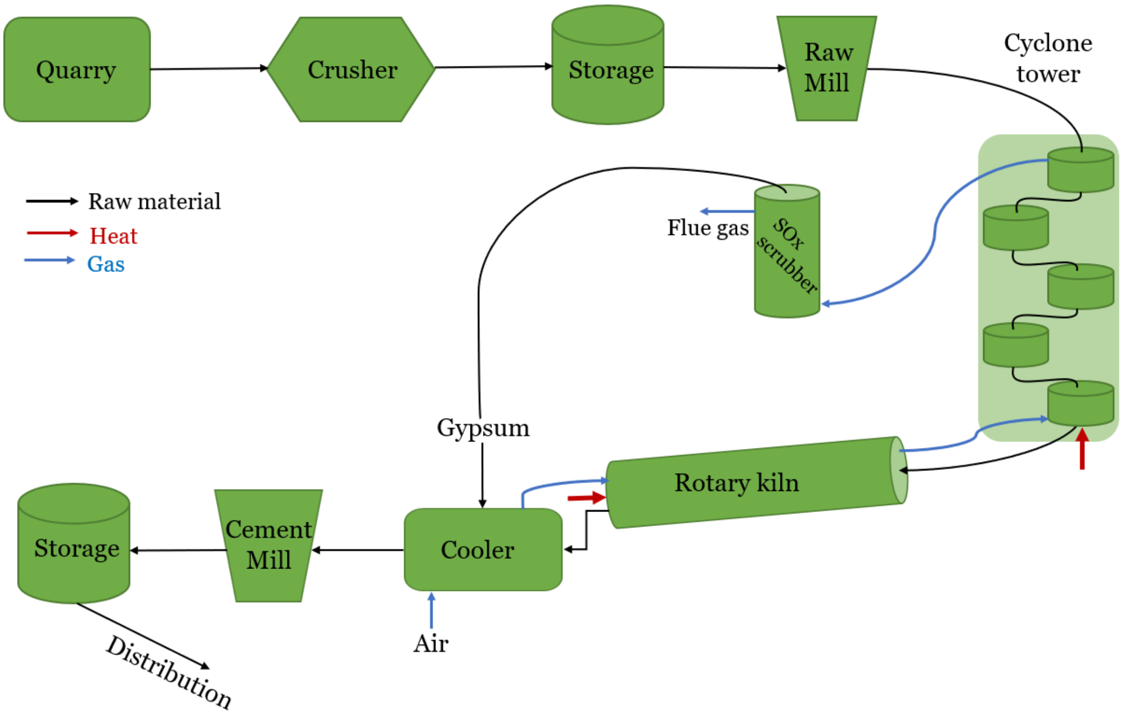

Figure 2.1: Schematic of the cement production process at Heidelberg Materials Sweden. Black arrows represent the product flow, red arrows represent the where heat is added, and blue arrows represent the gas flow

In Figure 2.1 it can be seen that the process starts with the mining of limestone and marlstone in a quarry, where the raw material is collected and sent to a crushing facility at the plant where it is crushed to smaller pieces and then potentially stored in a storage facility for some time. Sand and clay consisting of silicon, iron and alumina, are then added to the crushed stone to obtain a certain chemical composition which is important as to achieve a good quality of the product. The mixture often constitutes of 80 weight% of the lime- and marlstone and the rest coming from clay and sand [4].

Thereafter, the mixture is ground in a raw mill to a fine powder, called raw meal. If there is no need for immediate production, the raw meal can be stored as a buffer and be utilised when there is a deficit of raw material extraction. The milling is an important step since having fine particles promotes the reactions that follow during calcination and clinkerisation, as well as promoting heating and drying by the exiting flue gases in the mill. This flue gas arises from downstream process combustion, and using it to heat the raw meal makes it completely ready for further production steps [13]. Hence, the raw meal is transported to the cyclone tower which has the function of preheating the material with the help of the counter-current hot flue gases from downstream process combustion, hence utilising much of the existing heat, making it more energy efficient. The tower consists of five stages, i.e five cyclones, and they can be described as counter-current heat exchangers where the raw meal is flowing downstream the process, and hot flue gases flow upstream. Located at the bottom of the cyclone tower is the calciner, here the main calcination of the preheated raw meal will occur as the material has reached a sufficient temperature around 900°C [4]. The calcination reaction is as follows:

$$CaCO_{3(s)} \rightarrow CaO_{(s)} + CO_{2(g)} \tag{2.1}$$

The calcination reaction is endothermic with a heat of reaction of 1.7 MJ/kg $CaCO_3$, at it's dissociation temperature [14]. Reaction 2.1 shows how the calcium carbonate, when heated, releases carbon dioxide and left in its solid state is the calcium oxide. The heat required for calcination stands for 60% of the total energy consumption of the cement plant [13]. In the calciner, in which heat is supplied by combustion but also by heat recovery from hot flue gases, approximately 95% of the raw meal calcinates, and the rest of the raw meal calcinates in the rotary kiln which is the following process step. The carbon dioxide released during the calcination reaction is responsible for 60% of the total emissions during cement production. Next, the material feed enters the rotary kiln where clinkerisation reactions proceed after the calcination. Clinkerisation is a set of complex chemical reactions that essentially produce the cement, and these reactions occur at temperatures between 900-1450°C [4]. The high temperatures cause some compounds to react when mixed together with free calcium oxide and form new compounds, such as belite, alite, aluminate and ferrite [13]. The main clinkerisation reactions are as follows:

$$2\,CaO_{(s)} + SiO_{2(s)} \rightarrow 2\,CaO \cdot SiO_{2(s)} \tag{2.2}$$

$$2\,CaO \cdot SiO_{2(s)} + CaO_{(s)} \rightarrow 3\,CaO \cdot SiO_{2(s)} \tag{2.3}$$

$$3\,CaO_{(s)} + Al_2O_{3(l)} \rightarrow 3\,CaO \cdot Al_2O_{3(s)} \tag{2.4}$$

$$4\,CaO_{(s)} + Al_2O_{3(l)} + Fe_2O_{3(l)} \rightarrow 4\,CaO \cdot Al_2O_3 \cdot Fe_2O_{3(s)} \tag{2.5}$$

Reaction 2.2 describes the belite formation when free lime reacts with silicon oxide, whereas reaction 2.3 describes the alite formation which occurs when belite further reacts with free lime. Reaction 2.4 describes the formation of aluminate, and reaction 2.5 describes the formation of ferrite, both reactions occurring at temperatures above 1300°C. The material feed exiting the outlet of the kiln will now be around 1450°C, and the feed will consist of lumps of product (often referred to as nodules) which form during the rotation and tilting of the kiln [13]. A more detailed description of the rotary kiln can be found in section 2.2.

The 1450°C clinker is then fed through a cooler which cools the product with ambient air to approximately 100°C. The cooling air is thereby heated by the hot clinker, and the gas flow is split and directed to the rotary kiln and calciner, and used for combustion with fuel in the rotary kiln and calciner forming flue gases which is used in the preheater tower upstream. It is of importance that this cooling step proceeds rapidly, due to the instability of some clinker products, for example alite described by reaction 2.3, can react backwards during slow cooling [13]. After the clinker has cooled it will proceed to a cement mill where it is ground to a fine powder which is the finished cement product. In the grinding there will also be an addition of gypsum which helps enhance the product properties further. Lastly, the finished product will be stored in silos to later be packaged and shipped by transport vehicles [4].

2.2 Rotary kilns

A rotary kiln is a long, cylindrical furnace, with dimensions around 30-100 m long and a diameter of 3-6 m, depending on the process [13]. In Figure 2.2 a schematic is seen of how a rotary kiln operates, courtesy of Adrian Gunnarsson [1]. Here the thick arrows within the kiln represents the bed material flow, whereas the dotted arrows represents the rotation of the kiln and also how the bed material moves within the kiln due to this rotation.

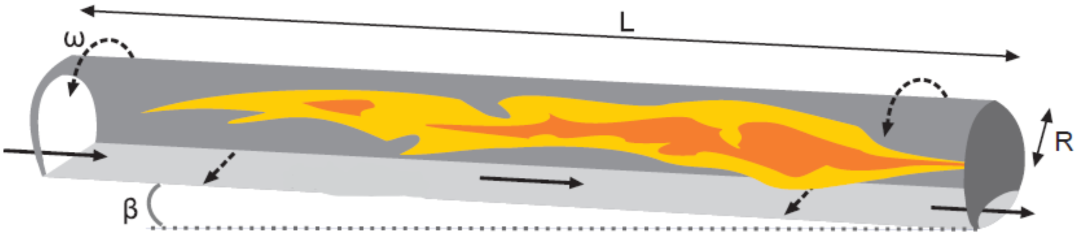

Figure 2.2: Schematic of a rotary kiln, courtesy of Adrian Gunnarsson [1]

Rotary kilns are used in many different solid processes, such as incineration, drying, heating, and cooling. This range of applications are attributed to the rotary kiln's ability to handle varying loads with varying particle size [15]. In the cement process, this is where the chemical clinker formation takes place. In order to ensure a sufficient residence time for the clinker formation processes, rotary kilns are inclined 1-3°, β in Figure 2.2, and rotate with a speed of 1-5 rpm, ω. At the material outlet, which is located at the lower end of the kiln, the kiln is equipped with a burner, which provides energy for the clinker forming reactions. To achieve sufficient heat transfer from the flame to the bed material, the flame should be strongly radiant [13]. The material moves down the kiln, counter current to the combustion gases generated in the burner. The kiln can be divided into sections: the inlet zone where the final calcination takes place, transition zone, burning zone and cooling zone [4]. In the transition zone the temperature of the feed is rapidly increased, and the solid phase reactions take place [16]. The flame is located in the burning zone, and this is where the highest temperatures are found, the material is then cooled down in the cooling zone [4].

A rotary kiln typically consists of an outer shell made of steel, and an inner refractory lining. As temperatures reach up to 1450°C, or even higher for the kiln walls, the refractory lining must be able to withstand and maintain the high temperatures. Mechanical dynamics of the kiln, fuels used, and the chemistry of the cement clinker process creates a destructive environment which the lining must be able to withstand. Therefore, the refractory usually consists of bricks with a certain composition making them able to withstand high temperatures, or sometimes concrete can be used for the lining [13].

2.2.1 Heat transfer in rotary kilns

All three different heat transfer mechanisms occur in a rotary kiln, i.e. radiation, convection, and conduction. Radiation is the most dominating heat transfer mechanism due to the very high temperatures, and it stands for approximately 80% of the total heat transfer in the kiln [10]. When heat is transferred by radiation it is due to electromagnetic waves that are emitted by a radiating particle, this type of heat transfer is in no need of a medium and can be transmitted to an object of any matter of state. In many engineering problems, the radiation is often transmitted from a solid to another solid [17]. However, in a rotary kiln the heat transfer by radiation occurs from participating radiative gases and particles in the flame to the bed as well as to the wall, it also occurs from wall to wall, and from the wall to the bed. Moreover, there is also some radiative heat transfer from the outside of the kiln to the ambient air, and this is considered a loss in the system [10].

The convective heat transfer within the rotary kiln occurs from the gas to the bed material as well as from the gas to the wall [10]. This heat transfer arises when there is a temperature difference between two different materials, causing a driving force between the material at the higher temperature to the one with a lower temperature [17]. The heat loss to the gas surrounding the outside of the kiln is also caused by convection [10].

Moreover, the conductive heat transfer is similar to convection as it occurs due to a temperature difference between materials, but instead it occurs between two solid materials, or within a single solid material. Therefore, the conductive heat transfer in a rotary kiln is between the wall and bed material, but also from the inner wall to the outer wall of the kiln [17]. The overall heat transfer problem in the rotary kiln is hence complex.

2.2.2 Rotary kiln heat transfer modelling tool

Due to radiation being the dominating heat transfer mechanism in a rotary kiln, a model which accurately describes the radiative heat transfer is needed. A heat transfer model has been built in Matlab, at the division of Energy Technology at Chalmers University of Technology. The model is based on the radiative heat transfer model, and employs a discrete ordinates method (DOM) which solves the radiative heat transfer equation (RTE) for a cylindrical enclosure. The volume is divided into cells in the radial (r), axial (z) and angular (ψ) direction, and each cell holds parameter values of temperature, gas concentration and radiative properties for particles and gases. [10].

Because of the contribution from emission, absorption, and scattering, the radiative intensity changes along a direction $\hat{s}$. For a given wave number, ν, the RTE can be described as seen in equation 2.6.

$$\frac{dI_\nu}{ds} = \kappa_\nu I_{b\nu} - (\kappa_\nu + \sigma_{s\nu})I_\nu + \frac{\sigma_{s\nu}}{4\pi}\int_0^{4\pi} I_\nu(\hat{s}_s)\Phi_\nu(\hat{s}_m, \hat{s})d\Omega_m \tag{2.6}$$

Where κ_ν is the absorption coefficient, $\sigma_{s\nu}$ is the scattering coefficient for the present medium, $I_\nu(\hat{s}_\nu)$ is the spectral intensity scattered in to direction $\hat{s}$ from the direction $\hat{s}_m$, $d\Omega_m$ is the solid angle of the small ray in the direction $\hat{s}_m$. Φ_ν is the scattering phase function, $I_{b\nu}$ is the black body intensity at wave number ν [10]. If the medium only consists of gases, with no particles present, the scattering can be neglected [1].

By assuming an overall intensity using grey coefficients to represent gas and particle contributions, the radiative intensity can be solved for using a simplified version of the RTE. A weighted-sum-of-grey-gases (WSGG) model is employed to estimate the grey absorption coefficients for the present gases. The WSGG model applies a set of four grey gases and one clear gas, to represent the actual gas mixture in the kiln. Spectral particle properties are calculated according to Mie theory, and Rayleigh theory is used for soot particles. The radiative intensity is calculated for a set number of directions to each cell node. The RTE is solved in every discrete angular direction and results in multiple coupled partial differential equations, thus an iterative solution process is needed. The iteration process starts at the outer wall at one end of the kiln, for the first iteration assumed values for the angular and reflected intensities are used and then updated with each iteration [10].

The weighted sum of the radiative intensities from all directions, ξ_m, are used to calculate the incident radiative heat flux to the bed material or furnace wall, as described in equation 2.7

$$q_r'' = \sum_{m-1}^{N} I_m w_m \xi_m \tag{2.7}$$

Where w_m is a weight which ensures full coverage of the sphere from a point in which radiation is emitted to. Both the wall and the bed are surfaces exposed to the flame, thus they are subject to the incident radiative heat flux and will be heated, as well as emit radiation [10].

Furthermore, the conductive heat transfer is described by an unsteady-state penetration model. Due to conduction, heat is transferred from the surrounding wall to the bed, hence penetration models for both the wall and bed material are used. When the bed and wall are in contact, they will adopt the same surface temperature, T_{cs}, which is calculated according to equation 2.8.

$$T_{cs} = \frac{(k\rho C_p)_w^{0.5} T_w + (k\rho C_p)_b^{0.5} T_b}{(k\rho C_p)_w^{0.5} + (k\rho C_p)_b^{0.5}} \tag{2.8}$$

Where k is the thermal conductivity, C_p is the specific heat capacity, T is the temperature and ρ is the density of the solid material. Index b and w represent the bed and wall respectively. The heat transferred between the bed and the wall, over a period of $t_{\psi b}$ seconds (i.e., the contact time between a bed segment and the wall), can then be calculated according to equation 2.9.

$$W_{cond,b/w} = A_w X_c \Big[\rho C_p \int_0^{t_{\psi b}} \int_{d_T=0}^{d_T=0.99} \delta T(\delta, t) d\delta dt\Big]_{b/w} \tag{2.9}$$

Where d_T is the temperature distribution within the thermal penetration depth of the bed or wall, δ. X is the volume portion of the bed consisting of solid material, and A is the surface area [1].

The convective heat transfer occurs between the passing gas (index g) and the surfaces of the bed and wall, and can be described by the heat transfer coefficients obtained from Gorog et al. [18], as seen in equations 2.10 and 2.11.

$$h_{g\to w} = 0.036\frac{k_g}{D} Re_D^{0.8} Pr^{0.33} (\frac{D}{L})^{0.0055} \tag{2.10}$$

$$h_{g\to b} = 0.4 G_g^{0.62} \tag{2.11}$$

Where D and L are the diameter and length of the kiln, G_g is the mass flux of gas passing through the kiln, Re is the Reynolds number and Pr is the Prandtl number.

The heat losses in the system are, as mentioned in the previous section, due to convection and radiation occurring from the outer wall of the kiln to the surrounding gas and surfaces of the kiln. In the model these are accounted for with the outer temperatures of the kiln, and the outer convective coefficient, h_o, which is described by following equation

$$h_o = \frac{k_{g_o}}{D_o} 0.11\{(0.5 Re_w^2 + Gr_o) Pr_o\}^{0.35} \tag{2.12}$$

This expression is a correlation for rotating cylinders, and here k_{g_o} is the thermal conductivity of the surrounding gas, Re_ω is the Reynolds number considering the rotational speed of the kiln, Gr_o is the Grashof number and Pr_o is the Prandtl number both calculated for the outside of the kiln [19].

In the model, the bed material is treated with a simplified mixing model due to its movement when the kiln rotates. This is further presented in Figure 2.3 below, where it can be seen that the bed is divided into two parts, where the bottom part is moving with the rotation of the kiln until it reaches the top, and thereby ends up in the upper part of the bed, where it then falls down the opposite direction. Therefore, one could describe the bottom part of the bed as solely moving along with the rotation of the kiln, but that it is "non-moving" in relation to the wall, and therefore no mixing occurs in this part. Since the bottom part of the bed is not moving in relation to the wall, no slip to the wall is assumed in the model. Furthermore, since the top layer of the bed is in motion, it is assumed that perfect mixing occurs in each of these surface layers cells with different angular positions, it is also assumed that the bed material in each surface layer position is isothermal. Figure 2.3 also describes the different heat transfer mechanisms and where these occur. In the two layers of the bed the bottom part receives heat through conduction from the wall, whereas the upper part receives heat from convection and radiation [1]. The bed material compositions are defined by the heat of reaction which are calculated by enthalpy differences as a function of the temperatures of the bed.

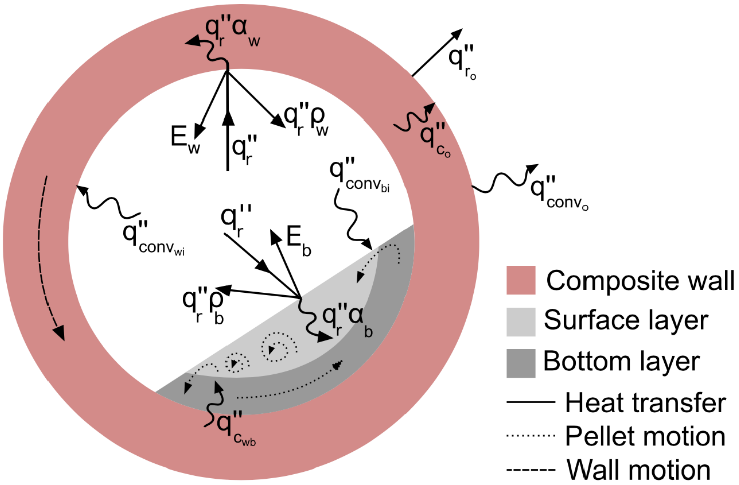

Figure 2.3: Cross-section of a rotary kiln, describing the different heat transfer mechanisms and also the mixing and motion of the bed, courtesy of Adrian Gunnarsson [1]

An iterative process is required to solve the RTE and calculate the bed and wall temperatures in each cell. The model requires profiles of gas and particle temperatures, particle concentrations and gas composition. Using this input, the model then calculates the radiative intensities in all directions, and the incident radiative heat flux to all the surfaces. The bed and wall temperatures are updated for each axial position, starting at the inlet of the bed. The outer wall temperature is calculated, as well as the heat loss and the inner wall temperature is updated. Over a period of t_ψ seconds, the wall turns one angular step, the top layer of the bed is mixed, the bottom layer of the bed is moved and the bed temperature is updated. Chemical reactions are accounted for and if the bed temperature has converged, the bed moves one axial step. At the end of the kiln all bed temperatures are updated, and the next iteration step is to find the updated radiative heat flux to the bed and wall surfaces. Then followed by updated wall and bed temperatures. Finally, the model has converged when the radiative intensities and surface temperatures all have converged [10]. For a more detailed description of the modelling tool see [10].

2.3 Plasma torches

Plasma is defined as an ionised gas, and is often referred to as the fourth state of matter [20]. Plasma can be generated by applying an electric current through a gas. In industry, two different modes of plasma are typically used, thermal plasma, also called equilibrium plasma, and non-equilibrium plasma. A thermal plasma is generated by accelerating electrons between two electrodes, in a gaseous environment. As the electrons are sped towards an anode they excite the atoms in the gas. The excitation causes collision and ionisation, and the additional electrons which are freed by the ionisation are accelerated towards the anode and cause further ionisation. This results in a highly conductive gas where the current can pass in the form of an electric arc. Equilibrium is reached when the gas particles have gained the same energy as the electrons. Thermal plasmas are characterised by a high energy density, and the plasma gas is generated at pressures above 10 kPa. Temperatures in the plasma typically lie within the range 2000-20 000 K. Non-equilibrium plasmas are low pressure plasmas, produced under vacuum. They are characterised by high electron temperatures, and low ion and neutral temperatures [9].

Plasma torches are used to generate thermal plasmas. A plasma torch typically consist of a cathode and an anode, which are shaped like a nozzle, and the two electrodes are separated by an insulator or spacer. Tungsten is the most commonly used cathode material, and copper is generally used for the anode [21]. They operate using either direct current or alternating current, although direct current is more commonly used since the plasma tends to be more stable and easy to control [4]. As the gas passes through the electrode gas, a DC arc is established which results in a high temperature plasma with a high velocity. The arc is constricted by electromagnetic forces and gas stabilisation. Because the arc will represent the path of least resistance, it passes from the cathode through the nozzle to the anode. DC thermal plasma torches are most commonly used as they can sustain more stable and longer arcs than AC torches, and they also have independent current and voltage control. This results in a reduced electrode consumption, less electrical disturbances and reduced noise levels [21]. Thermal plasma torches can further be classified into transferred and non-transferred arcs. In a non-transferred arc torch, the anode and cathode are located in the torch, as visualised in Figure (2.4). This will cause the arc to be established between these two electrodes. Transferred arc torches will instead have one electrode located outside the torch [22].

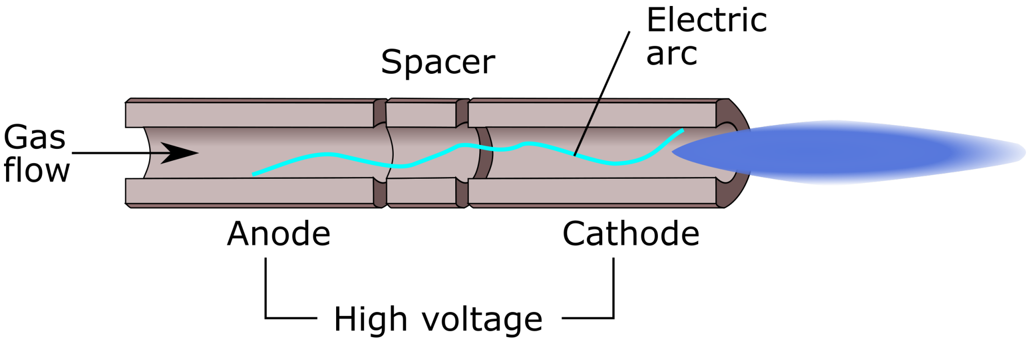

Figure 2.4: Schematic of a non transferred arc plasma burner, courtesy of Adrian Gunnarsson

Different gases, so called working gases, can be used to generate the plasma, with the most commonly used gases being helium, nitrogen, argon, air, and hydrogen. Which gas to use depends on characteristics such as reactivity and gas enthalpy, as well as cost and availability. In order to get a stable arc, the gas flow rate and the electric power to the plasma must be balanced properly. When the current is built up, the gas flow must be carefully adjusted to prevent the arc from blowing out [21]. Using CO_2 as the plasma gas has the advantage of being chemically compatible with the cement production process [4], as well as having the property of radiating heat. As has previously been examined by Heidelberg Materials Sweden and previous master thesis projects, the relevant option for Heidelberg Materials Sweden's process is a non-transferred thermal plasma [4].

2.3.1 Carbon dioxide environments in cement processes

It is expected that a change in the gas environments within different steps in the cement process, especially the rotary kiln and calcine tower, will affect the outcome of the process. Especially, an increase of carbon dioxide gas in the system, and therefore an increase of the carbon dioxide partial pressure, will have some impact on the process [4]. Khinast *et al.* (1995) stated that the reaction rate of the decomposition of limestone decreases when the CO_2 partial pressure is increased [23]. Moreover, Wang *et al.* (2019) stated that an increased CO_2 partial pressure also increases the temperature within the system, which in turn favours the calcination process, making the reaction rate faster [24]. It is hard to tell exactly how the cement process will change when the gas environment is altered, but it should be considered when studying these types of process modifications.

2.3.2 Difference between plasma gas and coal flame

An electric thermal plasma driven by carbon dioxide as the working gas in a carbon dioxide environment will produce different species from the dissociation of the CO_2. These are, besides CO_2, also carbon monoxide, CO, and oxygen in both its free form and as a molecule, O and O_2. Therefore no formation of nitrogen oxides will occur, which is one difference when comparing with a coal flame combusted with air since nitrogen is present in these cases, given no leakage of air into the system.

Another difference is also the lack of particles in the plasma gas case. In a coal flame there are ash and fuel particles present, and soot particles are formed during combustion, which all radiate heat and therefore contribute to the heat transfer within the kiln [4]. Both particles and gases emit and absorb radiation. Particles can be characterised as broad-band emitters, which means that they emit and absorb radiation across most of the spectrum. Unlike particles, gases emit and absorb radiation at a smaller range of the spectrum [1]. Hence, one can predict a decrease in the radiation contribution in a carbon dioxide plasma due to this lack of particles, however it is important to note that the species in the plasma will radiate to some extent but still not as much as the particles in a coal flame. This might imply an effect of the radiative heat transfer in a rotary kiln used in cement industry, since the decrease in radiative heat transfer can affect the clinkerisation [4].

A significant difference between a plasma gas and a coal flame are the maximum temperatures that they each can reach. Attempts to increase the temperature of the coal flame in a cement rotary kiln has been made by using oxygen enriched air and swirling flow. The highest temperatures reached was around 2300 K at the burner [25], which is substantially lower than the temperatures a plasma can reach, as mentioned in section 2.3.

2.4 Scaling of thermal processes

When scaling combustion processes, the most common two principles are: constant velocity scaling and constant residence time scaling. Constant velocity scaling implies that the velocity of the combustion gases are kept constant, while constant residence time scaling means that the mixing time, which is representative of the flame residence time, is kept constant. These two principles both aim at maintaining the fractional degree of mixing over the normalised length of the combustor. Even though constant residence time scaling achieves a greater degree of similarity for slower processes, it is rarely applied due to the fact that practical problems such as pressure drops and low velocities may arise. Thus, constant velocity scaling is often the preferred method [26].

However, simple geometrical scaling has been proven to not be sufficient for rotary kilns. Instead, other factors such as residence times, gas velocities and dimensionless numbers should be considered when scaling heat transfer processes. For the lower gas flows in a smaller kiln, laminar conditions may occur, while the gas flow is generally turbulent in kilns of a larger size, which could cause problems when scaling the heat transfer processes [27]. The Reynolds number is a dimensionless number and is used to check the conditions of a flow in a tube, it is calculated according to equation 2.13.

$$Re = \frac{vD_i}{\nu} = \frac{\rho v D_i}{\mu} \tag{2.13}$$

Where v is the gas velocity, D_i is the inner diameter of the tube, and ν is the kinematic viscosity. μ is the dynamic viscosity, ρ is the density of the fluid. For flows in circular tubes, the critical Reynolds number is 2300, meaning that flows with Re > 2300 can be considered turbulent [28].

A further challenge for kilns of smaller scales with lower mass flow rates is satisfying design requirements such as the residence time of the bed material, Froude, and Biot numbers, while maintaining a good utilisation of the heating zone. [29].

3

Method

The method describes how the results were achieved, which was done by literature studies, gathering of data, model developments, initial scaling, simulation, and iteration processes. The principal emphasis was placed on the model development, which included developing the temperature profile of a plasma gas and calibrating the heat transfer model to conform to a carbon dioxide environment with high temperatures.

3.1 Initial scaling of process data

Prior to conducting simulations of different rotary kiln demonstration scale cases, an initial scaling of relevant process data was done. A schematic of the present cement process can be seen in Figure 3.1. The process data to be scaled was the volumetric flow of the secondary carbon dioxide gas, called "Secondary air" in Figure 3.1, and the maximum temperature of the plasma at the inlet of the burner. Moreover, the heat transfer model has been updated to simulate a smaller scale kiln with an 8 MW plasma burner in a carbon dioxide environment.

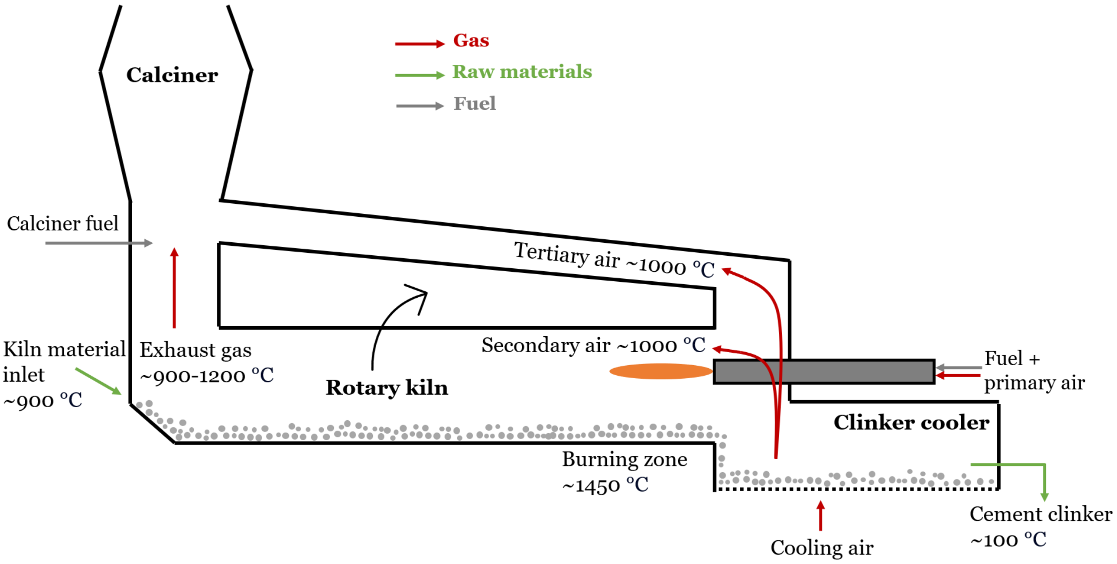

Figure 3.1: Schematic of the calciner, rotary kiln, and cooler in the present cement process at Heidelberg Materials Sweden

3.1.1 Scaling of secondary gas flow

The secondary carbon dioxide gas flow was initially scaled by assuming that the cooling effect in the cooler in the current process is kept constant when changing the gas from air to carbon dioxide, and therefore assuming that the cooling effect is not dependent on the gas flow. This is described by the following equation.

$$Q_{cooler,air} = Q_{cooler,CO_2} \tag{3.1}$$

The heat balance can further be described as:

$$H_{air,out} - H_{air,in} = H_{CO_2,out} - H_{CO_2,in} \tag{3.2}$$

Where H is the enthalpy of the gases at the outlet and inlet respectively. The inlet was set to the reference temperature of 298 K, and at this temperature the enthalpies for both air and CO_2 is zero, which simplified equation 3.2 further. The unit of enthalpy used in equation 3.2 was *kJ/mol*. In order to solve for a volumetric flow with the unit Nm^3/h, the heat balance in equation 3.2 was rewritten to equation 3.3.

$$\dot{V}_{air} \cdot \dot{n} \cdot m_{production} \cdot \Delta H_{air} = \dot{V}_{CO_2} \cdot \dot{n} \cdot m_{production} \cdot \Delta H_{CO_2} \tag{3.3}$$

Here, $\dot{V}_{gas}$ is the volumetric flow of secondary gas in $\mathrm{Nm^3}$/kg clinker, $\dot{n}$ is the standard molar flow per one normal cubic meter gas, which at standard conditions is 44.64 $\mathrm{mol/Nm^3}$. Moreover, $m_{production}$ is the clinker production of the process in kg clinker/h.

Equation 3.3 simplifies to:

$$\dot{V}_{CO_2} = \frac{\dot{V}_{air} \Delta H_{air}}{\Delta H_{CO_2}} \tag{3.4}$$

The secondary gas flow of air, $\dot{V}_{air}$, in the current process at Heidelberg Materials Sweden was known, and the enthalpies, ΔH, for both air and CO_2 at the cooler outlet temperature was collected from tables, hence the only unknown parameter was the secondary gas flow of CO_2, $\dot{V}_{CO_2}$, which could be solved for. The unit for the secondary gas flow used in the heat transfer model is Nm^3/h, thus the gas flow acquired from equation 3.3 was multiplied with the clinker production rate in $kg_{clinker}/h$ the achieve the desired unit.

3.1.2 Scaling of maximum plasma temperature

An initial temperature of the CO_2-plasma at the burner inlet was investigated in order to map the temperature profile of the plasma gas. First, gas flow data from several plasma torches with different sizes were collected, these were provided by ScanArc. The largest plasma size from the provided data was further investigated, and it was assumed that the enthalpy of this plasma would be the same for the utilised 8 MW plasma in the demonstration scale of the rotary kiln. The enthalpy was calculated by following equation:

$$H_{8MW} = \frac{\frac{\eta P}{\dot{V}}}{\rho_{CO_2}} \tag{3.5}$$

where η was the efficiency of the plasma torch, P was electrical power input to the plasma, $\dot{V}$ the volumetric primary gas flow entering the torch, both provided by ScanArc. From the enthalpy, the maximum temperature could be evaluated. It was accomplished with additional data provided by Heidelberg Materials Sweden, produced with FactSage, where the data described a table of dissociation enthalpies at different temperatures of carbon dioxide, presented in Appendix B. The temperature in this data that matched the size of the enthalpy calculated in equation 3.5 was then set as the maximal plasma temperature at the burner inlet.

3.1.3 Scaling of initial dimensions of the rotary kiln

An initial scaling of the dimensions was performed in order to attain a starting guess of the radius and length of the rotary kiln. The scaling was done under the assumption of a constant ratio of the total volumetric gas flow and the cross-sectional area of the kiln, a type of constant-velocity scaling, presented in the equation below.

$$\frac{\dot{V}_{fullscale}}{A_{fullscale}} = \frac{\dot{V}_{8MW}}{A_{8MW}} \tag{3.6}$$

Where both $\dot{V}_{fullscale}$ and $\dot{V}_{8MW}$ were the sum of the primary and secondary gas flow in the full scale and 8 MW scale respectively. Since the left hand side in equation 3.6 and V_{8MW} were known, A_{8MW} could be solved for. With this cross-sectional area for the 8 MW demonstration scale kiln, the initial radius could then be found.

The initial length of the kiln was then found by assuming a constant length to radius ratio from the full scale kiln and applying this to the demonstration kiln, similar to equation 3.6 above. This scaling does not relate to the previously mentioned constant-velocity scaling, instead it can be described as a linear scaling from the original full scale kiln, and was used as to attain a preliminary length of the demonstration kiln. Since all was known except for the length of the 8 MW kiln, this was solved for and the initial scaling was done. These dimensions were then used in the initial simulations and used as a reference case.

3.1.4 Checking of flow properties

In order to determine whether the gas flow in the initially scaled rotary kiln (also referred to as the reference case rotary kiln) was laminar or turbulent, the Reynolds number in the kiln was calculated using Equation 2.13.

The Reynolds number was computed for all cells in the kiln, since the temperature is not constant, the properties of the gas is not constant, which yields different Reynolds numbers throughout the kiln. Thus an average value of the Reynolds number for all cells was used. The value for the inner diameter that was used was the one scaled in section 3.1.3, the gas velocity was calculated as the sum of the primary and secondary gas flows, divided by the cross-sectional area of the kiln. Data for the dynamic viscosity and the density was gathered from The National Institute of Standards and Technology (NIST) and linearly extrapolated for temperatures above 2000 K.

3.2 Overall heat balance

To calculate an estimated temperature of the flue gas, a simplified heat balance over the kiln was set up analytically. Note that the bed material and gas passes in the kiln counter-current. The bed material enters the kiln at an inlet bed temperature, $T_{bed,in}$, and must reach an outlet bed temperature, $T_{bed,out}$, in order for the clinkerisation reactions to be completed. When $T_{bed,out}$ is achieved the bed material enters the cooler, downstream the process. The secondary gas from the cooler enters with an inlet temperature at the opposite end of the kiln compared to the bed material, $T_{secondary,in}$. The primary gas enters with the plasma, also at the opposite end of the kiln. At the centre of the plasma torch, the plasma gas reaches a maximum temperature, T_{plasma}, as calculated in section 3.1. Throughout the kiln the primary and secondary gas mixes, and before entering the calcine tower the secondary gas and the plasma gas are assumed to be fully mixed, and reaches the outlet temperature, $T_{fluegas,out}$, which is unknown. In Figure 3.1, $T_{fluegas,out}$ is the same as the stream called "Exhaust gas". Heat enters the system with the plasma, Q_{plasma}, and the secondary gas, $Q_{secondary,in}$, and leaves through the flue gas, $Q_{fluegas}$, and the bed, Q_{bed}, as well as through radiation losses, $Q_{radiation}$. Convection losses were assumed negligible for this initial heat balance. Equation 3.7 describes the heat balance over the kiln.

$$Q_{plasma} + Q_{secondary,in} = Q_{bed} + Q_{fluegas} + Q_{radiation} \tag{3.7}$$

The heat transferred to the bed is described by equation 3.8. The mass flow of the secondary gas, $\dot{m}_{secondary}$, and for the plasma burner, $\dot{m}_{plasma}$, were calculated as described in section 3.1. The mass flow of the cement, $\dot{m}_{production}$, was the target production rate for the demonstration scale kiln. The radiation losses are described in equation 3.9. A is the surface area of the outside of the kiln where an initial estimation of the kiln's dimension was used, σ is the Stefan-Boltzmann's constant, T_{sur} is the temperature of the air surrounding the outside of the kiln, and ϵ the emissivity of the kiln.

$$Q_{bed} = \dot{m}_{production} Cp_{cement}(T_{bed,out} - T_{bed,in}) \tag{3.8}$$

$$Q_{rad} = \epsilon\sigma A T_{sur}^4 \tag{3.9}$$

Equation 3.10 describes the energy in the secondary gas entering the kiln. Q_{plasma} was set to the maximum power of the plasma burner. The heat leaving the kiln via the flue gas is described by equation 3.11

$$Q_{secondary,in} = \dot{m}_{secondary} Cp_{CO_2,\,in} T_{secondary,in} \tag{3.10}$$

$$Q_{fluegas} = (\dot{m}_{plasma} + \dot{m}_{secondary})Cp_{CO_2,\,out}T_{fluegas,out} \tag{3.11}$$

Equations 3.8-3.10 were substituted into equation 3.7 and 3.11 to solve for the unknown flue gas temperature, $T_{fluegas,out}$.

3.3 Plasma gas temperature profiles

In this section the development of the plasma temperature profile is described. In the original model, the temperature profile of the coal flame was described by vectors at different axial locations throughout the kiln, where the temperatures in between these locations were linearly interpolated. In the development of the model, conducted with this master thesis work, the plasma temperature profile is instead described by a polynomial function, based on experimental data of a 50 kW carbon dioxide plasma. The experimental data provided estimated temperatures at different radial and axial positions within the cross-section of the 50 kW plasma gas.

3.3.1 Initial temperature profile

The initial temperature profile of the plasma gas was determined, based on experimental finding of the temperature profile of a 50 kW carbon dioxide plasma. The temperature profile data described how the temperature decreased in radial and axial directions from the plasma generator position to the ambient air, as visualised in equation 3.12. The centre temperatures, $T_{c,j}$, are marked in red, the rest of the plasma gas temperatures, $T_{i,j}$, in blue, and the surrounding gas, T_{sur} in black. From the experimental data, it can be seen that the plasma gas assumes a conical shape, with its apex at the burner position and widening further into the kiln. The data provided was only for half of the conical shape, but it is assumed to be symmetrical around its horizontal centre axis.

$$T = \begin{bmatrix} T_{c,1} & T_{c,2} & T_{c,3} & T_{c,4} & T_{c,5} & T_{c,6} & T_{c,7} & T_{c,8} \\ T_{21} & T_{22} & T_{23} & T_{24} & T_{25} & T_{26} & T_{27} & T_{28} \\ T_{31} & T_{32} & T_{33} & T_{34} & T_{35} & T_{36} & T_{37} & T_{38} \\ T_{sur} & T_{42} & T_{43} & T_{44} & T_{45} & T_{46} & T_{47} & T_{48} \\ T_{sur} & T_{sur} & T_{sur} & T_{54} & T_{55} & T_{56} & T_{57} & T_{58} \\ T_{sur} & T_{sur} & T_{sur} & T_{sur} & T_{65} & T_{66} & T_{67} & T_{68} \\ T_{sur} & T_{sur} & T_{sur} & T_{sur} & T_{sur} & T_{76} & T_{77} & T_{78} \\ T_{sur} & T_{sur} & T_{sur} & T_{sur} & T_{sur} & T_{sur} & T_{87} & T_{88} \\ T_{sur} & T_{sur} & T_{sur} & T_{sur} & T_{sur} & T_{sur} & T_{sur} & T_{98} \end{bmatrix} \tag{3.12}$$

In order to scale up the temperature profile to an 8 MW plasma, the temperatures in the matrix were converted to temperature ratios, where these ratios were percentages of the temperatures at the centre of the plasma gas. It was completed by first describing the axially decreasing temperatures in the centre positions, starting from the plasma generator position, which is the maximum temperature of the plasma gas. The centre temperature of the plasma gas was written as a linear function of the maximum temperature at the plasma gas outlet. This was done by dividing the centre temperature at the axial end of the plasma gas, $T_{c,8}$, with the maximum temperature at the generator, $T_{c,1}$. Thus a linear function of the axial $(z_{c,j})$ positions was fit to $T_{c,1}$ and $T_{c,8}/T_{c,1}$, see equation 3.13.

$$T_{c,j} = \frac{T_{c,8}}{T_{c,1}} \cdot z_8 \tag{3.13}$$

The relationship between the temperature at the end of the plasma gas and the generator position, $T_{c,8}/T_{c,1}$, is assumed to be the same for the 8 MW plasma as for the 50 kW. Thus, by knowing the maximum temperature at the generator, the centre temperatures can be found for the 8 MW plasma.

The decreasing temperatures in each radial position was described by comparing the temperature at an axial plasma centre position, $T_{c,j}$, to the temperature at a certain radial position below the centre position, $T_{i,j}$, and dividing this with the difference between the centre temperature, $T_{c,j}$, and surrounding temperature, T_{sur}. Then, a temperature ratio, $x_{i,j}$, for that certain position was attained described by the following equation, where i indicates the number of radial positions and j the number of axial positions.

$$x_{i,j} = \frac{T_{center} - T_{radial\,position}}{T_{center} - T_{surrounding\,gas}} = \frac{T_{c,j} - T_{i,j}}{T_{c,j} - T_{sur}} \tag{3.14}$$

The temperature profile described by the temperatures ratios per length unit for the 50 kW plasma were then assumed to be the same for an 8 MW plasma. To scale up the temperature profile to a 8 MW plasma, as to retrieve the dimensions of the 8 MW plasma, it was assumed that the ratio between volumetric flow and radius would be kept the same for both plasma sizes, as described by equation 3.15 below.

$$\frac{\dot{V}_{50kW}}{R_{50kW}} = \frac{\dot{V}_{8MW}}{R_{8MW}} \tag{3.15}$$

Since the volumetric flows were known for both plasma sizes, and the radius for the 50 kW plasma was known but unknown for the larger size, the larger radius was found by solving for R_{8MW}.

To scale the length of the 8 MW plasma the length to radius ratio was kept constant between the two plasma sizes, with an equation set up similar to equation 3.15. All variables were known except the length of the 8 MW plasma, which could be solved.

The total length and radius of the 8 MW plasma were now known, and the temperature profile of the plasma gas, at different axial and radial positions, could be computed with help of the previously calculated temperature ratios, by keeping the temperature ratios constant and calculating the temperatures at all positions within the plasma. The temperatures within the plasma, $T_{radialposition}$ were calculated according to equation 3.14, with x_{radial} being the same as for the 50 kW plasma, and T_{center} and $T_{surrounding\,gas}$ adjusted for the 8 MW plasma and the specifications within the demonstration scale kiln.

3.3.2 Polynomial function

The matrix containing the temperature ratios, as described in section 3.3.1 was used to scale up the temperature profile from the measurement data of the 50 kW plasma to the 8 MW plasma. The plasma was assumed to maintain it's conical shape when scaled up to 8 MW.

In order to implement the temperature ratios in the heat transfer model, a polynomial function of the radial and axial positions describing the temperature ratio in each cell, was developed. The polynomial was then used to find the temperature ratio in each position within the plasma gas, for different kiln dimensions. As described in section 3.3.1, a matrix containing the temperature ratios per length unit was acquired for the 50 kW plasma, and is assumed to be the same for the 8 MW plasma, as visualised in equation 3.16, where x_{ij} are the temperature ratios in each cell calculated according to equation 3.14.

$$X = \begin{bmatrix} x_{c,1} & x_{c,2} & x_{c,3} & x_{c,4} & x_{c,5} & x_{c,6} & x_{c,7} & x_{c,8} \\ x_{21} & x_{22} & x_{23} & x_{24} & x_{25} & x_{26} & x_{27} & x_{28} \\ x_{31} & x_{32} & x_{33} & x_{34} & x_{35} & x_{36} & x_{37} & x_{38} \\ x_{sur} & x_{42} & x_{43} & x_{44} & x_{45} & x_{46} & x_{47} & x_{48} \\ x_{sur} & x_{sur} & x_{sur} & x_{54} & x_{55} & x_{56} & x_{57} & x_{58} \\ x_{sur} & x_{sur} & x_{sur} & x_{sur} & x_{65} & x_{66} & x_{67} & x_{68} \\ x_{sur} & x_{sur} & x_{sur} & x_{sur} & x_{sur} & x_{76} & x_{77} & x_{78} \\ x_{sur} & x_{sur} & x_{sur} & x_{sur} & x_{sur} & x_{sur} & x_{87} & x_{88} \\ x_{sur} & x_{sur} & x_{sur} & x_{sur} & x_{sur} & x_{sur} & x_{sur} & x_{98} \end{bmatrix} \tag{3.16}$$

At the centre of the plasma gas, the first row, the temperature ratio is described by the polynomial function as zero in each axial position, as the temperature instead equals the centre temperature. This can be seen when rewriting equation 3.14 to equation 3.17 by substituting $T_{i,j}$ for $T_{c,j}$.

$$x_{c,j} = \frac{T_{c,j} - T_{c,j}}{T_{c,j} - T_{sur}} = 0 \tag{3.17}$$

Outside of the plasma gas, which is contained by the surrounding gas, the temperature ratio equals one since the temperature at all these positions are assumed to be that of the secondary gas, as seen in equation 3.18.

$$x_{sur} = \frac{T_{c,j} - T_{sur}}{T_{c,j} - T_{sur}} = 1 \tag{3.18}$$

Each position within the plasma gas was rewritten as a percentage of the total plasma dimension. Thus, instead of the temperature ratios being confined to a specific length position, they were assigned to a percentage of the total plasma gas radius and plasma gas length.

For example, in the initial temperature profile of the 50 kW plasma, at 25% of the total radius, corresponding to *i=3*, and 14% of the total plasma length, at axial position *j=2*, the corresponding temperature ratio is 0.65. In other words, the difference between the radial temperature and the centre temperature in that radial position equals 65% of the difference between the centre temperature in the same radial position and the temperature of the surrounding gas. This can also be written as:

$$x(r = 0.25R_{cone}, z = 0.14L_{cone}) = x_{32} = \frac{T_{c,2} - T_{32}}{T_{c,2} - T_{sur}} = 0.65 \tag{3.19}$$

The temperature ratio profile acquired in section 3.3.1 was assumed to be constant for all plasma sizes, thus making it possible to calculate the temperatures at all cells within the plasma gas from these temperature ratios, for different plasma dimensions assuming a conical shape. Measurement data was available for eight axial positions and nine radial positions within the plasma, rendering an initial matrix with nine rows and eight columns. To be able to increase the number of cells in the matrix, a polynomial function was fitted for each axial position, describing the temperature ratios as a function of the radial positions. A total of eight one dimensional polynomials were generated, one for each axial position.

The next step was to fit a two dimensional polynomial which would describe the temperature ratios as a function of both the radial and axial positions. This was achieved using the Curve fitting tool in Matlab. Since the radial measurement points were very few, especially for the first half of the plasma gas, the radial polynomials were used to find temperature ratios for nine radial positions at all eight axial positions. This generated a nine by eight matrix, and together with a nine by eight matrix containing all corresponding radial positions and a matrix of the same size containing the axial positions, a polynomial function was fitted with the Curve fitting tool. This polynomial gave the temperature ratios, x in all cells covered by the plasma gas, as a function of the radial and axial poistions within the plasma gas. The temperature ratios are based on the measurement data from the 50 kW plasma, which could then be used to calculate the temperature for the 8 MW plasma gas in all cells as described, by rewriting equation 3.14 to equation 3.20. For this calculation, x in each position was kept constant from the 50 kW plasma, the maximum temperature the calculated 8 MW plasma generator temperature. The surrounding temperature is the temperature of the carbon dioxide from the cooler.

$$T_{i,j} = T_{c,j} - x_{i,j}(T_{c,j} - T_{sur}) \tag{3.20}$$

3.4 Updating the heat transfer model

The heat transfer model was updated to fit the case with a carbon dioxide plasma burner. Several adjustments had to be made, the temperature profile of the plasma was implemented, as well as adding more thermodynamic data for higher temperatures, and to account for a carbon dioxide environment. The total energy balance over the kiln was closed, as this was not previously done in the model.

3.4.1 Implementation of the plasma temperature in the model

To implement the temperature model of the plasma in the heat transfer model of the rotary kiln, the polynomial function generating the temperature profile and the linear equation describing the centre temperature were written as two separate functions in Matlab.

The temperature profile was generated in the heat transfer model by first calculating how many cells the plasma gas occupies axially, depending on the cell discretization of the furnace volume. The number of cells covered by the plasma was then used as an input to a function generating the linearly decreasing centre temperature line. The Polyfit function in Matlab was used to fit a linear equation from the burner temperature down to 71.9% of the burner temperature, which was the ratio calculated for the 50 kW plasma as described by equation 3.13, over the number of axial cells. The output from this function was a vector containing the temperatures in each cell of the centre of the plasma.

The centre temperatures together with the radial and axial positions in the kiln were used as an input to a specific temperature profile function in the modelling tool. In the temperature profile function, it was first checked if the radial and axial positions were within the dimensions of the plasma gas, since the temperature ratios given by the polynomial function described in section 3.3.2, is only valid within the dimension of the conical plasma gas. This was done by dividing the radial positions with the set radius of the plasma, and the axial positions with the length of the plasma to find the corresponding positions within the plasma. If the radial and axial positions were found to be located within the plasma dimensions, the polynomial was used for that position. If the position was outside of the plasma, the temperature ratio was set to 1, according to equation 3.18. The polynomial function was then used to calculate the temperature ratios in each cell. Together with the centre temperatures, the temperature in each cell is calculated by using equation 3.20. Thus the temperature profile function gave the output as a matrix containing the temperatures in each axial and radial position of the plasma, as visualised in equation 3.12.

The linear equation describing the centre temperature and the polynomial giving the temperature profile were implemented in the model, replacing the previous method where three temperature vectors were used to set temperature values at five radial positions. From the axial end of the plasma to the outlet of the kiln, the gas temperature was interpolated linearly between each radial temperature to the flue gas temperature, due to the flue gas outlet stream was assumed to be a plug flow with a homogeneous temperature.

Since the mass flow of the secondary gas was adjusted according to the production rate of cement, as described in section 3.1, this calculation was also implemented in the model. This was done as a function which takes the production rate as an input and gives the secondary gas flow as an output. By doing this, the secondary gas flow was adjusted according to the production rate.

3.4.2 Closing the energy balance

Since the model did not close the energy balance over the kiln, this was implemented to improve the accuracy of the model. This was done iteratively by guessing a flue gas temperature, calculate an updated temperature from an energy balance and repeat until the total heat demand of the kiln met the energy input from the plasma torch. The total heat demand in the kiln was calculated according to equation 3.21.

$$Q_{heat\,demand} = Q_{to\,bed} + Q_{conduction\,losses} + Q_{to\,gas} \tag{3.21}$$

Where $Q_{to\,bed}$ was compiled of the heat transferred to the bed through conduction, convection, and radiation to the bed. The conduction losses $Q_{conduction\,losses}$ were the sum of the conduction losses from under the bed and through the kiln walls to the outside of the kiln, and $Q_{to\,gas}$ was the total energy transferred to the gas. In the model, this was done by initiating a guessed start value for the flue gas temperature, called exhaust gas in Figure 3.1, and looping over the entire model. The total heat demand was compared to the heat input, which was set as constant at 8 MW provided by the plasma burner, with an efficiency of 90%. If the difference between the total heat demand and input was larger than a set tolerance, the flue gas temperature was updated, until the heat demand equals the input and the energy balance was closed.

3.5 Simulations

Simulations were run in order to find the optimal dimensions of the demonstration scale kiln. A reference case was set up, based on the initial scaling calculations. Different parameters were adjusted to observe the effect each parameter had on the heat transfer, and the possibility to heat the bed sufficiently or not. Adjustments were made until dimensions were found which ensured sufficient heat transfer for the clinkerisation processes in the kiln. A simulation of the current full scale kiln with a coal flame was run to compare the results from the plasma cases.

3.5.1 Coal case

In Heidelberg Materials Sweden's current process, the full scale kiln is run with a coal flame as a heat source. A simulation of this case was run to gather data, which could be used to compare the performance of the demonstration scale kiln with the current kiln. The dimensions were set to those of the full scale kiln, see Table 3.1. The most important parameters to compare the coal case to the plasma case with was the residence time, temperatures of the bed material and gas, as well as the heat balance in the kiln. This simulation was run in an earlier version of the heat transfer model where the energy balance, see section 3.4.2, was not yet closed. Thus, the flue gas temperature was set to 1200 °C.

Table 3.1: Parameters used in the coal case

Parameters	Set values
Production rate [ton/h]	227
Length [m]	80
Radius [m]	2.1
Projected surface area of particles [m^2/kg]	153.61
Secondary gas flow [Nm^3/h]	144 590
Secondary gas inlet temperature [°C]	980
Flue gas temperature [°C]	1200
Bed volume portion [%]	10
Rotational speed [rpm]	3.8

3.5.2 Reference case

The settings for the reference case are presented in Table 3.2 below. The initial production rate was 10 ton/h, the length and radius were set to 18 m and 0.48 m respectively as these were the results of the initial dimensions calculated in section 3.1. The plasma length was set to 1.789 m since this was the results from the scaling of the plasma temperature profile. Furthermore, the plasma was assumed to be positioned and elongated along the centre line of the rotary kiln, i.e. the plasma gas. Therefore, the angle was set to 0° from the rotary kiln axis since the plasma was non-tilted. No particles were present in the reference case hence the value of the projected surface area of particles was set to 0 m^2/h. The last three parameters, inlet temperature of the secondary gas, bed volume portion, and rotational speed were held constant throughout all simulation cases.

Table 3.2: Parameters used in the reference case

Parameters	Set values
Production rate [ton/h]	10
Length [m]	18
Radius [m]	0.48
Plasma length [m]	1.789
Plasma angle [°]	0
Projected surface area of particles [m^2/kg]	0
Secondary gas flow [Nm^3/h]	3984
Secondary gas inlet temperature [°C]	980
Bed volume portion [%]	10
Rotational speed [rpm]	3.8

3.5.3 Simulation cases

Starting from the reference case, simulations were run where different design and operational parameters were altered, and the effects each parameter had were evaluated. Which parameters that were changed and within what ranges are shown in Table 3.3. For each simulation case, only one parameter was changed and the other parameters were kept constant as for the reference case. To find which parameter values that provided sufficient heat transfer conditions, the best case from each simulation was selected. Which case was regarded as the best was based on the bed outlet temperature, where the case with the bed outlet temperature closest to the sintering temperature was selected as the best, as well as the case with lowest flue gas temperature.

Table 3.3: Parameters used in different simulation cases

Parameters	**Set values**
Production rate [ton/h]	7-25
Length [m]	15-30
Radius [m]	0.3-0.8
Plasma length [m]	0.8-2
Plasma angle [°]	0-30
Projected surface area of particles [m^2/h]	0-55 000
Secondary gas flow [Nm^3/h]	2789-9961

4

Results & Discussion

The results from the initial scaling of process data and temperature profile are presented in the following section. The polynomial function is presented, as well as the resulting up-scaled temperature profile of the 8 MW plasma. Furthermore, a reference case was defined, based on the initial scaling, and different design parameters were varied and simulated. The resulting simulations and the trends that may be observed are discussed in this section.

4.1 Initial scaling of process data

The result from the initial scaling of process data is presented in Table 4.1 below. The scaling parameters were all based on a process producing 10 ton clinker/h, heated with an 8 MW carbon dioxide plasma.

Table 4.1: Results from initial scaling

Parameter	**Results**
Secondary gas flow [Nm^3/h]	3984
Length [m]	18
Radius [m]	0.48

4.2 Plasma temperature profiles

Based on the measurement data of the 50 kW plasma, the centre line temperature in a set number of axial positions from the generator outlet was rewritten as a percentage of the maximum temperature within the plasma. The acquired centre temperature ratios are described in equation 4.1.

$$T_{centre} = \begin{bmatrix} 1.0 & 0.96 & 0.88 & 0.83 & 0.81 & 0.74 & 0.73 & 0.719 \end{bmatrix} * T_{burner} \tag{4.1}$$

It can be seen that the temperature decreases from the plasma generator outlet down to 71.9% of the maximum temperature. Since this decline in temperature is assumed to be the same for the 8 MW plasma, the centre temperature was found, at the corresponding axial (z) positions shown in equation 4.2, initially from the experimental measurements. Assuming the calculated maximum temperature, which was found by Equation 3.5 and enthalpy tables from Heidelberg Materials Sweden, the temperature decreases to 71.9% of the maximum temperature. Equation 4.1 shows the percentages of the maximum temperature for the initial scaling of the plasma, but changes when the plasma occupies a different number of cells. The centre temperature is then assumed to always decrease from 100% of the plasma generator temperature, to 71.9% of the generator temperature, and a linear equation is then fit to the number of axial cells occupied by the plasma gas, in the heat transfer model.

$$z_{positions} = \begin{bmatrix} 0.04 & 0.14 & 0.29 & 0.43 & 0.57 & 0.71 & 0.86 & 1.00 \end{bmatrix} * L_{plasma} \tag{4.2}$$

As stated in section 3.3.1, temperature ratios comparing the decrease from the centre temperature to the edge of the plasma were calculated according to equation 3.14. This resulted in a matrix of temperature ratios shown in equation 4.3, at the corresponding axial positions shown in equation 4.2 and radial (r) positions shown in equation 4.4.

$$x_{i,j} = \begin{bmatrix} 0,00 & 0,00 & 0,00 & 0,00 & 0,00 & 0,00 & 0,00 & 0,00 \\ 0,14 & 0,20 & 0,14 & 0,11 & 0,07 & 0,02 & 0,02 & 0,03 \\ 0,73 & 0,65 & 0,46 & 0,35 & 0,27 & 0,14 & 0,12 & 0,11 \\ 1,00 & 0,97 & 0,80 & 0,65 & 0,51 & 0,34 & 0,30 & 0,28 \\ 1,00 & 1,00 & 1,00 & 0,88 & 0,76 & 0,54 & 0,49 & 0,44 \\ 1,00 & 1,00 & 1,00 & 1,00 & 0,95 & 0,77 & 0,65 & 0,60 \\ 1,00 & 1,00 & 1,00 & 1,00 & 1,00 & 0,93 & 0,80 & 0,75 \\ 1,00 & 1,00 & 1,00 & 1,00 & 1,00 & 1,00 & 0,93 & 0,88 \\ 1,00 & 1,00 & 1,00 & 1,00 & 1,00 & 1,00 & 1,00 & 0,96 \end{bmatrix} \tag{4.3}$$

$$r_{positions} = \begin{bmatrix} 0 \\ 0.125 \\ 0.25 \\ 0.375 \\ 0.5 \\ 0.625 \\ 0.75 \\ 0.875 \\ 1 \end{bmatrix} * R_{plasma} \tag{4.4}$$

4.2.1 Polynomial function

To make the temperature distribution described above more generalised, and to allow for variations in the radius and length of the heated plasma gas, the temperature ratios were written as a polynomial function of the radial and axial positions. This resulted in a fifth degree, two dimensional, polynomial, see equation 4.5.

$$\begin{gathered} x(r,z) = -0.059 + 0.092r + 0.589z + 18.93r^2 - 2.949rz - 1.296z^2 - \\ 26.4r^3 - 26.82r^2z + 7.689rz^2 + 0.7797z^3 - 6.345r^4 + 66.18r^2z - \\ 6.089r^2z^2 - 5.129rz^3 - 0.6784r^5 + 8.563r^4z - 44.05r^3z^2 + 17.93r^2z^3 \end{gathered} \tag{4.5}$$

The temperature ratios in each computational cell, given by the polynomial function, were then used to calculate the initial temperature profile of the 8 MW plasma, giving a temperature profile, in Kelvin. Since the maximum plasma gas temperature is based on calculations for an ideal case, the peak temperature is a theoretical maximum. Due to heat losses and other operating conditions, the actual temperatures in the plasma may be lower.

Since the calculations are based on measurements performed on the 50 kW plasma, there were fewer data points available for the axial positions closest to the plasma generator. Thus the temperature calculations for the positions closest to the plasma generator may lack in accuracy, compared to further out in the plasma, where more measurement points were available. The measurement data was only available for half of the plasma, and the plasma is assumed to be radially symmetrical around it's horizontal centre axis, which is a simplification. It is also difficult to know the accuracy of these results, since it comes from direct scaling of a smaller plasma torch, therefore it would be needed to validate these results with experiments using a larger plasma. However, performing temperature measurements at such extreme temperatures is very challenging, therefore there are many uncertainties in the accuracy of the measurements.

4.3 Coal case

The results from simulating the present coal flame rotary kiln at Heidelberg Materials Sweden, Kiln 8, are presented in this section. A previous version of the modelling tool was used for this case, therefore the changes described in Chapter 3 were not implemented for this particular model.

In Figure 4.1 below, the resulting axial temperature profile of a vertical cross-section of the the coal flame and gas within the rotary kiln is presented, where the bed would be located at the bottom of the figure if included. It is seen that the length of the flame is approximately 50 m, hence occupying 62.5% of the total kiln length. As can be seen in the figure below, the maximum temperature of the flame is approximately 2300K, at the position close to the burner.

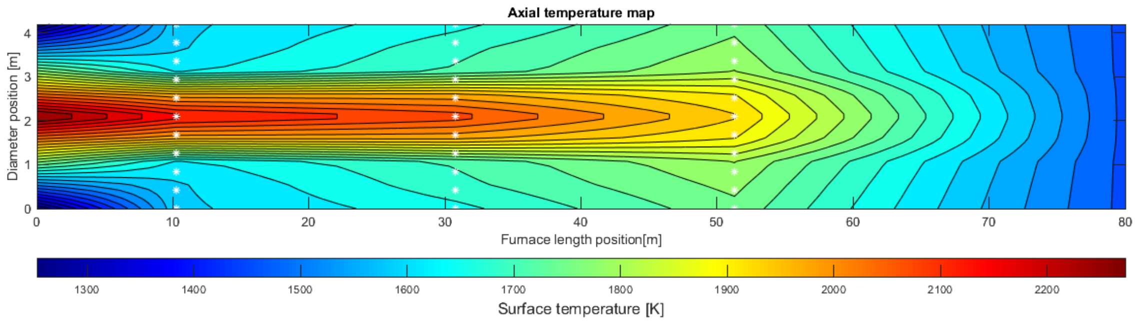

Figure 4.1: Axial temperature map of a vertical cross-section of the coal flame and gas within the present rotary kiln at Heidelberg Materials Sweden

Moreover, Figure 4.2 presents a three dimensional temperature map of the kiln walls as well as the bed material, where the bed is represented by the lowered section to the right. The axis named “Length position” refers to the axial positions, whereas the burner as well as the bed outlet are situated at position 0 m, while the flue gas outlet and bed inlet are located at position 80 m. The “Angular position” axis denotes the angular positions of the cylindrical kiln. In order to simplify the visualisation of the temperature profile of the walls and bed material, the inside of the kiln walls has been “unfolded”.

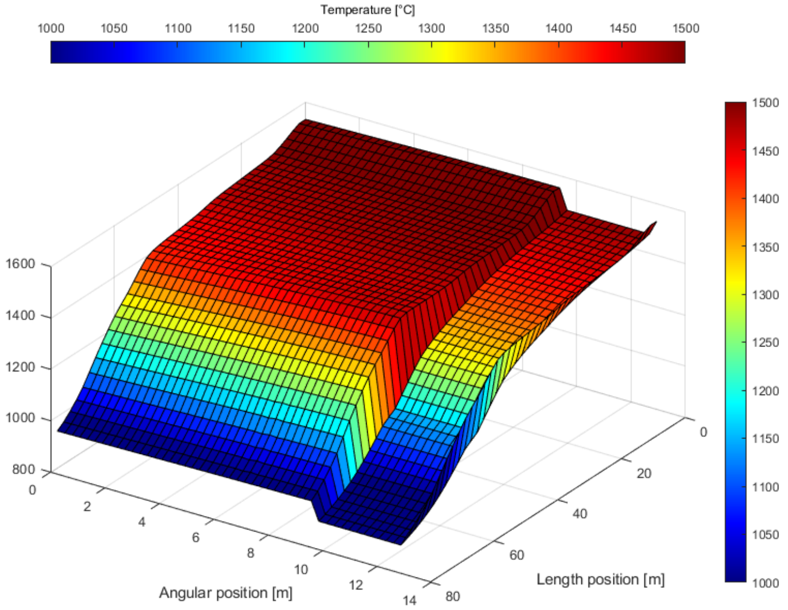

Figure 4.2: A three dimensional temperature map of the kiln walls and bed material within the present rotary kiln at Heidelberg Materials Sweden.

The grid resolution used in this simulation was 40 cells in the axial direction, 20 in the radial, 48 in the angular and a number of S_6 discrete ordinates approximation was used.

In Table 4.2 the heat balance of Kiln 8 is presented, it is seen that the major heat transfer mechanisms to the bed are radiation and conduction. Radiation accounts for 40% of the total heat demand, whereas the conduction accounts for 35%. Moreover, the heat transfer from convection accounts for 3.9% of the total heat demand. Considering that the rotary kiln produces 230 ton clinker/h, and the total heat to bed is 51.72 MW, the heat to clinker yield is 0.22 MWh/ton clinker for Kiln 8.

Table 4.2: Heat balance results for the coal case

Parameter [MW]	Results
Radiation to bed	26.17
Convection to bed	2.57
Conduction to bed	22.98
Total heat to bed	51.72
Outer heat losses	1.78
Total heat to gas	12.01
Total heat demand	65.51

Further results from the coal flame simulation is presented in Table 4.3 below. The outlet temperature of the bed material is 1485°C, this is also the peak temperature the bed reaches, and is represented by the bed temperature at length position 0 in Figure 4.2. The residence time for the bed material is 72.8 minutes. The Reynolds number for the gas flow within the kiln is approximately 322 000, therefore it can be concluded that the flow is turbulent.

Table 4.3: Simulation results for the coal case

Parameter	Results
Bed outlet temperature [°C]	1485
Residence time [min]	72.8
Reynolds number	322 000

4.4 Reference case

The results from the initial scaling presented in section 3.5.2 were used as the reference case settings. The results from the simulation with these reference case settings are presented in Table 4.4 below. The flue gas temperature, which is the gas leaving the rotary kiln and entering the calciner as seen in Figure 3.1, is found to be 2181°C. This temperature is very high since the present rotary kiln at Heidelberg Materials Sweden, Slite, usually attains a flue gas temperature between 900-1200°C, therefore it seems that the heat transfer is inefficient, and that the flue gas holds heat that could be utilised. The maximum bed temperature is 1412°C, and therefore a bit lower than the desired temperature of 1450°C needed for the sintering to fully occur. Moreover, the outlet temperature of the bed material is 1320°C which also implies that the bed has already started cooling at the end of the kiln, which is undesired due to the backwards reactions of the clinkerisation that might occur. In the table it can be seen that the Reynolds number is 122 000, and therefore concluded that the gas flow in the demonstration kiln is turbulent, which in turn makes the results of the scaling more reliable since the gas flow in Kiln 8 also is turbulent, as seen in previous section.

Table 4.4: Simulation results for the reference case

Parameter	Results
Flue gas temperature [°C]	2181
Maximum bed temperature [°C]	1412
Bed outlet temperature [°C]	1320
Reynolds number	122 000
Residence time [min]	19.4

As can be seen in Table 4.4, the Reynolds number in the reference case kiln corresponds to approximately 40% of the Reynolds number of the full scale kiln. The reason for this is likely that the reference case kiln has a smaller diameter. A lower Reynolds number indicates a less turbulent flow, which affects the convective heat transfer thus causing a lower contribution of heat transfer from the gas to the bed via convection.

In Figure 4.3 below, an axial temperature map of a vertical cross-section of the plasma and gas is presented, where the bed would be located at the bottom of the figure if included. It can be seen that the plasma has a conical shape, and that it expands towards the wall further into the kiln as the secondary gas is continuously mixed with the plasma.

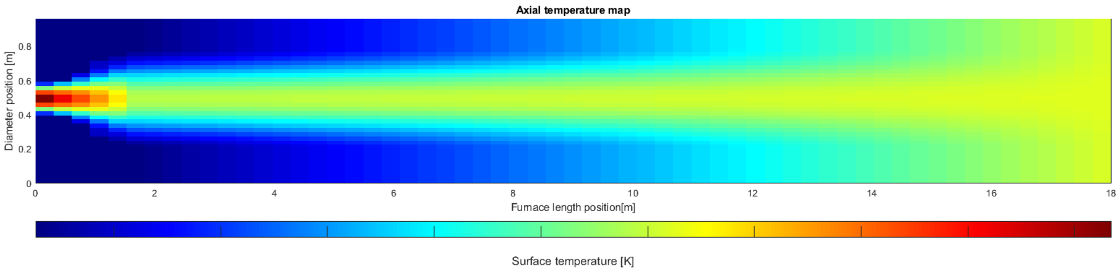

Figure 4.3: Axial temperature map of the plasma and gas within the reference case rotary kiln

Figure 4.4 below presents a three dimensional temperature map of the kiln wall and the bed, where the right end of the map represents the bed material in the kiln. These results come from the modelling tool, where the temperatures of the kiln wall, bed material and flue gas come from iterating and updating the energy balance until convergence.

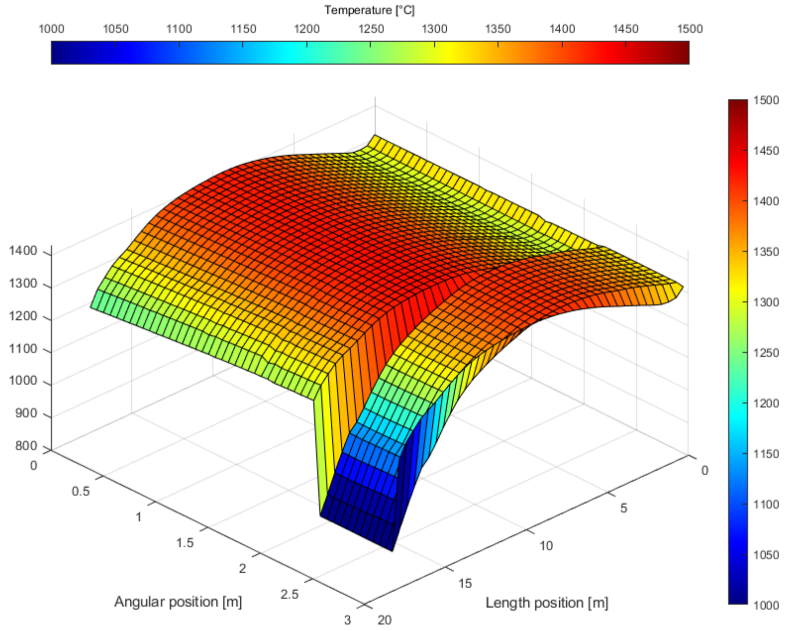

Figure 4.4: A three dimensional temperature map of the kiln walls and bed within the reference case rotary kiln

As for the coal case, the grid resolution in the reference case was set for 40 cells in the axial direction, 20 cells in the radial direction, and 48 cells in the angular direction, with an S_6 approximation for the discrete ordinates.

The heat balance results from the reference case simulation are presented in Table 4.5 below. The total heat demand is 7.17 MW, which corresponds to 11% of the total heat demand of Kiln 8. The most protruding results is the total heat to gas which is 5.56 MW, which is high, indicating that the heat transfer is inefficient. The table also shows that both the radiative, convective, and conductive heat transfer contributions to the bed are quite low. The contribution from radiation heating the bed material is 10% in the reference case, whereas the contribution from convection is 4.6%, which is in the same range as Kiln 8 seen in previous section. Lastly, the conduction to bed contributes with 7.5% in this case.

Table 4.5: Heat balance results for the reference case

Parameter [MW]	**Results**
Radiation to bed	0.66
Convection to bed	0.35
Conduction to bed	0.49
Total heat to bed	1.49
Outer heat losses	0.11
Total heat to gas	5.56
Total heat demand	7.17

The total heat to bed is 1.49 MW, and since the bed needs more heat in order to reach 1450°C, it can be concluded that this value also need to increase for a more efficient heat transfer. The heat to clinker yield is in this case 0.15 MWh/ton clinker.

4.5 Different parameters in cases

A few different geometrical and operational design parameters were changed to investigate how each parameter influences the heat transfer, and the sensitivity of the process. For each case, only one parameter is changed and the other parameters are kept constant as for the reference case, see Table 3.2. The results from the simulations are presented in the sections below, and a discussion on how the heat transfer is affected follows. Three dimensional temperature maps and axial temperature maps for all cases simulated, as well as bed and flue gas temperatures, residence times and heat balances can be found in Appendix A.

4.5.1 Kiln length

The results from investigating different kiln lengths are presented in Figures 4.5 and 4.6 below. It is seen in Figure 4.5 that an increase in kiln length results in somewhat increased bed temperatures, this is likely due to the residence time increasing with a longer kiln, as also seen in the figure, where the green dotted line represents the varying residence time. A kiln length of 12 m resulted in a residence time of 13.4 minutes, whereas a kiln length of 30 m and same radius resulted in 32.3 minutes. Hence, an increased length provides more time for the bed to absorb heat from the plasma and secondary gas. However, the bed temperature increase is not sufficient enough to reach the sintering temperature, in that case the kiln would have to be much longer which then would not account for as a demonstration size anymore. Moreover, it can be seen in the figure that the blue curve, representing the maximum temperature of the bed, have some plateaus during different lengths of the kiln. This is most probably due to the varying resolution of the model during the different simulations. For example, it was required to increase the number of axial cells for longer kilns, which in turn has an effect on the output from the model, hence slightly different from cases where resolution remained consistent.

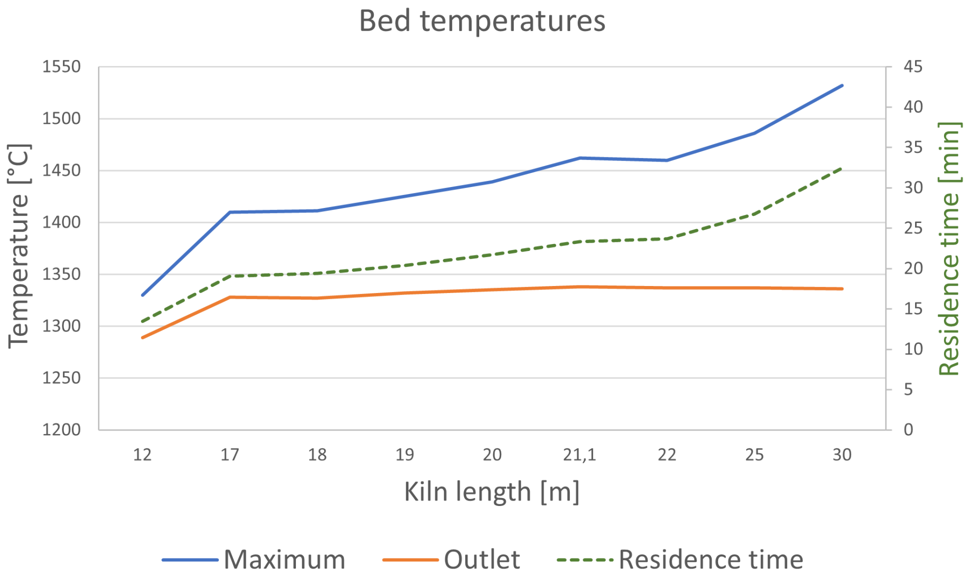

Figure 4.5: Temperature of the bed material for different kiln lengths

Furthermore, the flue gas temperature is hardly affected by the kiln length, as is seen in Figure 4.6 where the curve is quite constant and flat, with values within the interval of 2225 to 2150°C, this indicates that the overall gas convection is somewhat constant and independent on the length.

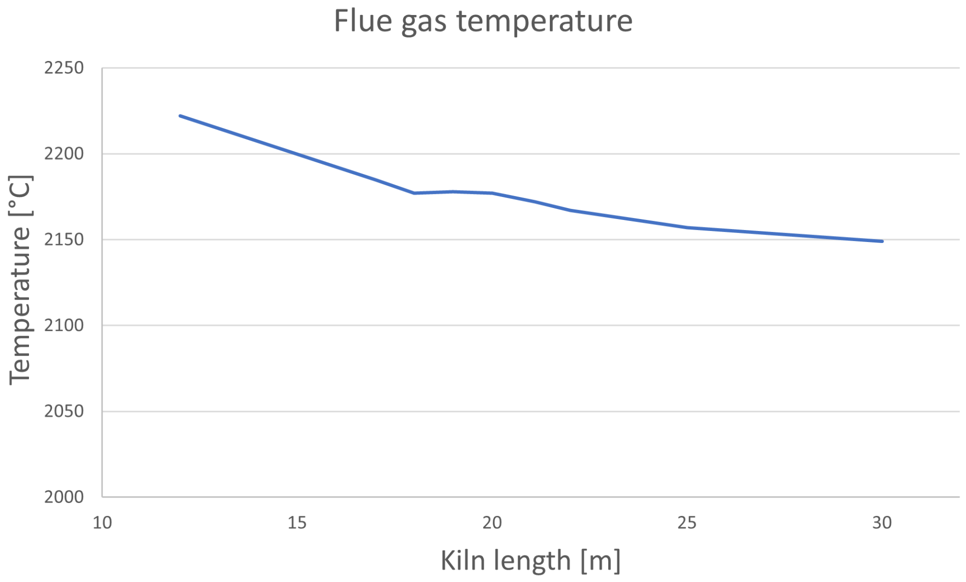

Figure 4.6: Flue gas temperatures for different kiln lengths

4.5.2 Kiln radius

Increasing the kiln radius results in increased bed temperatures, see Figure 4.7, again the reason for this is presumably due to the residence time being increased. With a radius of 0.3 m, the residence time for the bed material was just 8.55 minutes, compared to a kiln with a radius of 0.8 m the resulting residence time was as long as 53.6 minutes. It can be noted that the maximum bed temperature steadily increases, while the bed's outlet temperature seems to stabilise around a radius of 0.5 m. The convective heat transfer decreases with an increasing radius, likely due to reduced gas velocities, which could be a reason as to why the outlet temperature of the bed doesn't increase further.

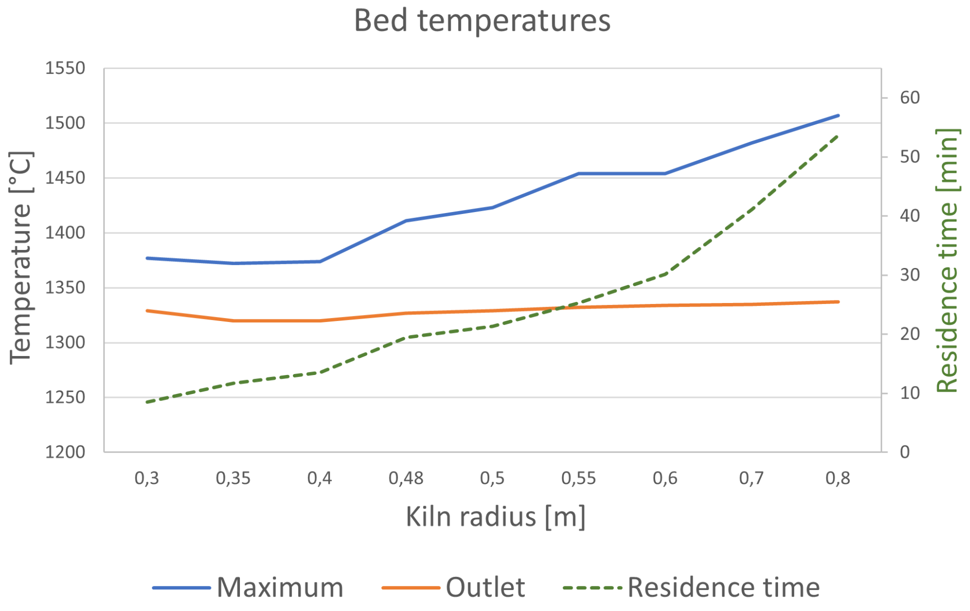

Figure 4.7: Temperature of the bed material for different kiln radii

Another potential reason for the bed's peak temperature increasing is the correlation between an increased radius resulting in an increased heat transfer area between the bed material and the passing gas. This results in more heat being transferred to the bed through radiation, and subsequently increasing the temperature. Moreover, the flue gas temperature doesn't seem to follow a trend, as seen in Figure 4.8, it decreases with increasing radius up to 0.5 m, but then increases. Although the flue gas temperature varies, the variation is of such a low magnitude that it can be seen as constant and thus not dependent on the radius.

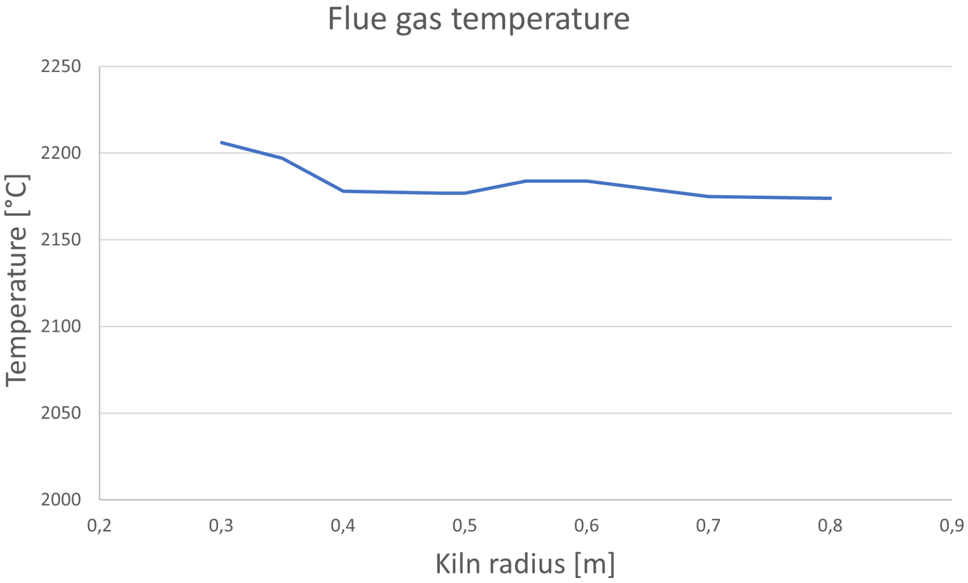

Figure 4.8: Temperature of the flue gas for different kiln radii

For both increased kiln length and kiln radius it can be noted that the bed outlet temperature remain constant. This is most probably due to insufficient mixing of gas in this the area close to the plasma generator, and that the majority of the gas there is the secondary gas which holds a temperature of 980°C in this position. This causes the bed to be cooled very efficiently at the bed outlet, and the bed temperatures to remain constant.

4.5.3 Production rate

Varying the production rate of bed material affects both the flue gas and bed temperatures substantially, as presented in Figures 4.9 and 4.10. Increasing the mass flow of the bed material results in a decrease of both the bed and flue gas temperatures. A lower flue gas temperature is desirable, since this means that more heat has been transferred from the gas to the bed.

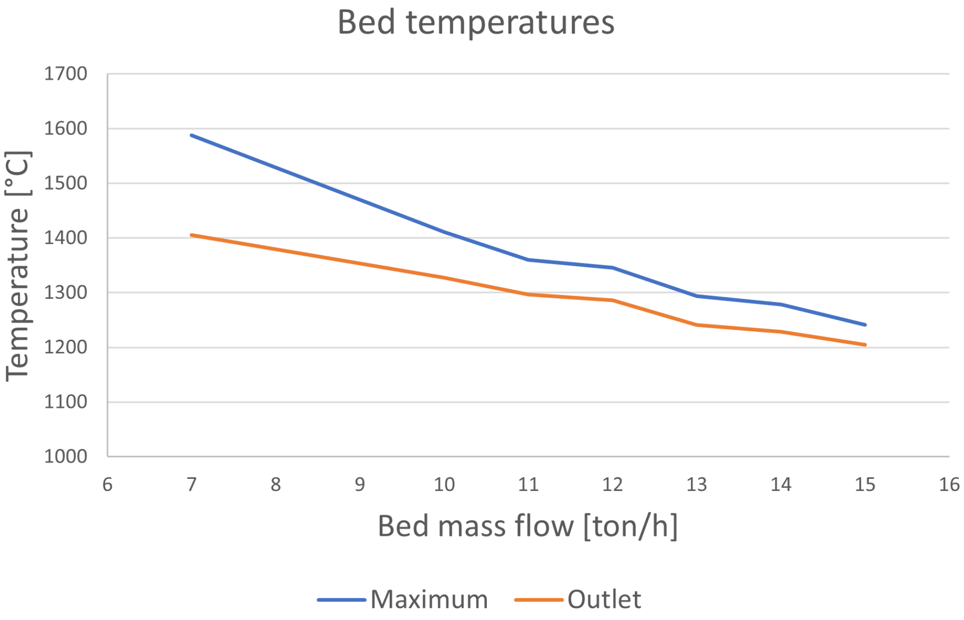

Figure 4.9: Temperature of the bed material for different bed mass flows

Increasing the bed mass flow decreases the flue gas temperature, but the bed will also require more heat due to more material being present in the kiln. Thus, more heat from the gas is utilised which decreases the flue gas temperature, but the heat transfer is still not sufficient for reaching the sintering temperature, this is also seen in Figure 4.9. When increasing the bed mass flow, the residence time drastically decreases, comparing the reference case with a production rate of 10 ton/h to a case producing 15 ton/h, the residence time is reduced from 19 minutes to 13 minutes. As previously discussed, a short residence will not give the material enough time to reach higher temperatures.

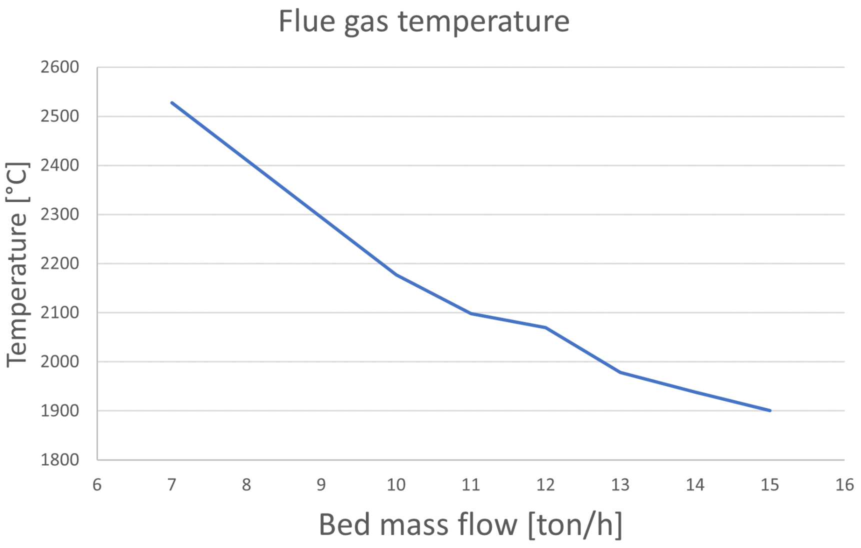

Figure 4.10: Temperature of the flue gas for different bed mass flows

A lower bed material flow increases the bed temperatures as well as the flue gas temperature, as also seen in Figures 4.9 and 4.10, this is probably due to the fact that less heat is required to heat up the bed due to less material being present. However, since the flue gas temperature also increases one can conclude that more heat is still present and available for the process.

4.5.4 Particle content in suspension

In Figure 4.11 the result of the bed material temperatures when altering the particle content being in suspension in the kiln is presented. As predicted, an increase of particle content in the plasma increases the radiative heat transfer from the plasma gas to the bed material, due to the particles being broad-band emitters, unlike the gas which only emits within certain intervals on the spectrum. Therefore, the bed material receives more heat and can now reach the sintering temperature due to the radiation from particles. It can also be seen that the maximum temperature almost reaches the outlet bed temperature with higher particle content, which is desired since the maximum temperature also should be the outlet temperature so that cooling can start immediately after the rotary kiln to avoid backward reactions of the clinker. The unit of the suspended particles is m^2/h, which is the projected surface area of the particles added to the plasma generator. This unit is used since the projected surface area is what radiates. A coal flame would have a corresponding value of approximately 150 000 m^2/h.

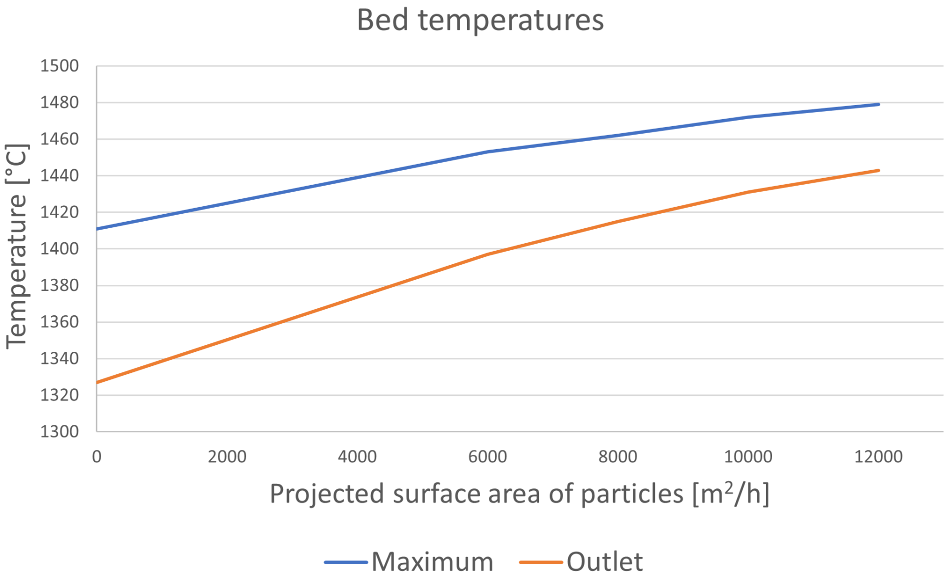

Figure 4.11: Temperature of the bed material for different amounts of particle content.

Furthermore, Figure 4.12 below presents the results of the flue gas temperature with varying particle content. It can be seen that the flue gas temperature decreases when increasing the particle content.

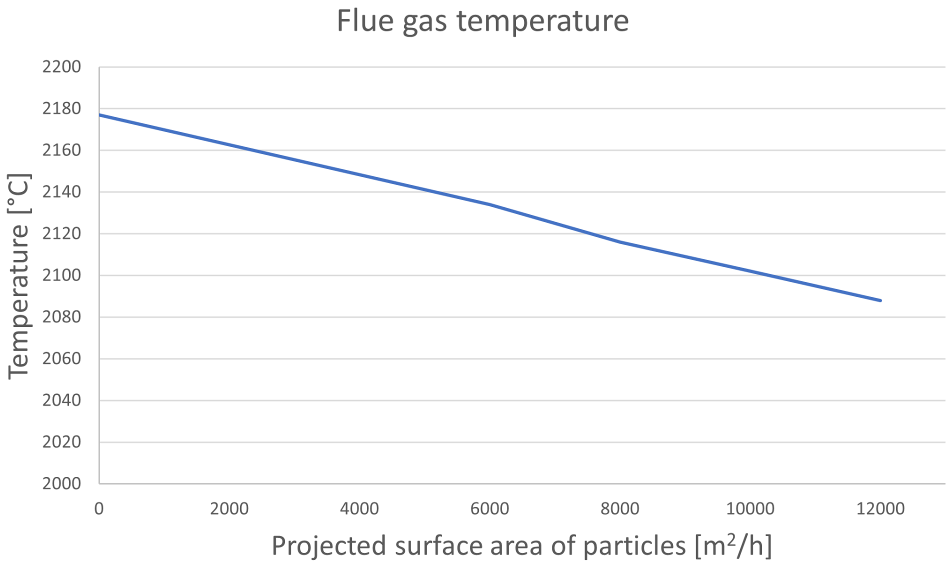

Figure 4.12: Temperature of the flue gas for different amounts of particle content

In Figure 4.13 below, the heat transfer contributions from convection and radiation to the bed are presented. Here it can be seen that the convection decreases, whereas the radiation is increased with varying particle content. A possible reason for the decrease in flue gas temperature could be that the convection from the gas has increased, but in Figure 4.13 it can be seen that the convection to the bed material decreases with an increased amount of particles. Thus the more likely reason for the decrease in flue gas temperature is that heat is transferred from the gas to the particles, cooling the gas. The particles then radiate heat to the bed, thus increasing the radiative heat transfer. Since the bed and wall and bed temperatures increase from the increased radiation, the temperature difference between the gas and bed has decreased, which decreases the convective heat transfer.

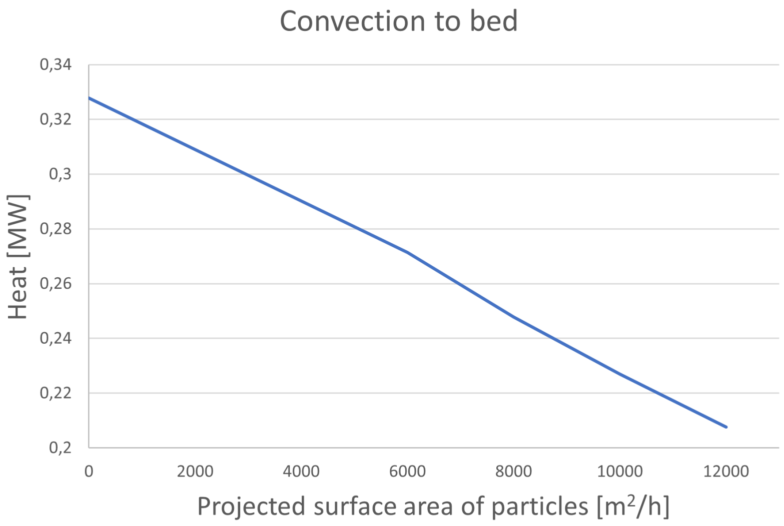

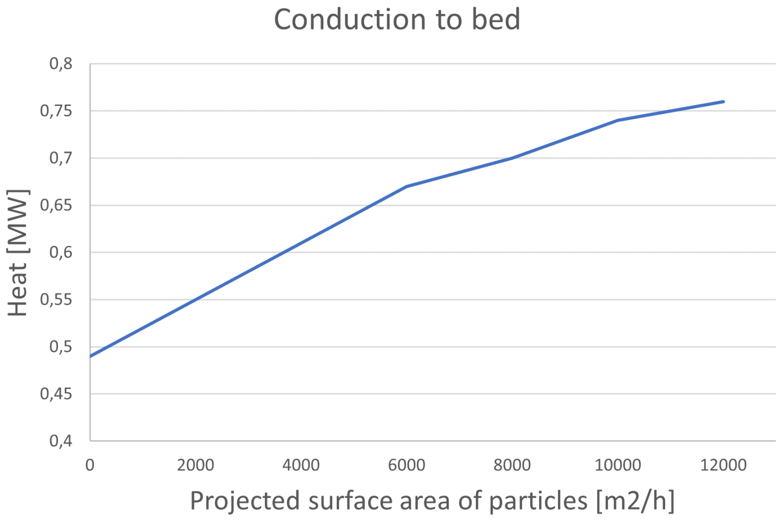

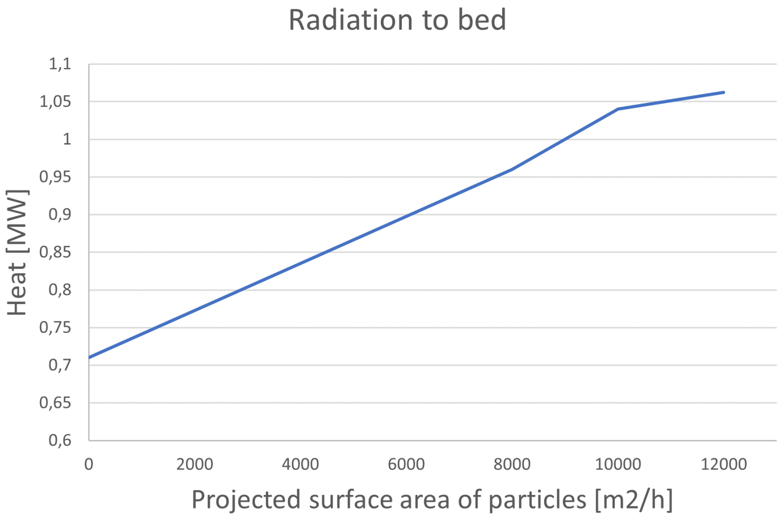

Figure 4.13: Heat transfer to the bed for different projected surface area of particles, convection presented on the top, conduction in the middle, and radiation on the bottom

4.5.5 Plasma length

The results from altering the plasma gas length while keeping the same plasma radius are presented in Figures 4.14 and 4.15 below. Figure 4.14 presents the impact on bed temperatures, and it can be seen that a shorter plasma length results in increased bed temperatures. This is probably due to the plasma and gas temperature profile being dispersed towards the wall earlier (on a shorter axial distance) with shorter plasmas, and therefore more heat is transferred earlier to the bed than with a longer plasma. Moreover, Figure 4.14 also shows that the peak temperature and the outlet temperature of the bed follows a similar pattern for a varying plasma length. However, the large gap between the maximum and outlet temperature implies that the bed is starting to cool down before reaching the kiln outlet.

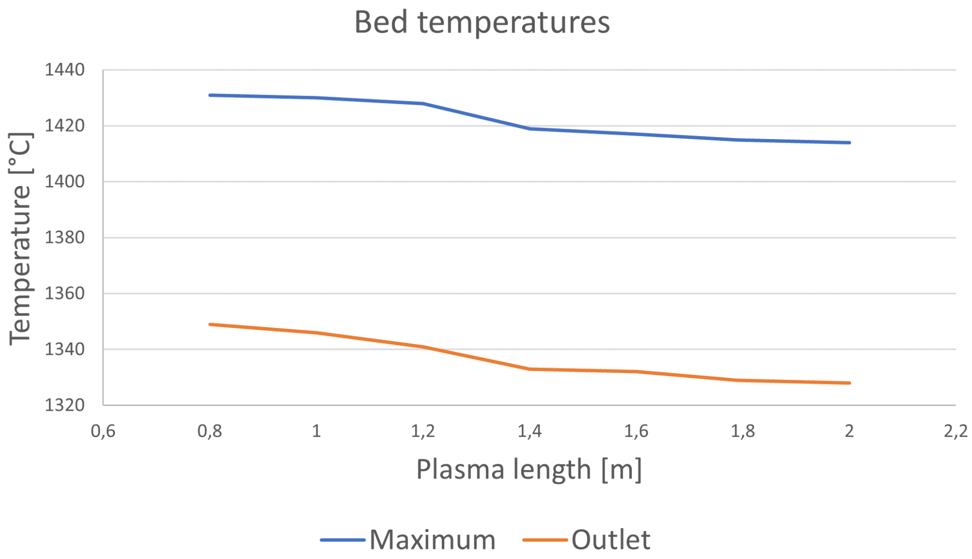

Figure 4.14: Temperature of the bed material for different plasma lengths

Figure 4.15 presents the impact on the flue gas temperature. The flue gas temperature decreases slightly with increased plasma length, but it is still seemingly constant around an interval of 2180 and 2190°C.

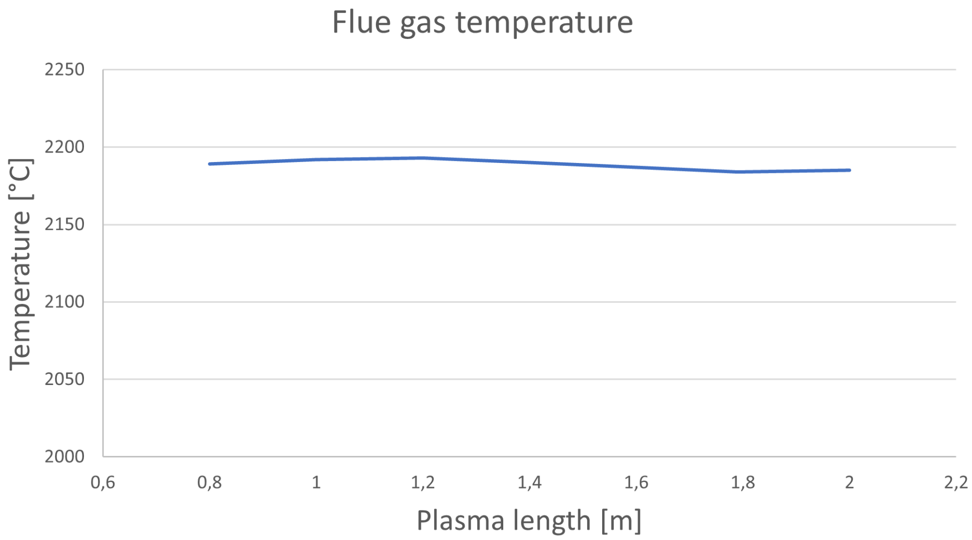

Figure 4.15: Temperature of the flue gas for different plasma lengths

A possible reason for this trend is again that the shorter plasma expands towards the kiln wall earlier in the kiln compared to a longer plasma. This is also confirmed when comparing the temperature profile of a plasma length of 0.8 m presented in Figure 4.16 below with the temperature profile of the reference case in Figure 4.3. By studying the gradient towards the walls throughout the kiln, it can be seen in Figure 4.16 that the plasma expands towards the wall earlier than for the reference case plasma. Consequently, more heat is transferred from the gas and thus the convection is somewhat increased for shorter plasmas. However, the resulting temperatures of both the bed and flue gas are only slightly affected, therefore one can conclude that this parameter is not of importance.

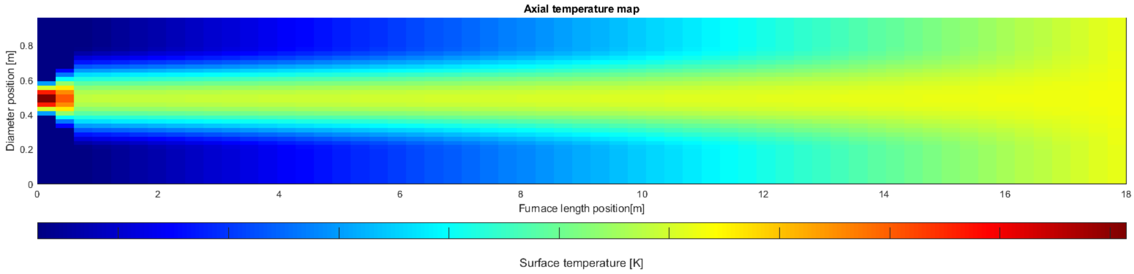

Figure 4.16: Axial temperature map of the gas and the plasma within the kiln, with a plasma length of 0.8 m

It can also be noted that the plasma only covers about 10% of the kiln length, compared to the coal flame which occupies up to 62.5% of the total kiln length.

4.5.6 Tilted plasma

Next, the results from tilting the plasma towards the bed will be presented. In Figure 4.17 below, an axial temperature map profile of the gas and plasma is presented, when the plasma has been tilted with 5°. It is seen that the plasma is tilted towards the bed, and further in to the kiln the plasma reaches the bed where the temperature profile finally flattens out parallel to the bed.

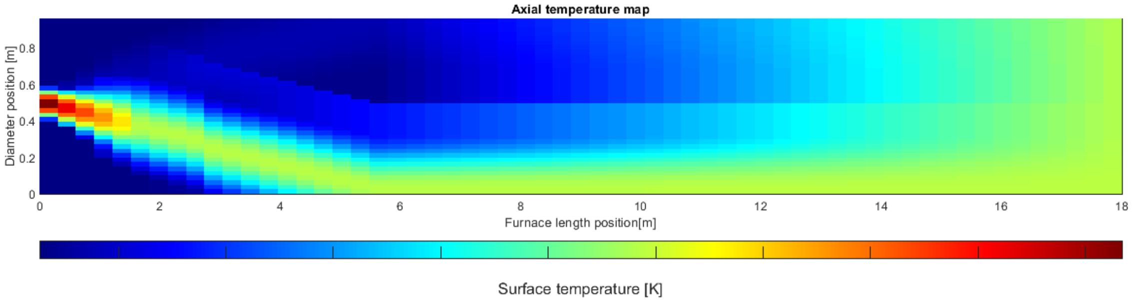

Figure 4.17: Axial temperature map of the gas and the plasma within the kiln, where the plasma is tilted by 5°

Figure 4.18 presents the temperature map of the kiln walls and bed material within the kiln. It is seen that the bed material temperature is steadily increasing throughout the kiln, one can also see that the bed is starting to cool right before the outlet, but it is however considered acceptable as it occurs in close proximity to the outlet.

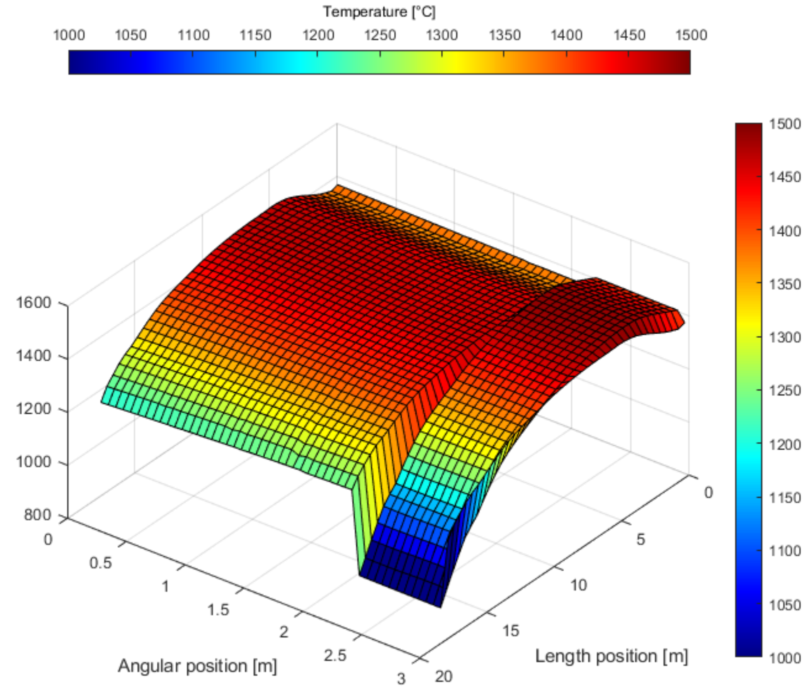

Figure 4.18: Three dimensional temperature map of the kiln walls and bed for a plasma angle of 5°

The resulting temperatures from tilting the plasma towards the bed are presented in Figures 4.19 and 4.20. It can be seen in Figure 4.19 that the bed temperatures increase when the plasma is tilted towards the bed. By tilting the plasma the heat provided by it will be more fixed towards the positions where the bed is located, and therefore where the heat is needed, which makes of a more efficient heat transfer. When the tilting angle exceeds approximately 25° one can see that the increase of the bed temperatures has reduced, so further tilting is not necessary after this point. It is also seen that the temperatures has exceeded the sintering temperature with 50°C at 6° incline, which again implies that further tilting is unnecessary.

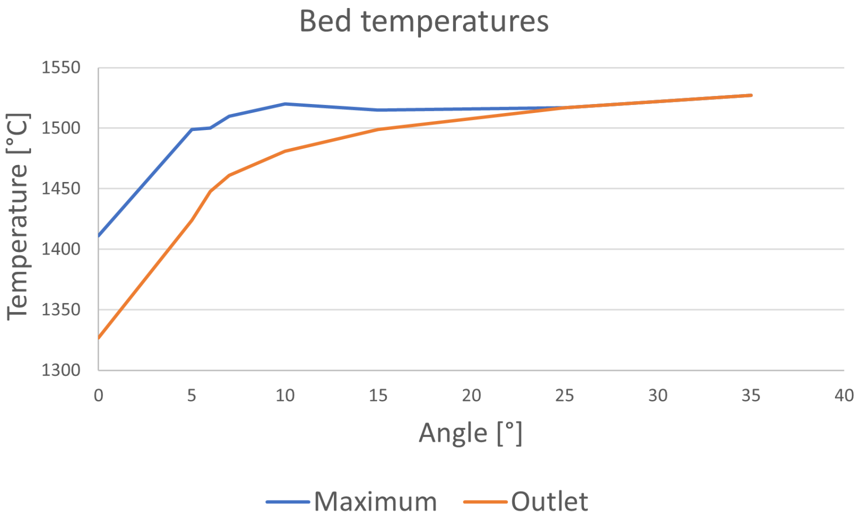

Figure 4.19: Temperature of the bed material for different plasma angles

In Figure 4.20 it is seen that the flue gas temperature decreases with a tilted plasma. The flue gas temperature is becoming constant after approximately 25°, as also seen for the bed temperatures in the previous figure, this implies that no further tilting is necessary after this point. Besides, the bed material has already exceeded the sintering temperature at approximately 6° when producing 10 ton clinker/h, as previously mentioned. If the production rate of clinker instead would be increased, further tilting could be done as to utilise more heat from the flue gas.

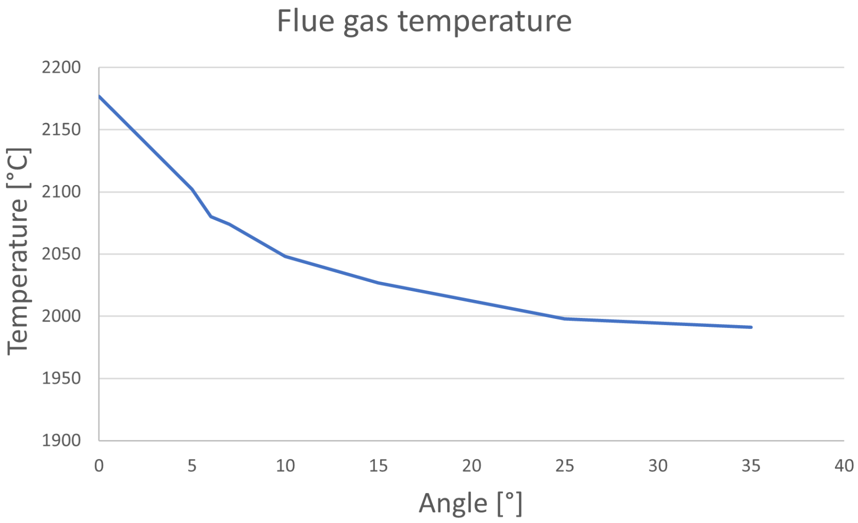

Figure 4.20: Temperature of the flue gas for different plasma angles

By tilting the plasma with 5° the flue gas temperature decreased to 2102°C, the maximum bed temperature increased to 1499°C, the outlet bed temperature increased to 1424°C, and the convection to bed increased to 0.72 MW, compared to the non-tilted plasma in the reference case. Therefore, one can conclude that tilting the plasma has a drastic effect on the temperatures within the kiln, and is a promising way of enhancing the heat transfer to the bed. Tilting the plasma further continues the decrease of the flue gas temperature and increase of bed temperatures, which implies that the convective heat transfer is increased, this is further confirmed by Figure 4.21 below. It is also seen in this figure that the convection reaches a maximum, once again at 25°, when operating the kiln with 10 ton clinker/h. The curve also begin to flatten out after a 6° angle, which indicates that this is the optimal plasma gas angle for this production rate of clinker. It was proven possible to reach the desired bed outlet temperature of 1450 °C by tilting the plasma, but with a resulting flue gas temperature of around 2000°C.

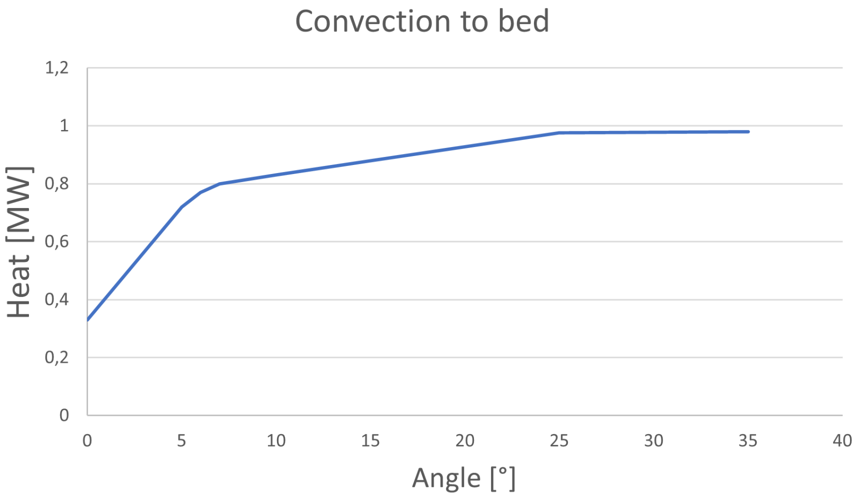

Figure 4.21: Heat transferred to bed via convection, for different plasma angles

4.6 Selected dimensions

The trends presented in previous section indicated which parameters to focus on during the optimisation. By tilting the flame 6°, the bed reaches the sintering temperature of 1450°C at the outlet, but the flue gas temperature is still high compared to the current process. However, if a high flue gas temperature is desired, since the flue gas enters the calciner upstream the process which requires additional heat, then this design would be a good option.

From the trends it was noted that tilting the plasma gas and increasing the particle content increased the bed temperature, while increasing the production rate of clinker resulted in decreased flue gas temperatures. In order to attain the sintering temperature of the bed, as well as a flue gas temperatures below 1200°C, as to achieve similar process temperatures as the current process at Heidelberg Materials, different combinations of these parameters were tested and optimised. The settings for the final optimised simulation is presented in Table 4.6 below. Here it is seen that the production rate of clinker was increased substantially in comparison to the reference case, it is also seen that the plasma angle as well as particle content are increased.

Table 4.6: Parameters used in the optimised demonstration scale rotary kiln

Parameters	
Production rate [ton/h]	25
Length [m]	18
Radius [m]	0.48
Plasma length [m]	1.789
Plasma angle [°]	30
Projected surface area of particles [m^2/h]	55 000
Secondary gas flow [Nm^3/h]	9961

Table 4.7 presents the simulation results of the optimised kiln. It can be seen that the sintering temperature is achieved, and the flue gas temperature is 1174°C which is within the interval of the present cement process at Heidelberg Materials Sweden, Slite, as previously seen in Figure 3.1. The Reynolds number is 125 000 which is almost the same as the reference case, and the residence time has decreased to 7.9 minutes due to the increased mass flow rate of bed material.

Table 4.7: Simulation results for the optimised kiln

Parameter	**Results**
Flue gas temperature [°C]	1174
Bed outlet temperature [°C]	1453
Reynolds number	125 000
Residence time [min]	7.9

The results from the optimised simulation are presented in Figures 4.22 and 4.23 below. Figure 4.22 presents the temperature map of the kiln walls and bed, and it is seen that the bed material is steadily increased throughout the kiln before reaching the sintering temperature. Additionally, the figure shows that the highest temperatures of the kiln walls occur in close proximity to the plasma generator location. This indicates that the gas temperature is quite high in this area, potentially due to increased radiation from the particles along with the high temperatures of the plasma at the generator position. Wearing and problems with stress on the refractory lining of the walls are possible risks with too high gas temperatures within the kiln.

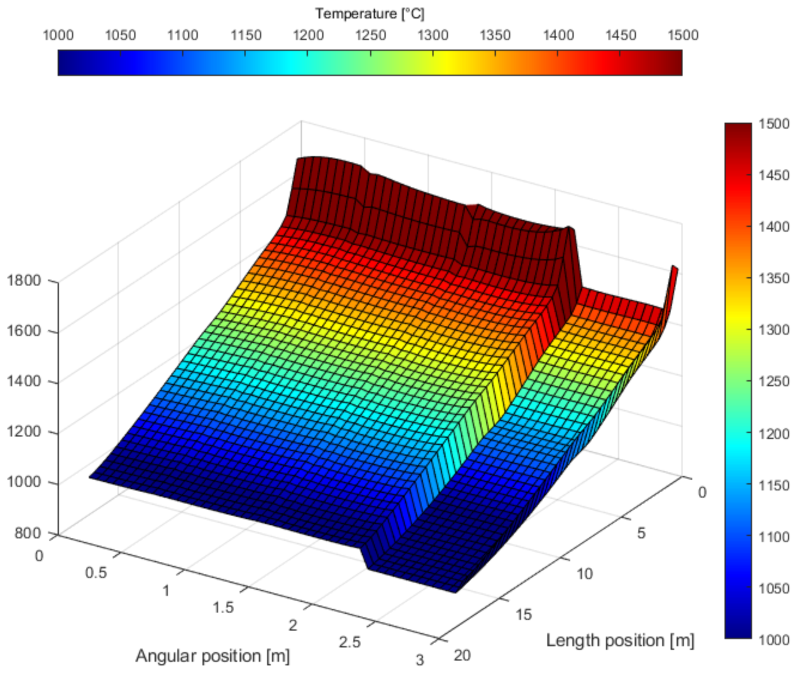

Figure 4.22: Three dimensional temperature map of the kiln walls and bed for a optimised kiln

Figure 4.23 presents the axial temperature map of the gas and the plasma, here the large tilting of the plasma can be seen, as well as the plasma reaching the bed at approximately 1.4 m. It can also be seen that a significant portion of the temperature profile is characterised by blue gradients, which suggests a notable decline in gas temperature with increasing plasma angle. This is probably due to that the heat transfer from the plasma is more directed towards the bed material, making it more efficient, hence less heat is transferred from the plasma to the secondary gas.

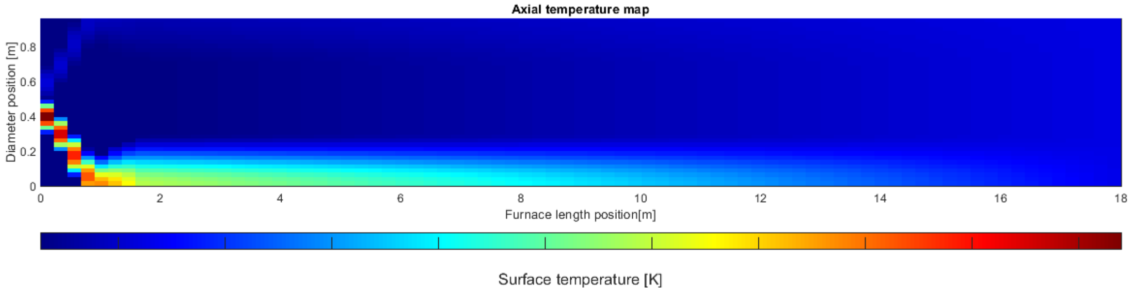

Figure 4.23: Axial temperature map of the gas and the plasma within the optimised kiln

In Table 4.8 the results from the heat balance of the optimised kiln is presented. When comparing it with the heat balance of the reference case in Table 4.5, it is noted that all heat transfer mechanisms to the bed has increased. As predicted, the heat transfer contribution from radiation has increased due to the addition of particle content. The increase of the convection to bed is potentially due to the tilting of the plasma. The conduction to bed probably increases due to the combination of a tilted plasma and particle content, where this results in higher kiln wall temperatures, as seen previously in Figure 4.22, which in turn grants the conduction from the walls to the bed. Moreover, heat to gas has decreased considerably compared to the reference case, this is also likely due to a more efficient heat transfer due to the tilting of the plasma.

Table 4.8: Heat balance results for the optimised kiln

Parameter [MW]	**Results**
Radiation to bed	3.12
Convection to bed	1.11
Conduction to bed	1.16
Total heat to bed	5.39
Outer heat losses	0.10
Total heat to gas	1.67
Total heat demand	7.17

A comparison of the heat to bed material in Kiln 8 and the optimised kiln is presented in Table 4.9 below. It is seen that the contribution from radiation is higher in the optimised kiln than for Kiln 8 per ton clinker, moreover, the convection to the bed is also higher when compared to Kiln 8. Furthermore, the conduction to bed is half the amount than for Kiln 8. The resulting heat to clinker yield for the optimised kiln is 0.216 MWh/ton clinker, and therefore very similar to the yield of Kiln 8 which is 0.224 MWh/ton clinker, even though each heat transfer mechanism contributes differently in both kilns.

Table 4.9: Comparison of heat to clinker for Kiln 8 and the optimised kiln

Heat to bed [MWh/ton]	**Kiln 8**	**Optimised kiln**
Radiation	0.114	0.125
Convection	0.011	0.044
Conduction	0.099	0.046
Total heat to bed	0.224	0.216

4.7 Sensitivity analysis

A sensitivity analysis was carried out to evaluate the robustness of the plasma model, as well as to investigate the effects that different plasma temperatures have on the heat transfer. Since the calculated maximum temperature of the plasma was considered an ideal maximum, the maximum temperature was reduced to 80%. This resulted in a bed outlet temperature of 1320°C with a peak temperature of 1410 °C and a flue gas temperature of 2184 °C. Of the total heat transferred to the bed, convection stands for 24% and radiation for 43%, which are very similar values to the reference case.

The plasma generator temperature was also increased by 20%, which resulted in a bed outlet temperature of 1315°C, a peak bed temperature of 1410°C and a flue gas temperature of 2220 °C. For both cases, there was no notable increase or decrease observed in the radiation, convection, or conduction to the bed. These findings suggest that a slight modification in the maximum plasma temperature will not have a significant impact of the heat transfer conditions in the kiln.

The radius of the plasma gas was determined during the initial scaling process, and was considered a constant parameter throughout the simulations. To explore the sensitivity of this initial calculation, a sensitivity analysis was conducted by varying the plasma gas radius. Similarly to the maximum temperature, the radius was reduced to 80% of the initially calculated values, as well as increased to 120% of the initial radius. Figure 4.24 shows two axial temperature maps of a vertical cross-section of the plasma and gas in the kiln, for smaller and larger plasma radius. Neither change in radius caused any significant effect on the bed or flue gas temperatures. The maximum temperature of the bed, as well as the temperature of the bed at the bed outlet, remained similar to the values of the reference case. These findings indicate that the radius of the plasma gas does not significantly influence the heat transfer to the bed.

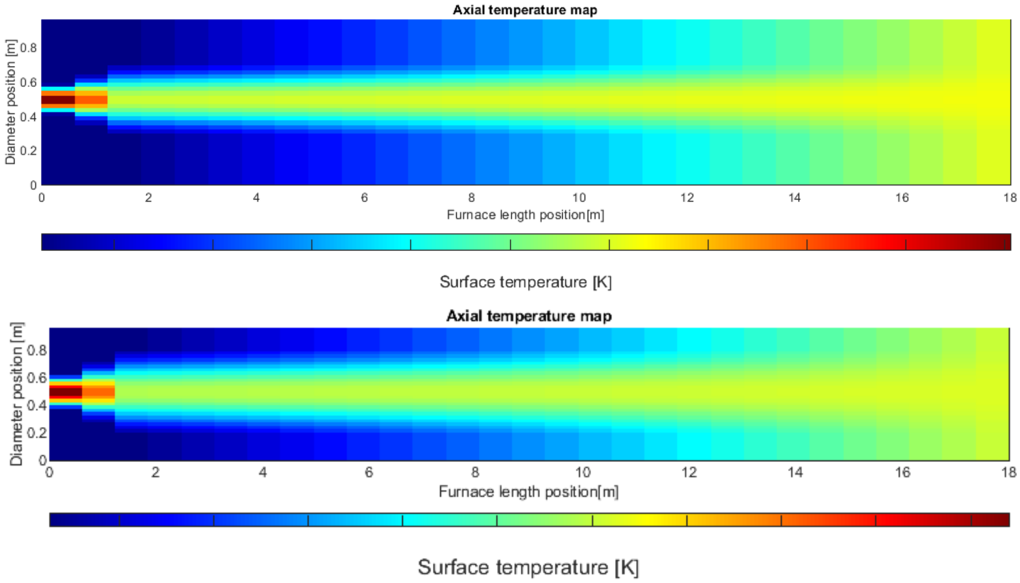

Figure 4.24: Axial temperature maps of the gas and plasma within the kiln. At the top: plasma gas with the radius increased by 20%, on the bottom: plasma gas with the radius decreased by 20%

5

Conclusion

The findings of the study implies that it is theoretically viable to design a demonstration scale rotary kiln providing sufficient heat for sintering, operated with a thermal plasma with carbon dioxide as the working gas. Several dimensions are possible for this rotary kiln, since no specific length or radius were found to be the optimal choice. In fact, neither the length nor radius significantly influenced the heat transfer within the rotary kiln at this scale. Rather, the most important parameters for increasing the heat transfer to the bed material were the addition of particle content as well as tilting of the plasma. Due to the soot and fuel particles in the coal flame, as used in the present kiln, it radiates more heat than the CO_2 plasma does, and therefore the addition of particles is crucial when operating with a plasma. Moreover, tilting the plasma towards the bed is also discovered to be essential for promoting heat transfer within the kiln. This is likely due to the heat from the plasma being more fixed towards the bed where the heat is needed, making the heat transfer more efficient.

A high flue gas temperatures indicate a large heat loss and a somewhat inefficient heat transfer process. To mitigate this issue and reduce the flue gas temperature further, a feasible strategy could be to increase the production rate of clinker, in combination with tilting the plasma and adding particles. Tilting the plasma and adding particles increases the heat transfer to the bed, while increasing the production rate decreases the flue gas temperature. When combining these parameters, it was found that the heat transfer to the bed material was equally efficient as Kiln 8 at Heidelberg Materials, Slite.

Based on the findings of this study, it can be deduced that multiple variables come into play when determining the optimal operational and geometrical parameters for a rotary kiln operating using a thermal plasma. Without the inclusion of particles, tilting the plasma was deemed necessary for the bed temperature to reach the required 1450 °C at its outlet, at the cost of higher flue gas temperatures. The inclusion of particles, as well as increasing the mass flow of bed material, play a crucial role in reducing the temperature of the flue gas. Hence, a combination of these factors is essential for determining the optimal dimension.

6

Further research

To validate the acquired temperature profile, measurements should be conducted on plasma equipment. Specifically, temperature measurements on a larger scale plasma, preferably utilising an 8 MW plasma burner, should be performed to validate the calculated temperature profile within the plasma gas. Additionally, conducting experiments involving the tilting of the plasma is suggested to investigate how the plasma gas behaves when being tilted towards the bed, as well as how the bed material reacts to a concentrated plasma of such high temperatures.

Since the addition of particles were deemed necessary to achieve a sufficient heat transfer from the gas to the bed, the effect of different particles should be examined. Different particles have different dimensions and radiative properties, thus finding suitable particles which will aid the heat transfer while not interacting with the bed material should be explored. When using a tilted plasma, the particles should be added at the same angle. The practicalities of particles added on an angle, as well as tilting the plasma gas should be examined and tested to verify the suggested selected kiln dimensions.

Further investigation into how a carbon dioxide environment will affect the process is suggested. Increasing the carbon dioxide partial pressure could have an impact on the decomposition of limestone which is why this would be important to examine. In this study, it was assumed that there were no air leaks into the system. However, it is important to that further research be conducted to explore the feasibility and potential implications of achieving a leak-free system. Assessing possible sources of air leakages is important to ensure a carbon dioxide environment.

Moreover, how the secondary gas is heated by both the bed and walls close to the plasma generator should be examined. This is necessary as there appears to be a substantial cooling effect on the bed caused by the secondary gas at these positions in the kiln, as seen in the modelling tool. Therefore, indicating that adjustments to the temperature of the secondary gas should be considered.

Bibliography

[1] A. Gunnarsson, *Radiative Heat Transfer in Suspension-Fired Systems.* Department of Space, Earth and Environment, Chalmers University of Technology, 2019.

[2] "What is climate change?" [Online]. Available: https://www.un.org/en/climatechange/what-is-climate-change

[3] "Global ghg emissions shares by sub sector," Feb 2023. [Online]. Available: https://www.statista.com/statistics/1167298/share-ghg-emissions-by-sub-sector-sector-globally/

[4] B. Wilhelmsson, C. Kollberg, J. Larsson, J. Eriksson, and M. Eriksson, "Cemzero - a feasibility study evaluating ways to reach sustainable cement production via the use of electricity," *Vattenfall, Cementa*, 2018.

[5] "Cementa, nollvision för koldioxid 2030," [Online] https://www.cementa.se/sv/nollvision2030, accessed: 2023-01-20.

[6] M. Schneider, "The cement industry on the way to a low-carbon future," *Cement and Concrete Research*, vol. 124, p. 105792, 2019. [Online]. Available: https://www.sciencedirect.com/science/article/pii/S0008884619301632

[7] T. Burman and J. Engvall, "Evaluation of usage of plasma torches in cement production," 2019.

[8] J. Petersson, "Thermal plasma in a rotary kiln for cement production: An investigation of the heat transfer mechanisms," 2022.

[9] S. Samal, "Thermal plasma technology: The prospective future in material processing," *Journal of Cleaner Production*, vol. 142, pp. 3131–3150, 2017. [Online]. Available: https://www.sciencedirect.com/science/article/pii/S0959652616317851

[10] A. Gunnarsson, K. Andersson, B. R. Adams, and C. Fredriksson, "Full-scale 3d-modelling of the radiative heat transfer in rotary kilns with a present bed material," *International Journal of Heat and Mass Transfer*, vol. 147, p. 118924, 2020.

[11] F. M. Lea and Mason, "Cement," *Encyclopedia Britannica*, 2022. [Online]. Available: https://www.britannica.com/technology/cement-building-material

[12] I. E. Agency. (2023) Cement. International Energy Agency. [Online]. Available: https://www.iea.org/reports/cement

[13] A. R. Nielsen, *Combustion of large solid fuels in cement rotary kilns.* DTU Chemical Engineering, 2012.

[14] A. P. Watkinson and J. Brimacombe, "Limestone calcination in a rotary kiln," *Metallurgical Transactions B*, vol. 13, pp. 369–378, 1982.

[15] B.-J. R. M. Bisulandu and F. Huchet, “Rotary kiln process: An overview of physical mechanisms, models and applications,” *Applied Thermal Engineering*, p. 119637, 2022.

[16] S. Wang, J. Lu, W. Li, J. Li, and Z. Hu, “Modeling of pulverized coal combustion in cement rotary kiln,” *Energy & Fuels*, vol. 20, no. 6, pp. 2350–2356, 2006.

[17] A. A. Boateng, *Rotary kilns: transport phenomena and transport processes.* Butterworth-Heinemann, 2015.

[18] J. Gorog, T. Adams, and J. Brimacombe, “Regenerative heat transfer in rotary kilns,” *Metallurgical transactions B*, vol. 13, pp. 153–163, 1982.

[19] P. Barr, J. Brimacombe, and A. Watkinson, “A heat-transfer model for the rotary kiln: Part ii. development of the cross-section model,” *Metallurgical and Materials Transactions B*, vol. 20, pp. 403–419, 1989.

[20] M. Boulos, P. Fauchais, and E. Pfender, *Thermal plasmas: Fundamentals and applications: Volume 1.* Plenum Press, 1994.

[21] N. Venkatramani, “Industrial plasma torches and applications,” *Current Science*, vol. 83, no. 3, pp. 254–262, 2002. [Online]. Available: http://www.jstor.org/stable/24106883

[22] P. Taylor and S. Pirzada, “Thermal plasma processing of materials: A review,” *Advanced Performance Materials*, vol. 1, pp. 35–50, 01 1994.

[23] J. Khinast, G. Krammer, C. Brunner, and G. Staudinger, “Decomposition of limestone: the influence of co2 and particle size on the reaction rate,” *Chemical engineering science*, vol. 51, no. 4, pp. 623–634, 1996.

[24] L. Wang, Z. Xue, J. Cai, and B. Hu, “Relationship between microstructure and properties of limestone calcined rapidly at high temperatures,” *Transactions of the Indian Institute of Metals*, vol. 72, pp. 3215–3222, 2019.

[25] M. Wang, B. Liao, Y. Liu, S. Wang, S. Qing, and A. Zhang, “Numerical simulation of oxy-coal combustion in a rotary cement kiln,” *Applied Thermal Engineering*, vol. 103, pp. 491–500, 2016.

[26] R. Edland, F. Normann, T. Allgurén, C. Fredriksson, and K. Andersson, “Scaling of pulverized-fuel jet flames that apply large amounts of excess air—implications for nox formation,” *Energies*, vol. 12, no. 14, 2019. [Online]. Available: https://www.mdpi.com/1996-1073/12/14/2680

[27] W. D. Owens, G. D. Silcox, J. S. Lighty, X. X. Deng, D. W. Pershing, V. A. Cundy, C. B. Leger, and A. L. Jakway, “Thermal analysis of rotary kiln incineration: comparison of theory and experiment,” *Combustion and Flame*, vol. 86, no. 1-2, pp. 101–114, 1991.

[28] F. P. INCROPERA, *Fundamentals of heat and mass transfer*, 7th ed. J. Wiley amp; Sons, 2011.

[29] F. Proch, K. Bauerbach, and P. Grammenoudis, “Development of an up-scalable rotary kiln design for the pyrolysis of waste tyres,” *Chemical Engineering Science*, vol. 238, p. 116573, 2021.

A

Appendix 1

The following appendix provides a detailed presentation of the results obtained from the simulations. Bed and flue gas temperatures, residence times and the heat balance for all cases are presented below, together with the three dimensional temperature maps of the kiln walls and bed, as well as the axial temperature maps of the plasma and secondary gas.

A.1 Length

In this section all results and data from varying kiln lengths are presented. For all cases the grid have 20 cells in the radial direction, 24 cells in the angular direction, and 4 discrete ordinates used. For the kiln lengths between 12-20 m the grid have 30 cells in the axial direction, whereas lengths between 21.1-30 have 40 cells in this direction.

Table A.1: Bed temperatures, flue gas temperatures and residence time for varying kiln lengths

Length [m]	**Maximum bed temperature [°C]**	**Outlet bed temperature [°C]**	**Flue gas temperature [°C]**	**Residence time [min]**
12	1330	1289	2222	13
17	1410	1328	2185	19
18	1411	1327	2177	20
19	1425	1332	2178	20
20	1439	1335	2177	22
21,1	1462	1338	2172	23
22	1460	1337	2167	24
25	1564	1337	2157	27
30	1532	1336	2149	32

Table A.2: Heat balance of the rotary kiln for varying kiln lengths, in MW

Length [m]	Radiation to bed	Convection to bed	Conduction to bed	Total heat to bed	Outer heat losses	Total heat to gas
12	0.54	0.31	0.44	1.29	0.071	5.76
17	0.62	0.34	0.48	1.44	0.10	5.58
18	0.65	0.35	0.49	1.50	0.11	5.54
19	0.66	0.36	0.50	1.52	0.12	5.54
20	0.67	0.35	0.50	1.52	0.12	5.55
21,1	0.65	0.36	0.48	1.49	0.13	5.52
22	0.68	0.37	0.50	1.55	0.14	5.50
25	0.70	0.36	0.50	1.56	0.16	5.45
30	0.68	0.37	0.47	1.52	0.19	5.41

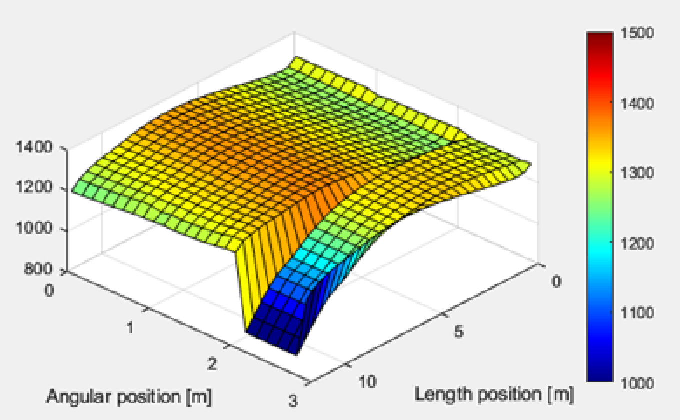

Figure A.1: Three dimensional temperature of kiln walls and bed with kiln length 12 m

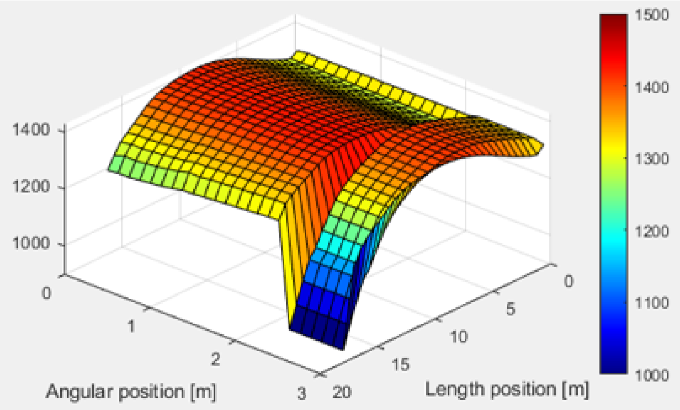

Figure A.2: Three dimensional temperature of kiln walls and bed with kiln length 17 m

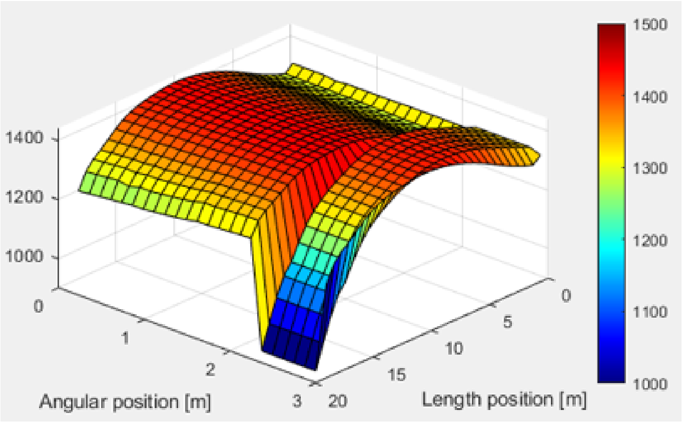

Figure A.3: Three dimensional temperature of kiln walls and bed with kiln length 19 m

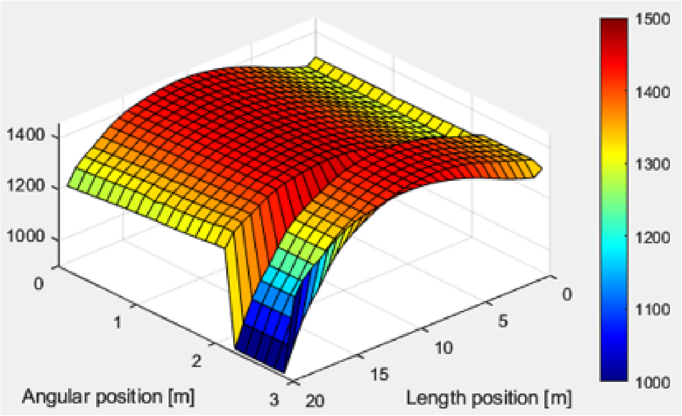

Figure A.4: Three dimensional temperature of kiln walls and bed with kiln length 20 m

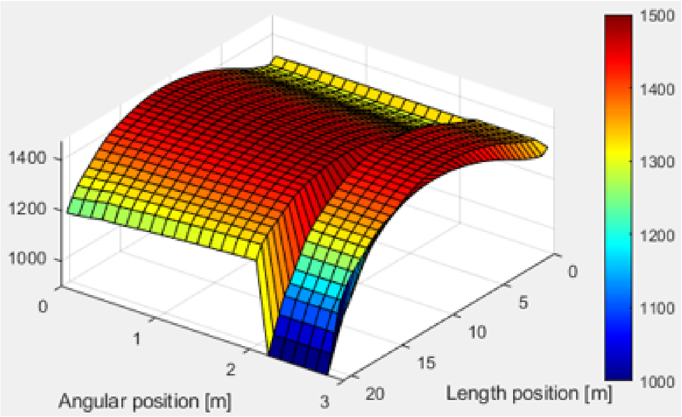

Figure A.5: Three dimensional temperature of kiln walls and bed with kiln length 21 m

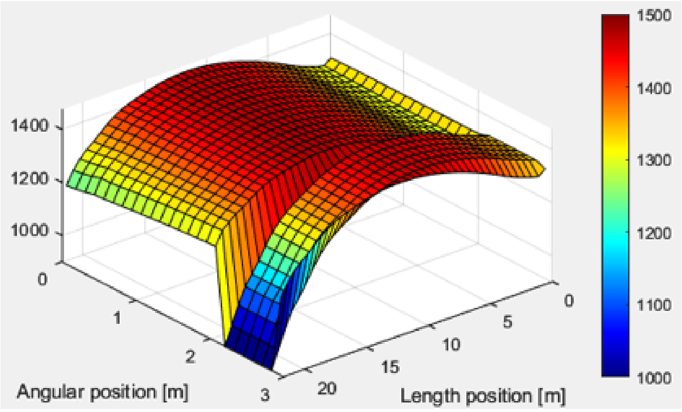

Figure A.6: Three dimensional temperature of kiln walls and bed with kiln length 22 m

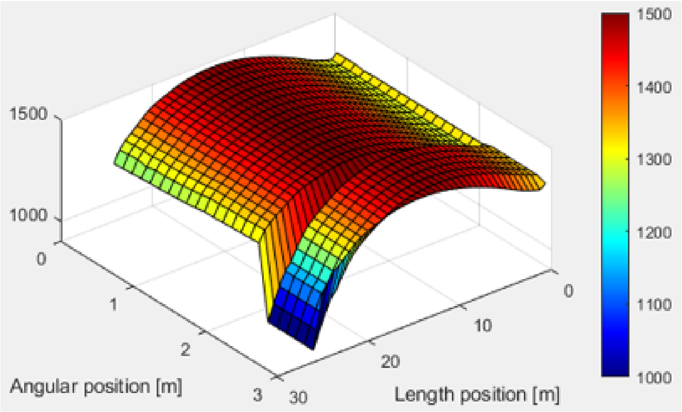

Figure A.7: Three dimensional temperature of kiln walls and bed with kiln length 25 m

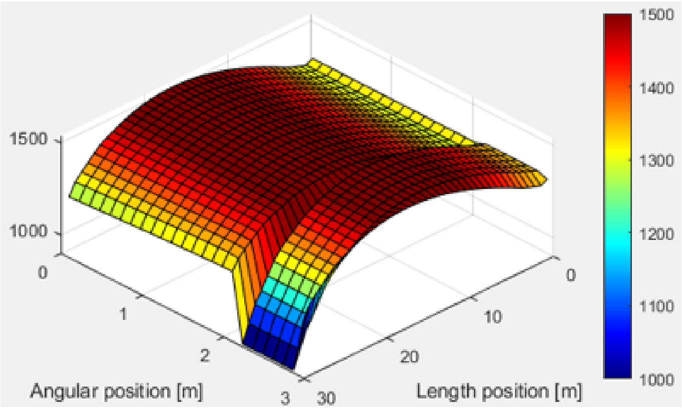

Figure A.8: Three dimensional temperature of kiln walls and bed with kiln length 30 m

A.2 Radius

Below, data and results from the simulations varying the kiln radius is presented. For all cases, a grid with of 20 radial cells, 30 axial cells and 24 angular cells was used, with an S_4 approximation for the discrete ordinates.

Table A.3: Bed temperatures, flue gas temperatures and residence time for varying kiln radii

Radius [m]	**Maximum bed temperature [°C]**	**Outlet bed temperature [°C]**	**Flue gas temperature [°C]**	**Residence time [min]**
0.3	1377	1329	2206	9
0.4	1374	1320	2178	21
0.48	1411	1327	2177	19
0.5	1423	1329	2177	21
0.55	1454	1332	2184	25
0.6	1454	1334	2184	30
0.7	1482	1335	2175	41
0.8	1507	1337	2174	54

Table A.4: Heat balance of the rotary kiln for varying kiln radius, in MW

Radius [m]	**Radiation to bed**	**Convection to bed**	**Conduction to bed**	**Total heat to bed**	**Outer heat losses**	**Total heat to gas**
0,3	0.49	0.46	0.38	1.33	0.077	5.63
0,4	0.59	0.42	0.46	1.46	0.094	5.55
0,48	0.65	0.35	0.49	1.50	0.11	5.54
0,5	0.66	0.38	0.49	1.49	0.11	5.54
0,55	0.70	0.31	0.52	1.53	0.12	5.54
0,6	0.73	0.29	0.53	1.55	0.14	5.58
0,7	0.76	0.24	0.55	1.55	0.15	5.54
0,8	0.79	0.20	0.55	1.54	0.18	5.53

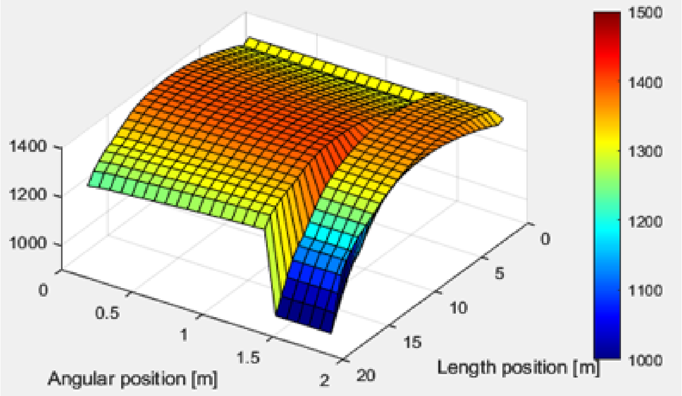

Figure A.9: Three dimensional temperature of kiln walls and bed with kiln radius 0.3 m

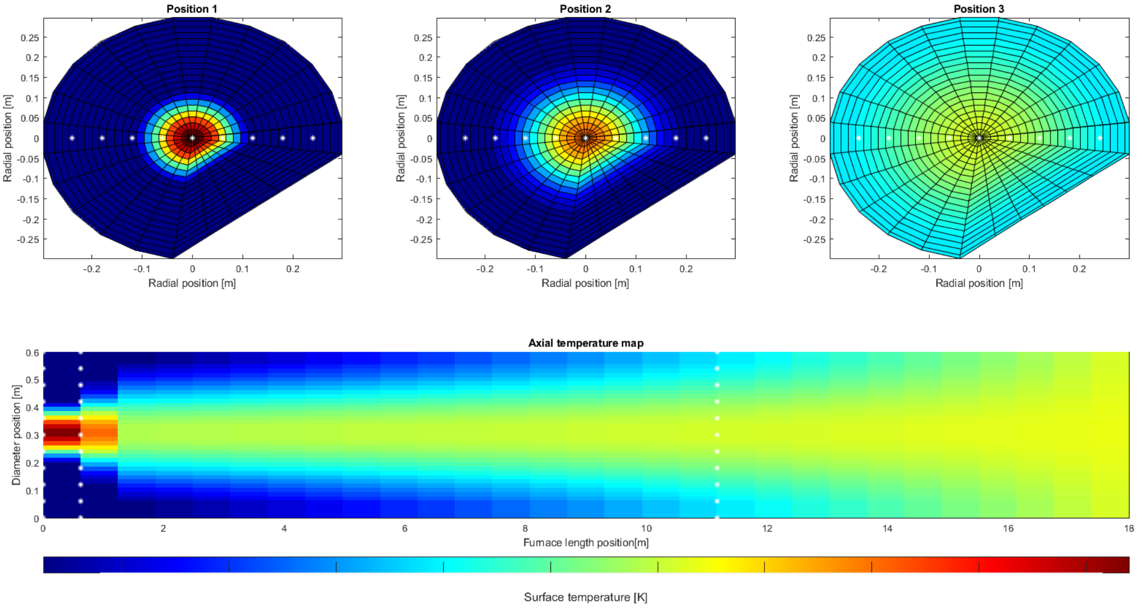

Figure A.10: On the top: vertical temperature maps of the plasma and secondary gas, on the bottom: axial temperature map of the plasma and secondary gas with a kiln radius of 0.3 m. The three cross sections correspond to the length positions marked by white stars in the axial temperature map

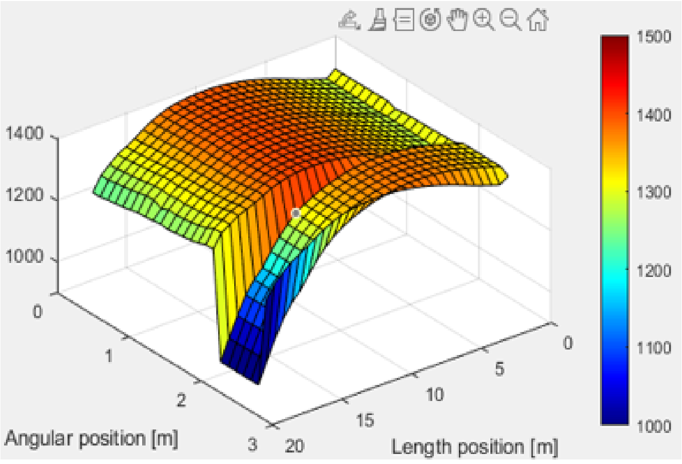

Figure A.11: Three dimensional temperature of kiln walls and bed with kiln radius 0.4 m

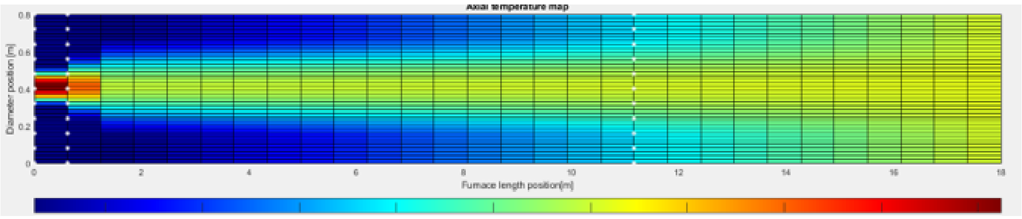

Figure A.12: Axial temperature map of the plasma and secondary gas, with a kiln radius 0.4 m

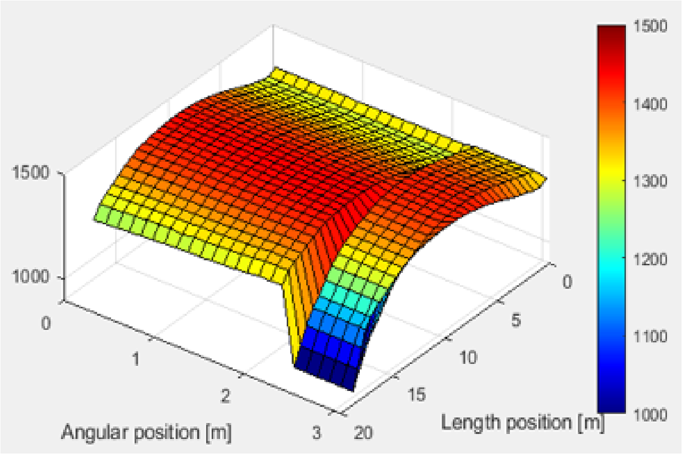

Figure A.13: Three dimensional temperature of kiln walls and bed with kiln radius 0.5 m

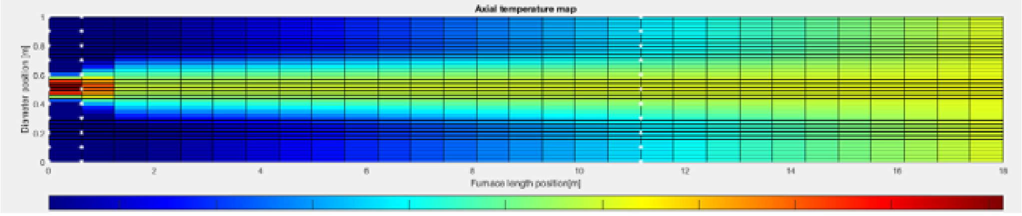

Figure A.14: Axial temperature map of the plasma and secondary gas, with a kiln radius 0.5 m

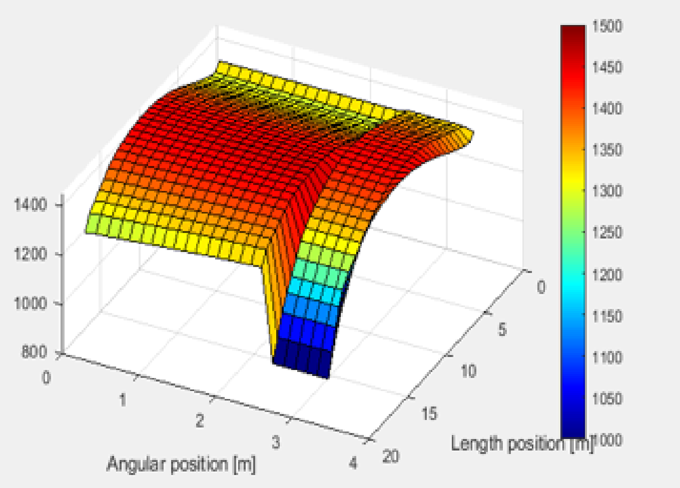

Figure A.15: Three dimensional temperature of kiln walls and bed with kiln radius 0.55 m

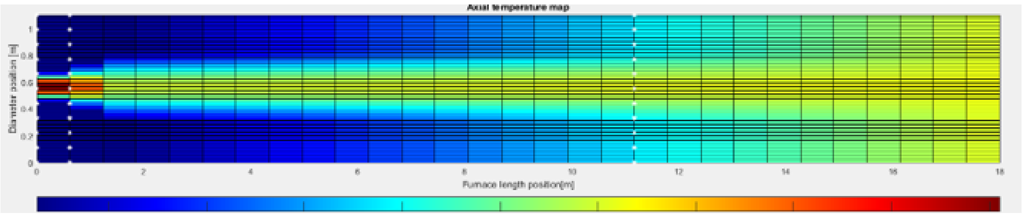

Figure A.16: Axial temperature map of the plasma and secondary gas, with a kiln radius 0.55 m

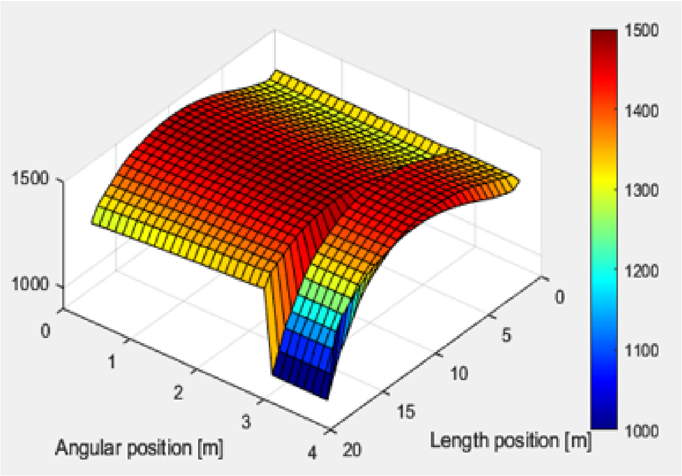

Figure A.17: Three dimensional temperature of kiln walls and bed with kiln radius 0.6 m

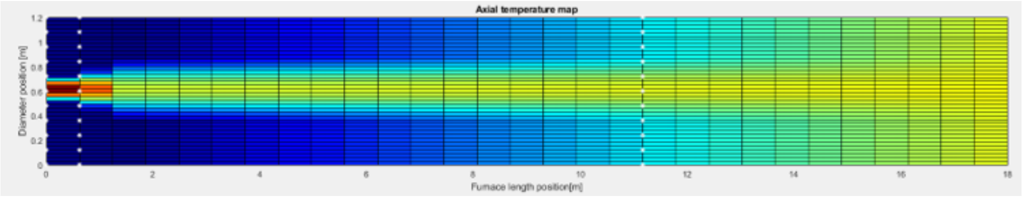

Figure A.18: Axial temperature map of the plasma and secondary gas, with a kiln radius 0.6 m

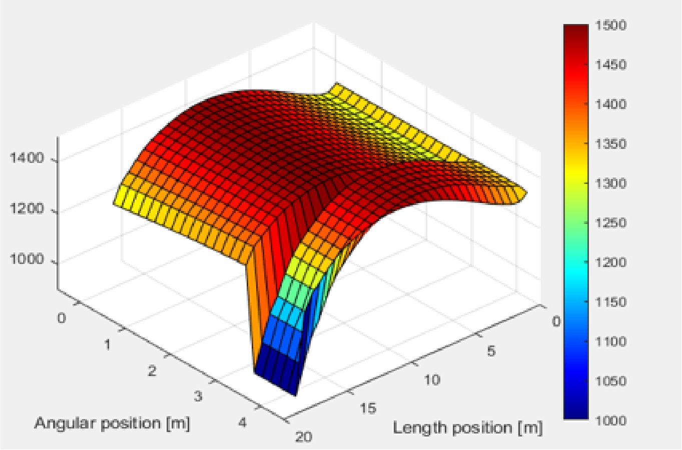

Figure A.19: Three dimensional temperature of kiln walls and bed with kiln radius 0.7 m

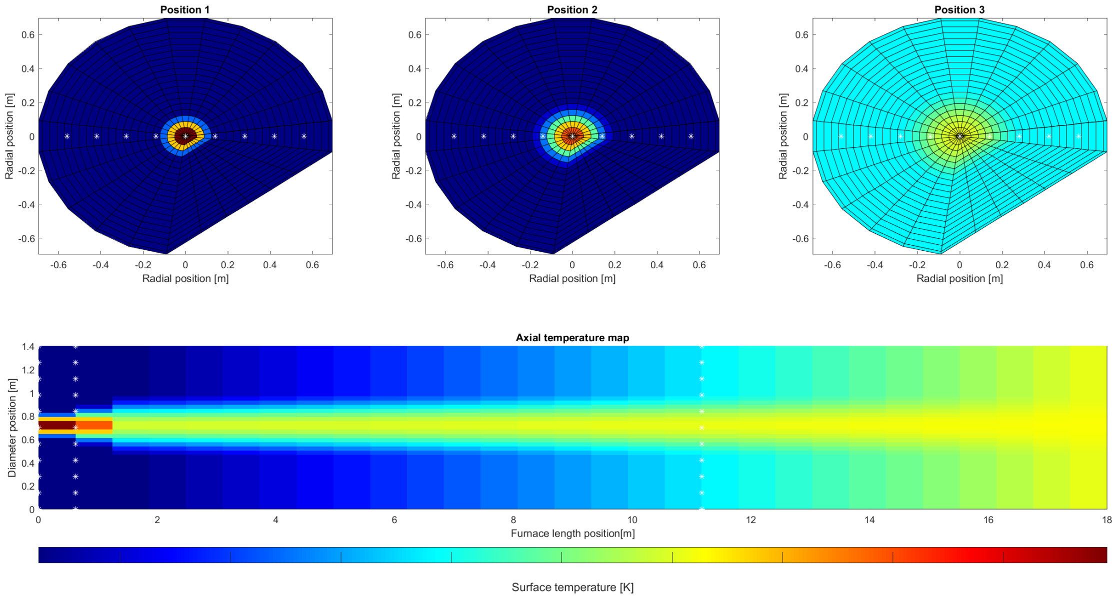

Figure A.20: On the top: vertical temperature maps of the plasma and secondary gas, on the bottom: axial temperature map of the plasma and secondary gas with a kiln radius of 0.7 m. The three cross sections correspond to the length positions marked by white stars in the axial temperature map

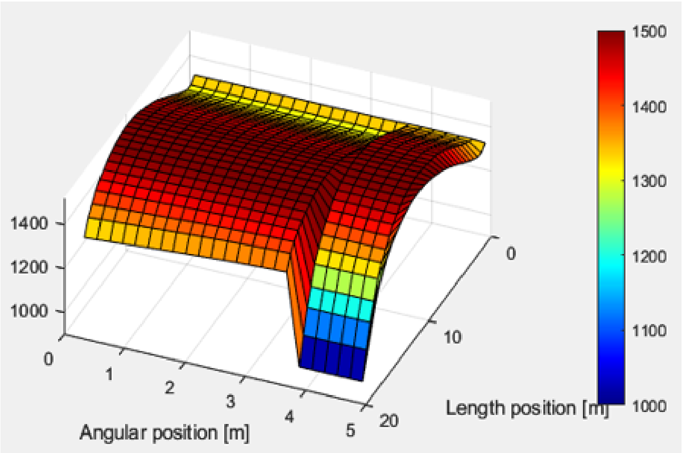

Figure A.21: Three dimensional temperature of kiln walls and bed with kiln radius 0.8 m

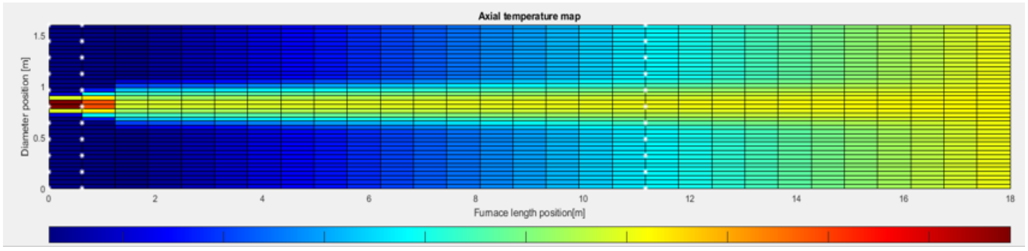

Figure A.22: Axial temperature map of the plasma and secondary gas, with a kiln radius 0.8 m

A.3 Bed mass flow

In this section all results and data from varying production rate of clinker are presented. For all cases the grid have 20 cells in the radial direction, 24 cells in the angular direction, 30 cells in the axial direction, with an S_4 approximation for the discrete ordinates.

Table A.5: Bed temperatures, flue gas temperatures and residence time for varying clinker production

Bed mass flow [ton/h]	**Maximum bed temperature [°C]**	**Outlet bed temperature [°C]**	**Flue gas temperature [°C]**	**Residence time [min]**
7	1588	1405	2527	28
10	1411	1327	2177	19
11	1360	1297	2098	18
12	1346	1286	2070	17
13	1294	1241	1978	15
14	1278	1228	1938	15
15	1241	1205	1901	13

Table A.6: Heat balance of the rotary kiln for varying clinker production, in MW

Bed mass flow [ton/h]	**Radiation to bed**	**Convection to bed**	**Conduction to bed**	**Total heat to bed**	**Outer heat losses**	**Total heat to gas**
7	0.56	0.33	0.38	1.26	0.12	5.84
10	0.65	0.35	0.49	1.50	0.11	5.54
11	0.63	0.37	0.50	1.50	0.11	5.50
12	0.62	0.39	0.50	1.51	0.11	5.68
13	0.60	0.41	0.51	1.53	0.10	5.48
14	0.58	0.42	0.50	1.50	0.10	5.53
15	0.60	0.45	0.53	1.59	0.10	5.58

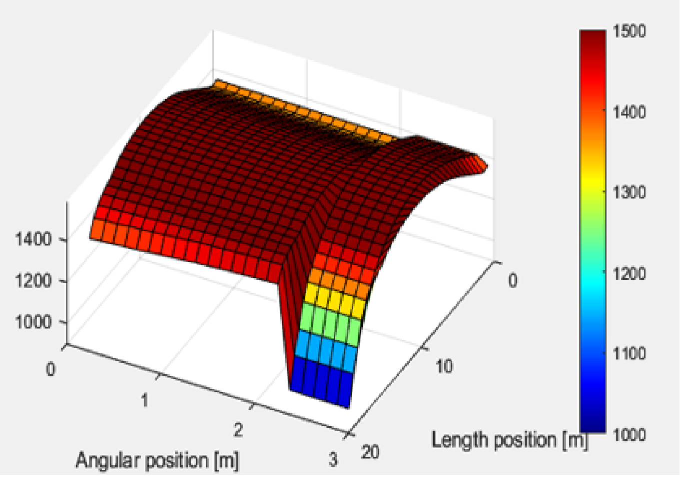

Figure A.23: Three dimensional temperature map of kiln walls and bed with clinker production 7 ton/h

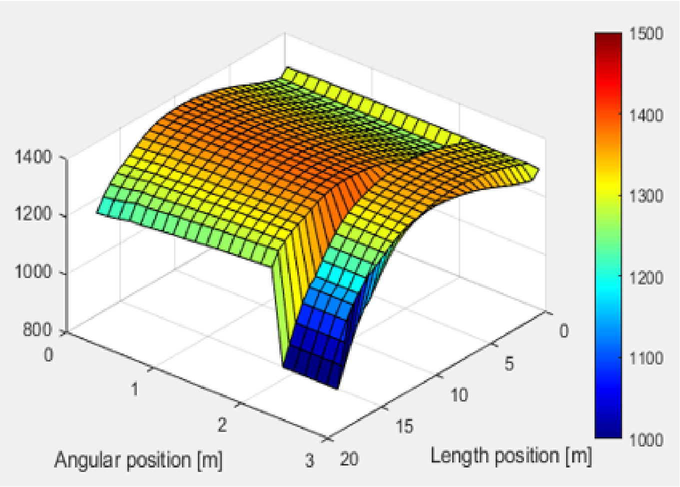

Figure A.24: Three dimensional temperature map of kiln walls and bed with clinker production 11 ton/h

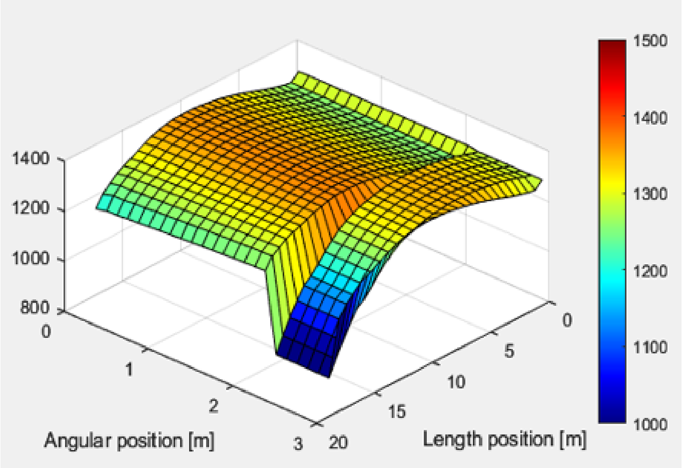

Figure A.25: Three dimensional temperature map of kiln walls and bed with clinker production 12 ton/h

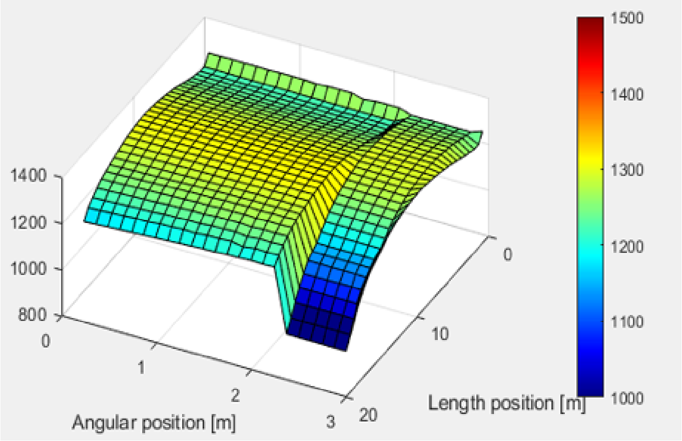

Figure A.26: Three dimensional temperature map of kiln walls and bed with clinker production 13 ton/h

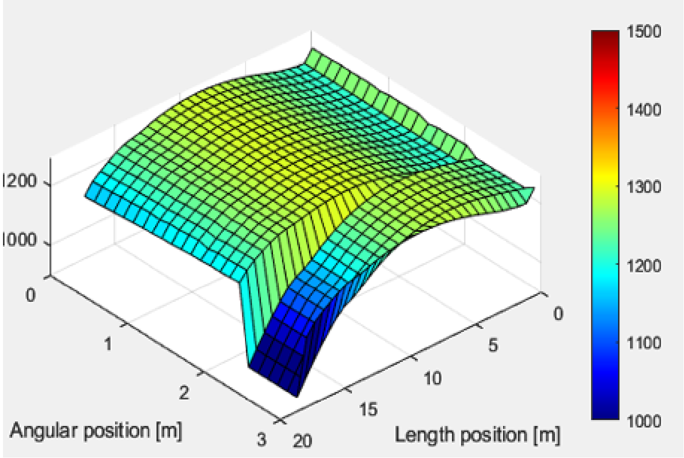

Figure A.27: Three dimensional temperature map of kiln walls and bed with clinker production 14 ton/h

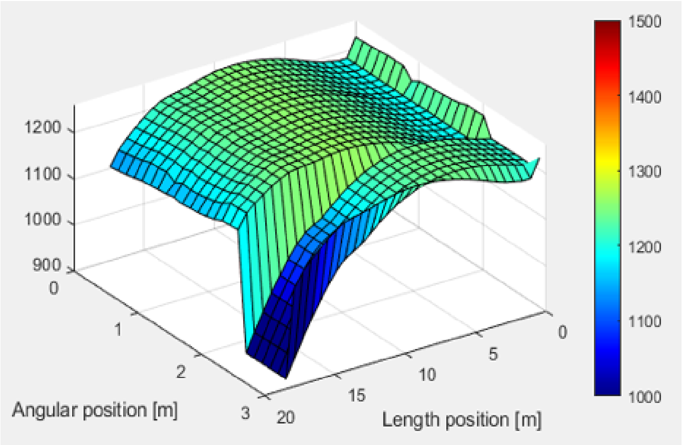

Figure A.28: Three dimensional temperature map of kiln walls and bed with clinker production 15 ton/h

A.4 Particle content

In the following section, data and results from simulations when increasing the particle content is presented. For the grid, 20 radial cells, 30 axial cells and 24 angular cells were used, with an S_4 approximation for the discrete ordinates

Table A.7: Bed temperatures, flue gas temperatures and residence time for varying particle content

Particle content [m^2/**h**]	**Maximum bed temperature [°C]**	**Outlet bed temperature [°C]**	**Flue gas temperature [°C]**	**Residence time [min]**
0	1411	1327	2177	19
6000	1453	1397	2134	19
8000	1462	1415	2116	19
10000	1472	1431	2102	19
12000	1480	1443	2077	19

Table A.8: Heat balance of the rotary kiln for varying particle content, in MW

Particle content [$\mathbf{m^2/h}$]	**Radiation to bed**	**Convection to bed**	**Conduction to bed**	**Total heat to bed**	**Outer heat losses**	**Total heat to gas**
0	0.65	0.35	0.49	1.50	0.11	5.54
6000	0.90	0.27	0.67	1.83	0.11	5.34
8000	0.96	0.25	0.70	1.91	0.12	5.25
10000	1.01	0.23	0.74	1.98	0.12	5.19
12000	1.08	0.19	0.76	2.03	0.12	5.07

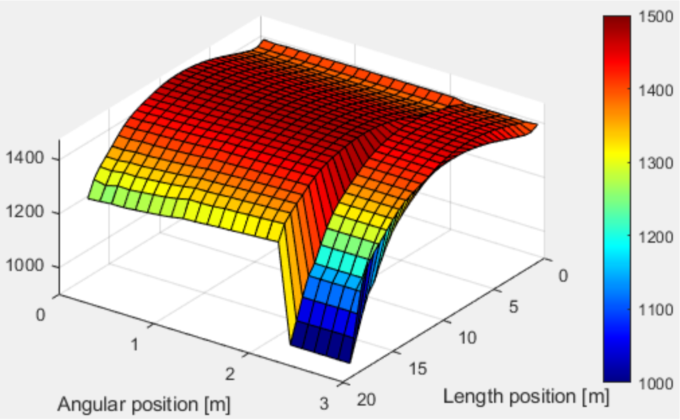

Figure A.29: Three dimensional temperature map of kiln walls and bed with a particle content of 6000 m^2/h

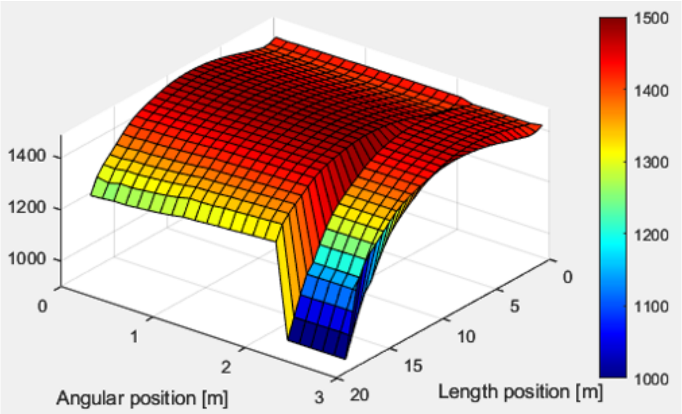

Figure A.30: Three dimensional temperature map of kiln walls and bed with a particle content of 8000 m^2/h

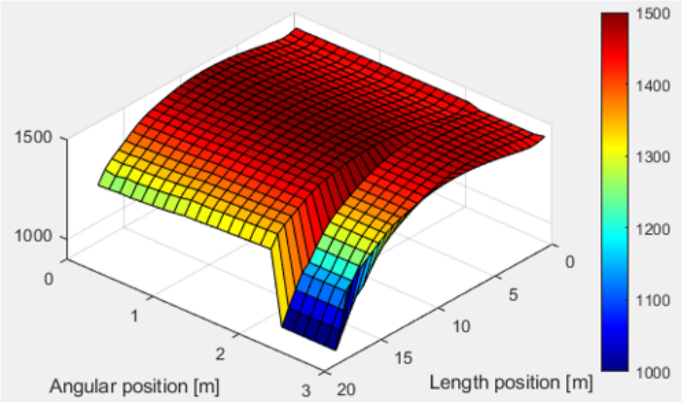

Figure A.31: Three dimensional temperature map of kiln walls and bed with a particle content of 10000 m^2/h

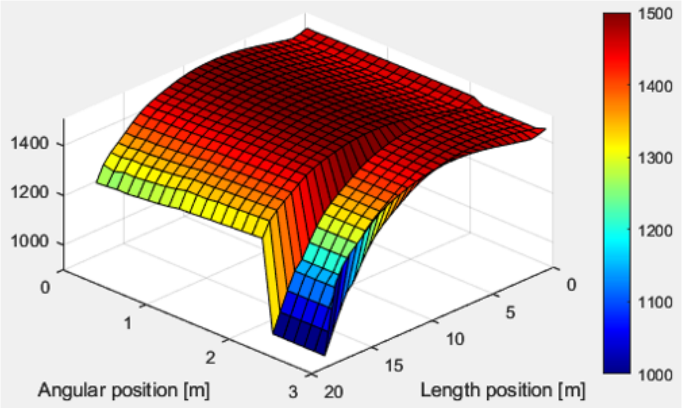

Figure A.32: Three dimensional temperature map of kiln walls and bed with a particle content of 12000 m^2/h

A.5 Flame angle

In this section all results and data from varying flame angles are presented. For all cases the grid have 20 cells in the radial direction, 24 cells in the angular direction, with an S_4 approximation for the discrete ordinates. For the flame angles 5, 10 and 35° the grid have 40 cells in the axial direction, whereas all other angles have 30 cells in this direction.

Table A.9: Bed temperatures, flue gas temperatures and residence time for varying flame angles

Flame angle [°]	**Maximum bed temperature** [°C]	**Outlet bed temperature** [°C]	**Flue gas temperature** [°C]	**Residence time** [min]
0	1411	1327	2177	19
5	1499	1424	2102	19
6	1500	1448	2080	19
7	1510	1461	2074	19
10	1520	1481	2048	19
15	1515	1499	2027	19
25	1517	1517	1998	19
35	1527	1527	1991	19

Table A.10: Heat balance of the rotary kiln for varying flame angles, in MW

Flame angle [°]	**Radiation to bed**	**Convection to bed**	**Conduction to bed**	**Total heat to bed**	**Outer heat losses**	**Total heat to gas**
0	0.65	0.35	0.49	1.50	0.11	5.54
5	0.75	0.72	0.42	1.89	0.11	5.19
6	0.79	0.77	0.45	2.01	0.11	5.08
7	0.80	0.79	0.47	2.06	0.11	5.05
10	0.82	0.83	0.48	2.13	0.11	4.93
15	0.84	0.89	0.50	2.23	0.11	4.83
25	0.84	0.98	0.49	2.31	0.11	4.69
35	0.85	0.99	0.49	2.33	0.11	4.66

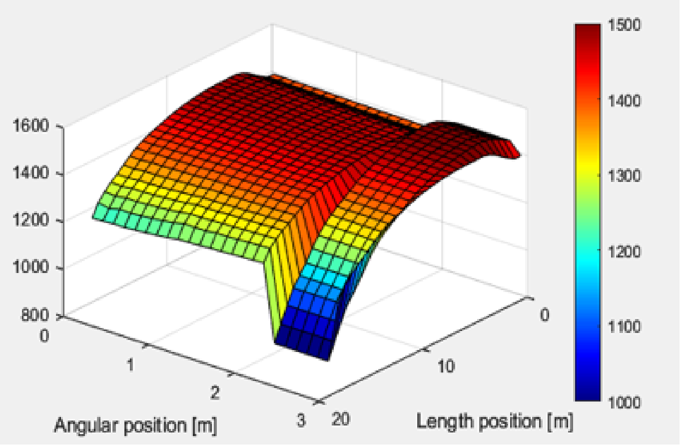

Figure A.33: Three dimensional temperature of kiln walls and bed with flame angle 6°

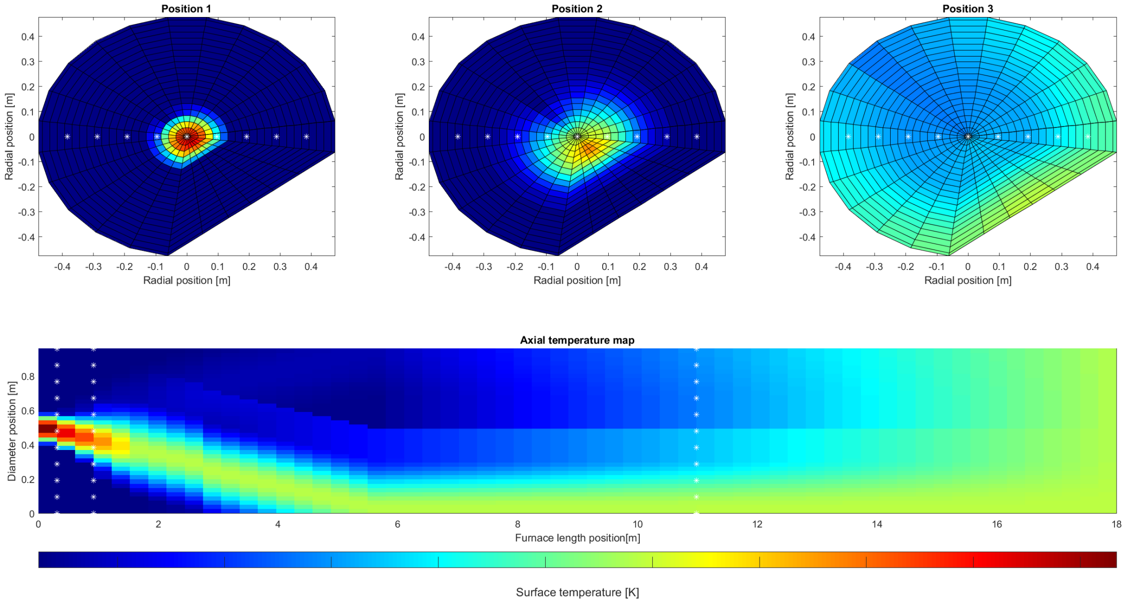

Figure A.34: On the top: vertical temperature maps of the plasma and secondary gas, on the bottom: axial temperature map of the plasma and secondary gas with flame angle 6°. The three cross sections correspond to the length positions marked by white stars in the axial temperature map

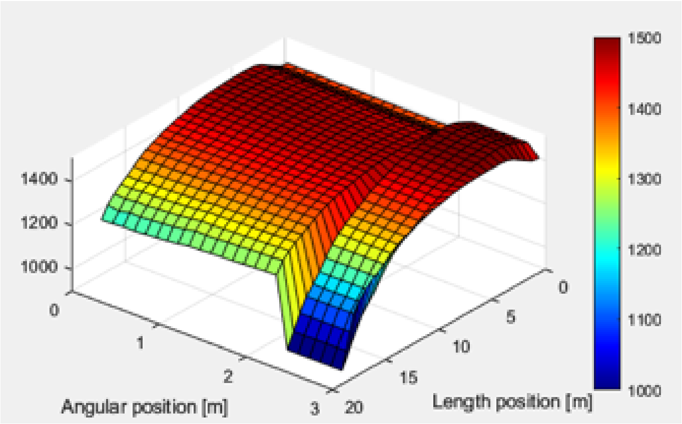

Figure A.35: Three dimensional temperature of kiln walls and bed with flame angle 7°

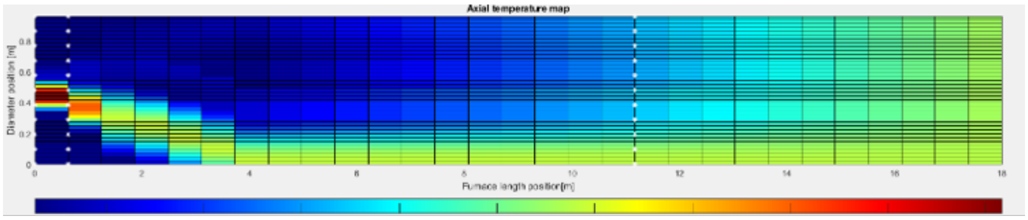

Figure A.36: Axial temperature map of the plasma and secondary gas, with flame angle 7°

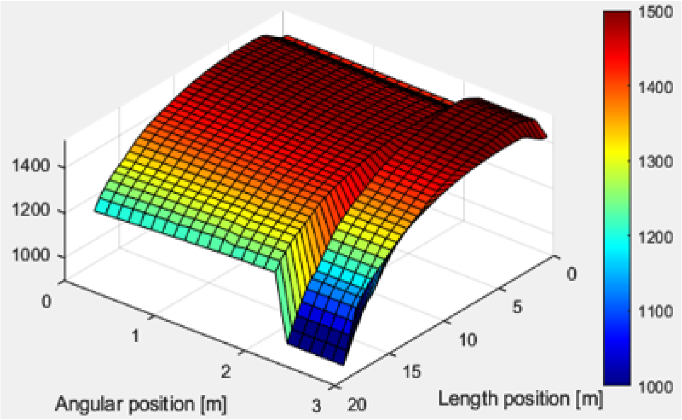

Figure A.37: Three dimensional temperature of kiln walls and bed with flame angle 10°

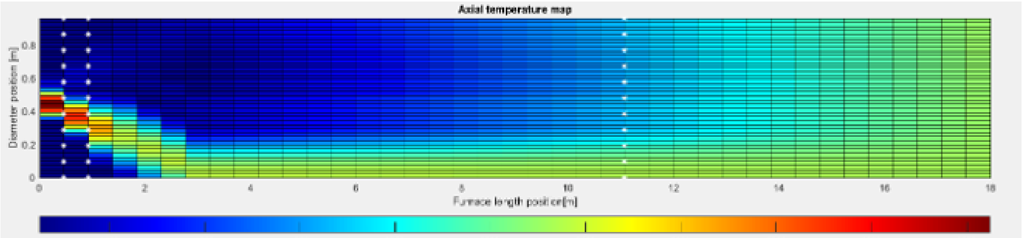

Figure A.38: Axial temperature map of the plasma and secondary gas, with flame angle 10°

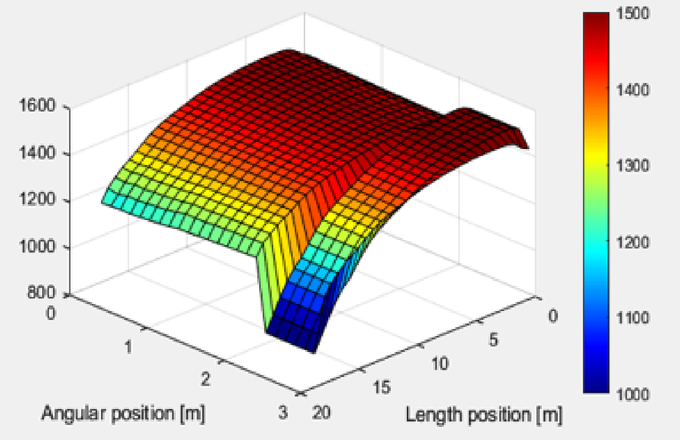

Figure A.39: Three dimensional temperature of kiln walls and bed with flame angle 15°

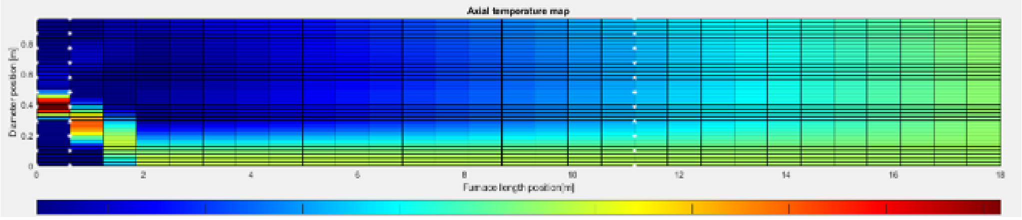

Figure A.40: Axial temperature map of the plasma and secondary gas, with flame angle 15°

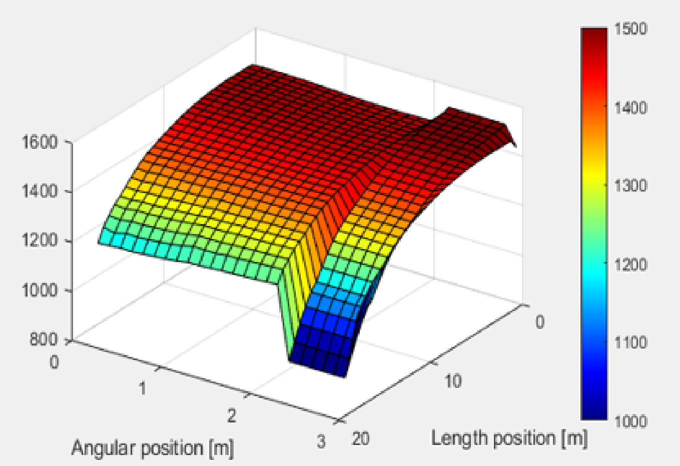

Figure A.41: Three dimensional temperature of kiln walls and bed with flame angle 25°

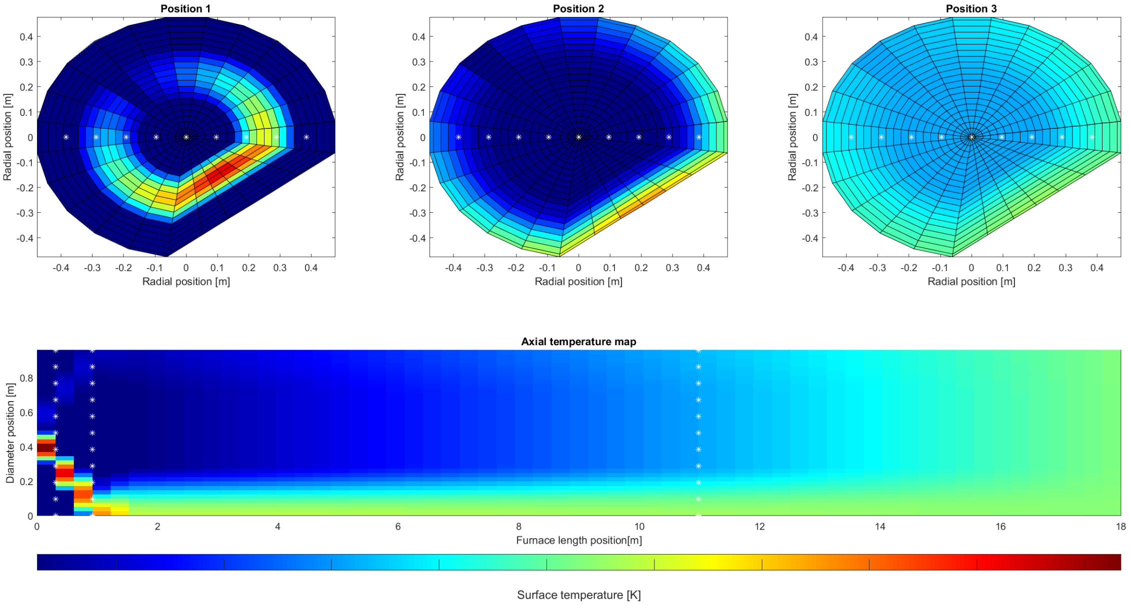

Figure A.42: On the top: vertical temperature maps of the plasma and secondary gas, on the bottom: axial temperature map of the plasma and secondary gas with flame angle 25°. The three cross sections correspond to the length positions marked by white stars in the axial temperature map

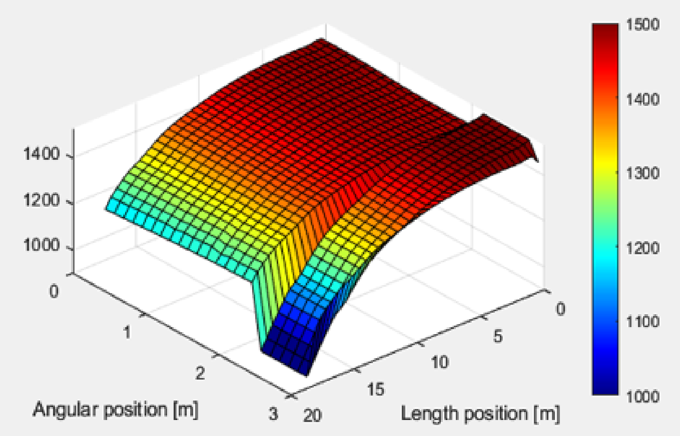

Figure A.43: Three dimensional temperature of kiln walls and bed with flame angle 35°

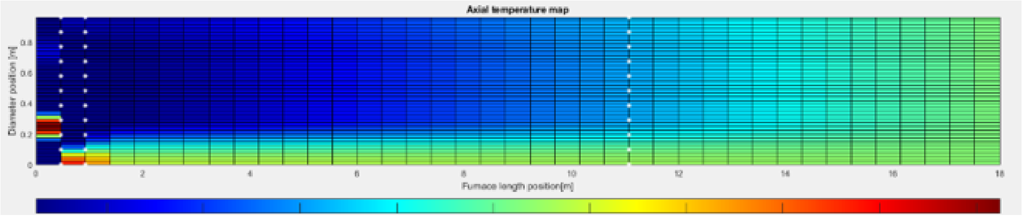

Figure A.44: Axial temperature map of the plasma and secondary gas, with flame angle 35°

A.6 Flame length

In this section all results and data from varying flame lengths are presented. For all cases the grid have 20 cells in the radial direction, 24 cells in the angular direction, with an S_4 approximation for the discrete ordinates. For the flame lengths 2 and 1.6 m the grid have 30 cells in the axial direction, whereas the flame lengths between 1.4-0.8 have 40 cells in this direction.

Table A.11

Flame length [m]	**Maximum bed temperature [°C]**	**Outlet bed temperature [°C]**	**Flue gas temperature [°C]**	**Residence time [min]**
0.8	1431	1349	2189	19
1.0	1430	1346	2192	19
1.2	1428	1341	2193	19
1.4	1420	1334	2178	19
1.6	1409	1327	2169	19
1.79	1411	1327	2177	19
2.0	1417	1330	2193	19

Table A.12: Heat balance of the rotary kiln for varying flame length, in MW

Flame length [m]	**Radiation to bed**	**Convection to bed**	**Conduction to bed**	**Total heat to bed**	**Outer heat losses**	**Total heat to gas**
0.8	0.68	0.37	0.52	1.57	0.11	5.57
1.0	0.68	0.38	0.51	1.57	0.11	5.62
1.2	0.67	0.36	0.51	1.54	0.11	5.62
1.4	0.65	0.36	0.50	1.51	0.11	5.55
1.6	0.65	0.35	0.50	1.50	0.11	5.51
1.79	0.65	0.35	0.49	1.50	0.11	5.54
2.0	0.66	0.36	0.50	1.51	0.11	5.62

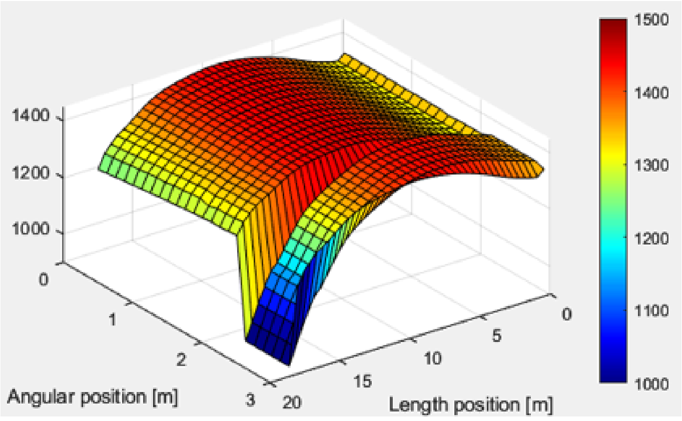

Figure A.45: Three dimensional temperature of kiln walls and bed with flame length 0.8 m

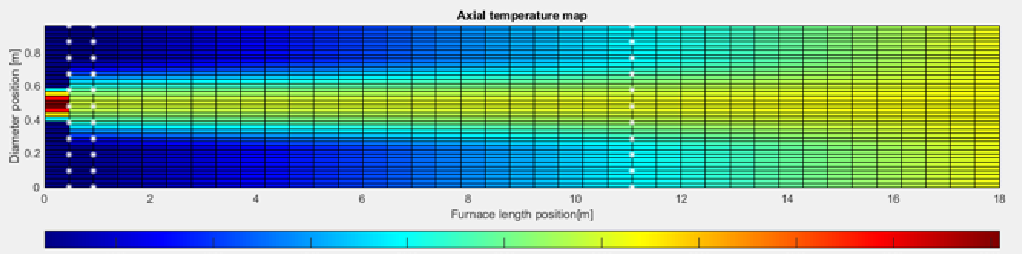

Figure A.46: Axial temperature map of the plasma and secondary gas, with flame length 0.8 m

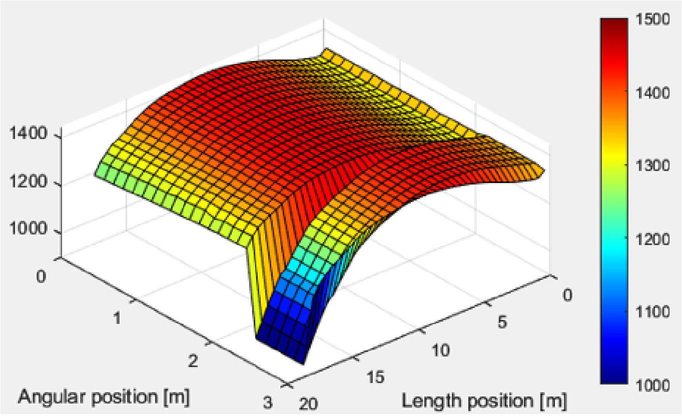

Figure A.47: Three dimensional temperature of kiln walls and bed with flame length 1 m

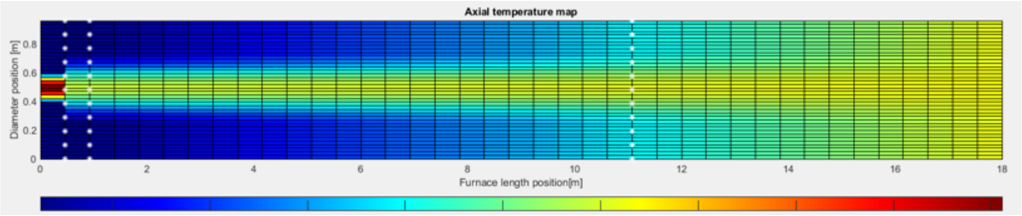

Figure A.48: Axial temperature map of the plasma and secondary gas, with flame length 1 m

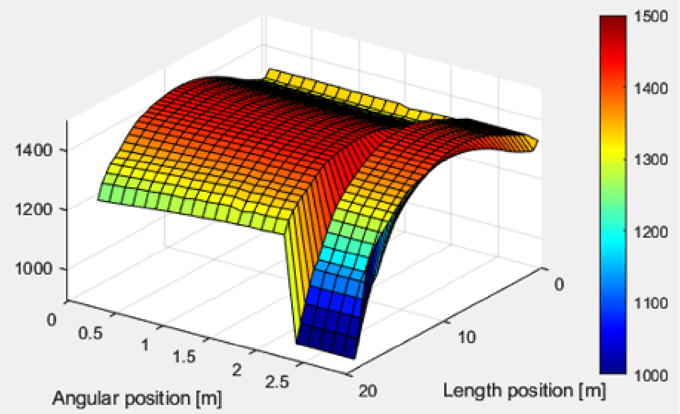

Figure A.49: Three dimensional temperature of kiln walls and bed with flame length 1.2 m

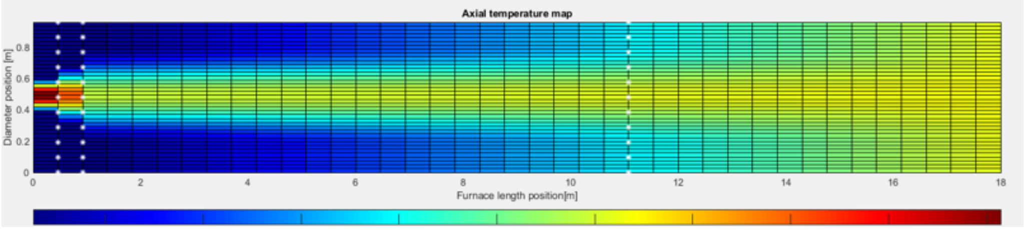

Figure A.50: Axial temperature map of the plasma and secondary gas, with flame length 1.2 m

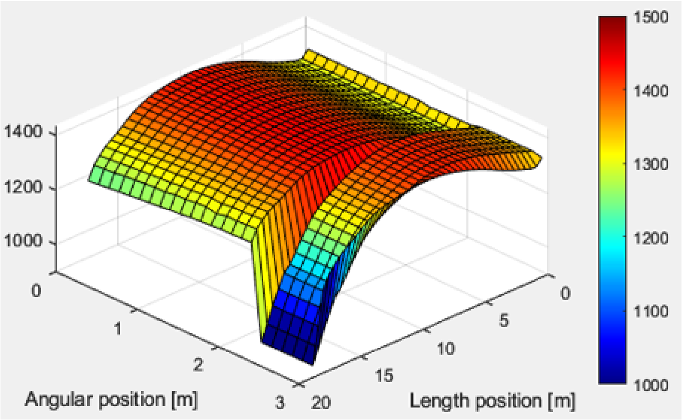

Figure A.51: Three dimensional temperature of kiln walls and bed with flame length 1.4 m

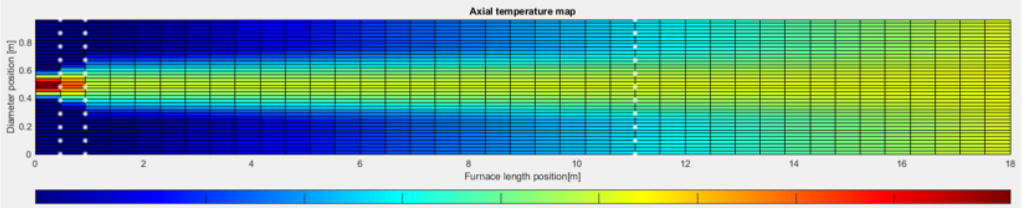

Figure A.52: Axial temperature map of the plasma and secondary gas, with flame length 1.4 m

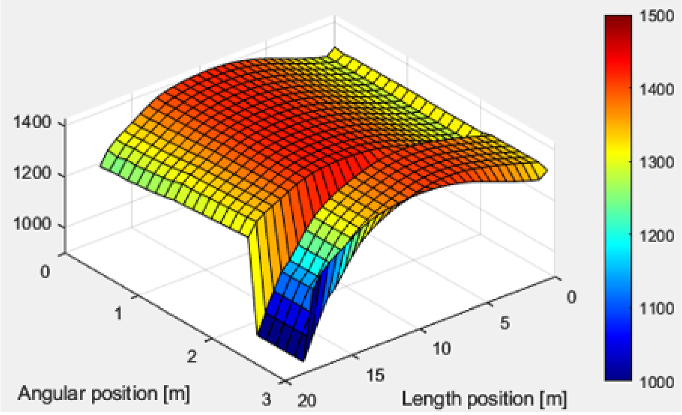

Figure A.53: Three dimensional temperature of kiln walls and bed with flame length 1.6 m

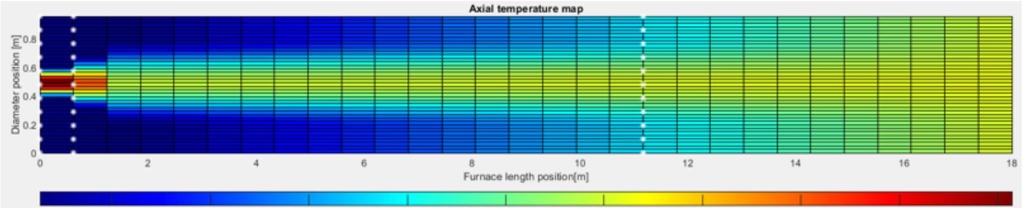

Figure A.54: Axial temperature map of the plasma and secondary gas, with flame length 1.6 m

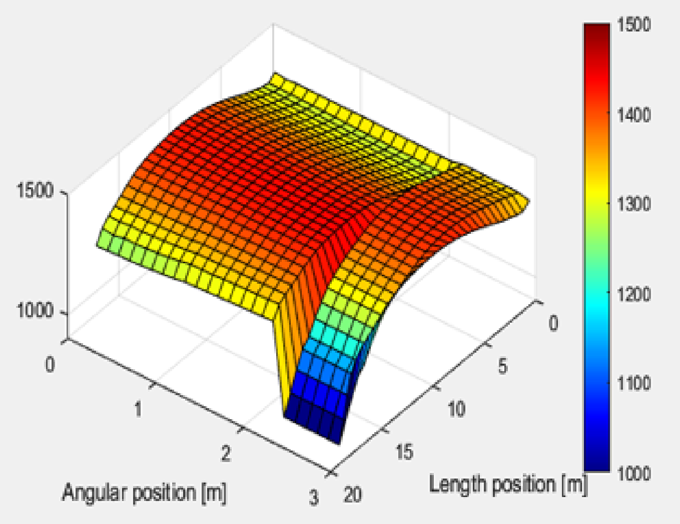

Figure A.55: Three dimensional temperature of kiln walls and bed with flame length 2 m

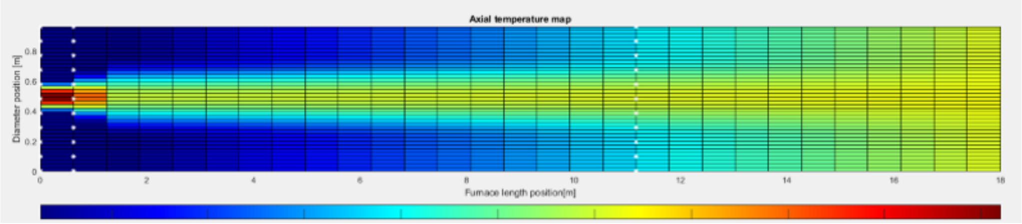

Figure A.56: Axial temperature map of the plasma and secondary gas, with flame length 2 m

B

Appendix 2

In this section the dissociation enthalpy data used for finding the maximum temperature of the plasma is presented. It was provided by Heidelberg Materials Sweden and the data was retrieved with FactSage.

Table B.1: Dissociation enthalpy data of carbon dioxide, provided by Heidelberg Materials Sweden with FactSage

T [°C]	Delta H [kWh]	O (g)	O_2 (g)	CO (g)	CO_2 (g)	MJ/kg CO_2
0	-0.25402119	5.92242E-59	5.35692E-31	1.07138E-30	1000	-0.020783552
50	0.2617041	8.62141E-49	2.04537E-25	4.09074E-25	1000	0.021412154
100	0.80705131	2.42552E-41	2.51727E-21	5.03455E-21	1000	0.066031471
150	1.3795105	1.20286E-35	3.36268E-18	6.72537E-18	1000	0.112869041
200	1.9764892	3.77172E-31	9.83787E-16	1.96757E-15	1000	0.161712753
250	2.5955691	1.64717E-27	9.73096E-14	1.94619E-13	1000	0.212364745
300	3.2345753	1.67607E-24	4.31901E-12	8.63802E-12	1000	0.26464707
350	3.8915804	5.63732E-22	1.0427E-10	2.0854E-10	1000	0.318402033
400	4.5648834	8.01527E-20	1.56778E-09	3.13555E-09	1000	0.37349046
450	5.2529831	5.75668E-18	1.61933E-08	3.23866E-08	1000	0.429789526
500	5.9545519	2.38349E-16	1.23566E-07	2.47133E-07	1000	0.48719061
550	6.6684117	6.28794E-15	7.36051E-07	1.4721E-06	1000	0.545597321
600	7.3935131	1.14179E-13	3.57121E-06	7.14241E-06	999.99999	0.604923799
650	8.1289184	1.51612E-12	1.45911E-05	2.91821E-05	999.99997	0.665093324
700	8.8737875	1.5447E-11	5.1549E-05	0.000103098	999.9999	0.726037159
750	9.6273677	1.25525E-10	0.000160868	0.000321735	999.99968	0.787693721
800	10.388989	8.39632E-10	0.000451193	0.000902386	999.9991	0.850008191
850	11.158062	4.74434E-09	0.001153698	0.002307401	999.99769	0.912932345
900	11.93409	2.31385E-08	0.002721423	0.005442869	999.99456	0.976425545
950	12.716682	9.91708E-08	0.005980957	0.011962013	999.98804	1.0404558
1000	13.505582	3.79242E-07	0.01234918	0.024698739	999.9753	1.105002164
1050	14.300711	1.31079E-06	0.024125297	0.048251905	999.95175	1.170058173
1100	15.102216	4.14014E-06	0.04486423	0.0897326	999.91027	1.235635855
1150	15.910544	1.20637E-05	0.07983191	0.15967588	999.84032	1.301771782
1200	16.726515	3.26949E-05	0.13653675	0.27310619	999.72689	1.368533045
1250	17.551411	8.30056E-05	0.22532503	0.45073307	999.54927	1.436024536
1300	18.387077	0.000198636	0.36002181	0.72024225	999.27976	1.504397209

T [°C]	Delta H [kWh]	O (g)	O_2 (g)	CO (g)	CO_2 (g)	MJ/kg CO_2
1350	19.236019	0.000450505	0.55859314	1.1176368	998.88236	1.5738561
1400	20.101503	0.000972997	0.84380084	1.6885747	998.31143	1.644668427
1450	20.987657	0.002009721	1.2438167	2.4896431	997.51036	1.717171936
1500	21.899555	0.003984795	1.7927615	3.5895077	996.41049	1.791781773
1550	22.843296	0.007609847	2.5311294	5.0698686	994.93013	1.868996945
1600	23.826062	0.014039247	3.5060545	7.0261482	992.97385	1.949405073
1650	24.856192	0.025088361	4.7713777	9.5678438	990.43216	2.033688436
1700	25.943392	0.043531653	6.3874653	12.818462	987.18154	2.122641164
1750	27.098307	0.073499051	8.4207338	16.914967	983.08503	2.217134209
1800	28.332587	0.12098992	10.942841	22.006671	977.99333	2.318120755
1850	29.658841	0.19452392	14.02949	28.253505	971.7465	2.426632445
1900	31.090501	0.30594665	17.758815	35.823576	964.17642	2.543768264
1950	32.641647	0.47140528	22.20929	44.889985	955.11001	2.670680209
2000	34.326781	0.71250401	27.457167	55.626839	944.37316	2.808554809
2050	36.160551	1.0576423	33.573399	68.20444	931.79556	2.958590536
2100	38.157434	1.5435271	40.620068	82.783664	917.21634	3.121971873
2150	40.331364	2.2168377	48.646371	99.509579	900.49042	3.299838873
2200	42.695334	3.136	57.684207	118.50441	881.49559	3.4932546
2250	45.260957	4.3730063	67.743534	139.86007	860.13993	3.703169209
2300	48.038024	6.0151871	78.80765	163.63049	836.36951	3.930383782
2350	51.034063	8.1668105	90.82869	189.82419	810.17581	4.175514245
2400	54.253943	10.950351	103.72365	218.39765	781.60235	4.438958973
2450	57.699537	14.507245	117.37134	249.24993	750.75007	4.720871209
2500	61.369496	18.997922	131.61074	282.21941	717.78059	5.021140582
2550	65.25916	24.600897	146.24106	317.08313	682.91687	5.339385818
2600	69.360629	31.510752	161.02421	353.55929	646.44071	5.674960555
2650	73.663012	39.934789	175.68931	391.31357	608.68643	6.026973709
2700	78.152845	50.088321	189.94006	429.96865	570.03135	6.394323682
2750	82.814641	62.188548	203.46419	469.11717	530.88283	6.775743355
2800	87.631516	76.447084	215.94476	508.33689	491.66311	7.169851309
2850	92.585822	93.061323	227.07277	547.20721	452.79279	7.575203618
2900	97.659691	112.20484	236.56009	585.32541	414.67459	7.990338355
2950	102.83541	134.01715	244.15196	622.32152	377.67848	8.413806273
3000	108.09556	158.59316	249.6384	657.87047	342.12953	8.844182182
3050	113.42295	185.97277	252.86372	691.70075	308.29925	9.280059545
3100	118.80019	216.13104	253.73386	723.59934	276.40066	9.720015545
3150	124.2092	248.96965	252.22129	753.41285	246.58715	10.16257091
3200	129.63057	284.31041	248.3672	781.04545	218.95455	10.60613755
3250	135.04288	321.89168	242.28098	806.45431	193.54569	11.04896291
3300	140.42233	361.36897	234.13685	829.64334	170.35666	11.48909973
3350	145.74249	402.32036	224.16749	850.656	149.344	11.92438555
3400	150.97461	444.2579	212.65469	869.56793	130.43207	12.35246809
3450	156.08829	486.64483	199.91718	886.4798	113.5202	12.77086009
3500	161.05259	528.91837	186.29591	901.51068	98.489263	13.17703009

T [°C]	Delta H [kWh]	O (g)	O_2 (g)	CO (g)	CO_2 (g)	MJ/kg CO_2
3550	165.83748	570.51627	172.13788	914.79242	85.207497	13.56852109
3600	170.41552	610.90498	157.77953	926.4643	73.53557	13.943088
3650	174.7634	649.60633	143.53124	936.6689	63.330911	14.29882364
3700	178.86328	686.21972	129.66439	945.54837	54.451356	14.63426836
3750	182.70367	720.43739	116.40224	953.24142	46.758172	14.94848209
3800	186.27973	752.0514	103.91519	959.88091	40.118495	15.24106882
3850	189.59305	780.95237	92.32049	965.59191	34.407221	15.51215864
3900	192.65096	807.121	81.685811	970.49039	29.508364	15.76235127
3950	195.46554	830.61467	72.035601	974.6823	25.315913	15.99263509
4000	198.05229	851.55035	63.358986	978.26325	21.734213	16.20427827
4050	200.42911	870.08876	55.618422	981.31842	18.677989	16.39874536
4100	202.61508	886.41773	48.757659	983.92296	16.071997	16.57759745
4150	204.62955	900.73882	42.708875	986.14249	13.850467	16.74241773
4200	206.49143	913.25644	37.398483	988.03387	11.956362	16.89475336
4250	208.21868	924.16974	32.75159	989.64597	10.340555	17.03607382
4300	209.82798	933.66711	28.695191	991.02057	8.9609707	17.16774382
4350	211.33456	941.92282	25.160297	992.19312	7.7817337	17.29100945
4400	212.75214	949.09529	22.083203	993.19357	6.7723675	17.40699327
4450	214.09297	955.32661	19.4061	994.04709	5.9070505	17.51669755
4500	215.36788	960.74297	17.077239	994.77466	5.1639478	17.62100836
4550	216.58646	965.45557	15.050776	995.39364	4.5246195	17.72071036
4600	217.75715	969.56187	13.286424	995.91827	3.9735034	17.81649409
4650	218.88742	973.14706	11.748999	996.36	3.4974689	17.90897073
4700	219.9839	976.28556	10.407924	996.72761	3.0854342	17.99868273
4750	221.05252	979.04207	9.2367061	997.02829	2.7280428	18.08611527
4800	222.09869	981.47351	8.212466	997.26662	2.4173864	18.171711
4850	223.1274	983.62989	7.3154705	997.44542	2.1467746	18.25587818
4900	224.14336	985.55556	6.5287225	997.56567	1.9105395	18.33900218
4950	225.15112	987.2903	5.8375897	997.62648	1.7038728	18.42145527
5000	226.1552	988.87024	5.2294785	997.62508	1.5226889	18.50360727
5050	227.16023	990.32903	4.6935503	997.55643	1.3635101	18.585837
5100	228.171	991.69776	4.2204655	997.41407	1.2233715	18.66853636
5150	229.19267	993.00697	3.8021804	997.18861	1.0997403	18.75212755
5200	230.23087	994.2866	3.4317557	996.86831	0.99044897	18.83707118
5250	231.29179	995.56689	3.1032003	996.43863	0.89363893	18.92387373
5300	232.38238	996.87901	2.8113355	995.88196	0.80771358	19.01310382
5350	233.51044	998.25576	2.5516799	995.17719	0.73129858	19.10539964
5400	234.6848	999.73217	2.3203499	994.29945	0.66320867	19.20148364
5450	235.91545	1001.3461	2.1139756	993.21959	0.60241963	19.30217318
5500	237.21369	1003.139	1.9296284	991.90391	0.5480447	19.40839282
5550	238.59228	1005.1563	1.7647597	990.31363	0.49931461	19.52118655
5600	240.06559	1007.4477	1.6171478	988.40459	0.45556075	19.64173009
5650	241.64968	1010.0684	1.484853	986.1269	0.41620089	19.77133745

T [°C]	Delta H [kWh]	O (g)	O_2 (g)	CO (g)	CO_2 (g)	MJ/kg CO_2
5700	243.36243	1013.0786	1.3661785	983.42464	0.38072702	19.91147155
5750	245.22352	1016.5442	1.2596376	980.23579	0.34869513	20.06374255
5800	247.25416	1020.5368	1.1639247	976.4922	0.31971637	20.22988582
5850	249.47767	1025.1333	1.0778905	972.11981	0.29344962	20.41180936
5900	251.91916	1030.4159	1.0005212	967.03914	0.26959513	20.61156764
5950	254.60514	1036.471	0.93092009	961.16604	0.24788905	20.83132964
6000	257.56327	1043.3885	0.86829141	954.41281	0.22809885	21.07335845

DEPARTMENT OF ENERGY TECHNOLOGY
CHALMERS UNIVERSITY OF TECHNOLOGY
Gothenburg, Sweden
www.chalmers.se

CHALMERS
UNIVERSITY OF TECHNOLOGY